ABSTRACT

VIBRATION-INDUCED Ddensification OF GRANULAR MATERIALS

by
Ninghua Zhang

Physical experiments as well as discrete element simulations of vibration are carried out. The use of different amplitudes and frequencies are applied in the experiments to facilitate the observation of densification trends with mono-disperse acrylic spheres and multi-disperse polyethylene pellets. For mono-disperse acrylic spheres, four densification trends are found at different vibration conditions, and attaining the "maximum density" is closely related to the combination of vibration frequency and amplitude, in agreement with experiments in the literature. For multi-disperse polyethylene pellets, there is a substantial increase in solids fraction due to the effects of particle shape and surface friction. Computer simulations applying the discrete element method are then used to investigate the influence of material properties, container geometry and vibration amplitude and frequency on the vibration process. The instantaneous dynamic states have been deeply investigated. The results obtained are in agreement with the experiments of Thomas et al. and consistent with theoretical predictions of Richman et al. at the high relative accelerations. At low relative accelerations, the initial structure of the poured particle bed strongly affects the dynamic behavior. From the analysis of the relaxed states, four densification trends have also been found, and the relationship between the instantaneous dynamic states and final relaxed states is established. Several possible densification mechanisms have been discussed, which is substantiated by evolution of the solids fraction.

VIBRATION-INDUCED DENSIFICATION OF GRANULAR MATERIALS

by
Ninghua Zhang

A Dissertation
Submitted to the Faculty of
New Jersey Institute of Technology
in Partial Fulfillment of the Requirements for the Degree of
Doctor of Philosophy

Department of Mechanical Engineering

January 2004

APPROVAL PAGE

VIBRATION-INDUCED DENSIFICATION OF GRANULAR MATERIALS

Ninghua Zhang

Dr. Anthony D. Rosato, Dissertation Advisor — Date
Professor of Mechanical Engineering, NJIT

Dr. Ian S. Fischer, Committee Member — Date
Professor of Mechanical Engineering, NJIT

Dr. Ernest S. Geskin, Committee Member — Date
Professor of Mechanical Engineering, NJIT

Dr. Jonathan H. C. Luke, Committee Member — Date
Professor of Mathematical Sciences, NJIT

Dr. I. Joga Rao, Committee Member — Date
Assistant Professor of Mechanical Engineering, NJIT

BIOGRAPHICAL SKETCH

Author: Ninghua Zhang

Degree: Doctor of Philosophy

Date: January 2004

Undergraduate and Graduate Education:

- Doctor of Philosophy in Mechanical Engineering
  New Jersey Institute of Technology,
  Newark, New Jersey, 2004

- Master of Science in Material Engineering
  Wuhan Institute of Technology
  Wuhan, P. R. China, 1993

- Material Engineering
  Shanghai College of Building Materials
  Shanghai, P. R. China, 1987

Major: Mechanical Engineering

Presentations and Publications:

N. Zhang, Rosato, A.D.,
"Vibration-Induced Densification of Granular Materials",
the 39th Annual Meeting of the Society of Engineering Science, PA, USA, 2002.

Rosato, A.D., Blackmore, D., N. Zhang and Y. Lan,
"A Perspective on Vibration-Induced Size Segregation of Granular Materials",
Chemical Engineering Science 57, 265-275 (2002).

Rosato, A.D., Blackmore, D., N. Zhang and Y. Lan,
"A Perspective on Vibration-Induced Size Segregation of Granular Materials",
the 9th Nisshin Engineering Particle Technology International Symposium,
Kyoto, Japan, 2001.

This dissertation is dedicated to
my son, Jason, my wife, Yuefeng and my parents

ACKNOWLEDGMENT

The author wishes to express his sincere gratitude to his advisor, Dr. Anthony D. Rosato, for his guidance, friendship and moral support through this research.

Special thanks to Drs. Ian S. Fischer, Ernest S. Geskin, Jonathan H.C. Luke and I. Joga Rao for serving as members of the committee.

The author would also like to thank Dr. Yidan Lan of Union Carbide and Dr. Wenliang Chen of New Jersey Institute of Technology for giving me many helpful discussions.

TABLE OF CONTENTS

TABLE OF CONTENTS
(Continued)

Chapter **Page**

TABLE OF CONTENTS
(Continued)

Chapter **Page**

TABLE OF CONTENTS
(Continued)

Chapter **Page**

LIST OF TABLES

Table **Page**

LIST OF FIGURES

LIST OF FIGURES
(Continued)

Figure **Page**

LIST OF FIGURES
(Continued)

LIST OF FIGURES
(Continued)

Figure **Page**

LIST OF FIGURES
(Continued)

Figure **Page**

LIST OF FIGURES
(Continued)

Figure **Page**

LIST OF FIGURES
(Continued)

Figure **Page**

CHAPTER 1

INTRODUCTION

1.1 Overview

The behavior of vibrating granular beds has been of great interest to industries which process granular materials, such as plastics, powder metals, ceramics, food and pharmaceuticals. From daily observations to extended scientific research, vibrations applied to granular assemblies can produce two dramatically different effects: either the bed densifies or it becomes fluidized.

Densification of bulk solids by vibration, known as vibratory compaction, is extensively used in industry. These techniques involve the supply of energy to the bed of particles at a selected frequency and amplitude for some time period, but for different materials, how to determine the most suitable parameters (such as vibration frequency and amplitude) to attain a "maximum density" is still an open problem. The complication lies on the fact that many factors (i.e. resilience, friction, particle sharp & size, material density, geometry of container and the initial state before vibration) affect the behavior. Much effort has been made in the past to attain the densest packing [1, 2, 3, 4, 5, 6, 7]. Due to the difficulties of obtaining data on individual particle motions and local property in a particle bed, these experimental studies were focused on the phenomenology to explain the observed behavior. Recently, there have been experiments, modeling and simulations on the behavior of bulk solids subject to tapping [9, 10, 11, 12].

Fluidization of granular beds by vibration has been another challenging area of study. A granular bed can be fluidized and different kinds of complicated phenomena are

generated under external vibration. These phenomena include heaping [13, 14, 15], pattern formation [16], convection [17, 18], size segregation [19, 20, 21, 22], surface wave [13, 23, 24, 25, 27] and arching [13, 16, 23, 26, 27].

The manner in which particles pack or self-arrange in a containment vessel is also an important area related to the subject of this dissertation, since both densification and fluidization depend on the microstructure for low energy vibrations. Numerous investigations on the packing of spheres can be found in the literature, including experiments [7, 29, 30] and computer simulations [31 – 36, 81 – 86].

1.2 Literature Survey

1.2.1 Sphere Packing

Randomly packed beds are extensively used in many industries (such as granular materials, plastics, powder metals, ceramics, food and pharmaceuticals). Furthermore, packed beds of spheres also serve as a model for other more general porous system. As early as 1944, Oman and Watson [28] coined the terms "random dense" and "random loose" to describe the two limiting cases of random, uniform sphere packing. In 1960, Scott [29] carried out a number of different experiments with 3mm steel ball bearing to study dense and loose random packing. He poured the steel spheres into cylindrical containers followed by 2 minutes of shaking to obtain a dense random packing. He plotted solids fraction ρ against $1/\sqrt[3]{N}$ (where N is the number of spheres), and then extrapolated the curve to large N. He found two distinct values of the solids fraction, namely $\rho_{loose} = 0.59$ before vibrations, and $\rho_{dense} = 0.63$ after vibrations. In 1969, Scott and Kilgour [7] investigated randomly packed hard spheres by improving on the older

studies. Both random 'loose' and random close-packed densities were reported for 1/8″ plexi-glass, nylon and steel balls in air, and also with steel balls immersed in oil. A series of measurements for the random close-packed density was made using up to 80,000 steel balls with the aid of a mechanical vibrator. From the analysis of the experimental data, the solids fraction for a random close packing was found to be 0.6366 ± 0.0005.

In 1960, Macrae [30] carried out a series of experiments to investigate the significance of material properties in the packing of spherical particles consisting of steel, glass, lead shot, bronze and polystyrene. Two filling methods were employed to generate the particle beds, i.e. either via cascading or by dropping the entire particle mass. The intensity of deposition, height of drop and elasticity of the materials were shown to be important parameters affecting the bulk density. As a function of the drop height, there was an increase in solids fraction curve up to a drop height beyond which the curve flattened out. Although this was the general trend, there were quantitative differences in the curves depending on the sphere materials being used. The results obtained by varying deposition intensity were also a function of the sphere material properties. Except for the lead shot, there was a critical range of deposition intensity that produced the closest packing at the prevailing height of drop.

Since the 1960's, various computer simulation algorithms have been employed to study the packing of particles [31-36]. These algorithms generally involve various assumptions about particle motion and/or stability criteria, which stem largely from geometrical considerations by ignoring dynamic effects during the process. Realistic dynamics have been reproduced with the Discrete Element Method [37]. This technique involves the solution of the equations of motion that govern systems of interacting,

dissipative particles. Yen and Chaki [38] carried out a DEM study of the packing of fine particles that had only translational degrees of freedom, i.e., their contact model did not include a mechanism for particle rotations. A detailed DEM study of the variable affecting the packing structure of spheres characterized by the solids fraction, coordination number and radial distribution function was report by Zhang et al. [39]. They were able to demonstrate that the bulk density increases with drop height and restitution coefficient, and decreases with deposition intensity and friction coefficient, in qualitative agreement with the experimental results of Macrae [30].

Table 1.1 lists selected results from experiments and simulations in the literature.

Table 1.1 Summary of Selected Literature on Uniform Sphere Packing

ρ_{loose}	ρ_{dense}	System	Reference
0.608	0.6366±0.005	Steel spheres in cylinder	Scott & Kilgour [7]
0.605		Glass spheres in cylinder	Scott [29]
0.596		Steel spheres in cylinder	Macrae & Gray [30]
0.599	0.644	Glass spheres in cylinder	Macrae & Gray [30]
0.607	0.62	Lead spheres in cylinder	Macrae & Gray [30]
0.59		Computer Simulation	Tory, Cochrane & Waddell [31]
0.6099	0.6472	Statistical Model	Gotoh & Finney [32]
0.61		Computer Simulation	Bennett [33]
	0.634	Computer Simulation	Mason [34]
	0.6366	Computer Simulation	Jodrey & Tory [35]
0.582		Computer Simulation	Tulluri [81]
	0.628	Computer Simulation	Adams & Matheson [82]
0.606		Computer Simulation	Matheson [83]
0.582		Computer Simulation	Visscher & Bolsterli [84]
0.59 ± 0.01		Computer Simulation	Powell [85]
0.58 ± 0.05		Computer Simulation	Rodriguez, Allibert & Chaix [86]

1.2.2 Vibration-induced Fluidization

Evesque et al. [14] carried out experiments on sand piles subjected to vibrations. From observations, they found that fluidization began at the surface, which appeared to be at odds with the predictions of some analytical models. [40, 49, 50, 51]. In 1989, Thomas et al. [41] conducted experiments on sinusoidal vibrating shallow granular beds that had static depths ranging from 24μm to 30mm. The vibration frequency was 25 Hz and amplitude was a few millimeters. Glass beads with different sizes and FCC powders were used. In a thin, rectangular vessel with transparent walls, they measured the critical values of vibrational intensity $\Gamma_{cr} = a\omega^2/g$, at which shallow beds became "mobilized". Their results indicated that Γ_{cr} was very sensitive to the particle size, cohesiveness and initial packing state of the beds. For fine and aeratable particles, Γ_{cr} was significantly larger in a densely packed bed than in a loosely packed bed. During the experiments, four vibration-induced dynamic states were distinguished by the degree of fluidization as the bed depth increased. The reported that bed depth, particle properties (including restitution coefficient) were the primary factors affecting transitions from one state to another.

In 1995, Lan and Rosato [42] reported on the results of their three-dimensional DEM simulations to investigate macroscopic behavior of spherical particles that were agitated through the sinusoidal motion of the floor of the computational cell. The particles were smooth (i.e., frictionless) so that transfer of tangential momentum did not produce rotations. This was done in order to facilitate comparison with kinetic theory predictions of predications of Richman and Martin [40], and with the experimental measurements of Hunt et al. [43]. In the higher acceleration regions, the computed depth profiles of granular temperature and solid fraction were in good agreement with the

kinetic theory predictions, while for lower accelerations, the simulation results were quantitatively consistent with the experimental data of Hunt et al. In addition, the simulations captured the observations of Evesque [14], that at lower acceleration values, most of the bulk mass is near the bottom, while fluidization occurs at the surface. In a subsequent study [44], Lan and Rosato examined the critical factors required for the production of bulk convection during vibration.

In 1997, Vanel et al. [45] carried out experiments to measure the rise time T of a single large sphere (or intruder) within a sinusoidally vibrated bed. At a fixed acceleration Γ, the authors identified three distinct behavioral regimes from visual observations and from the trends of the log of the dimensionless rise time $T \bullet f$ against frequency f. The first regime was characterized by visible surface heaping and an exponential scaling of $T \bullet f$ with f. Here, the intruder was carried to the bed's surface by a strong convective flow that manifested itself by surface avalanches. In the second regime, this appeared for frequencies beyond 15 Hz and smaller than approximately 40 Hz, the surface heaping was not apparent. $T \bullet f$ varied slowly with f near 15 Hz, but this product increased more rapidly at higher frequencies. In the last regime, for which the amplitude was only a fraction of the particle diameter $a/d \leq 0.25$, the bed became very rigid and tightly packed. Here, a size dependent rise of the large intruder was seen.

In 1998, Hsiau and Pan [46] carried out a series of experiments with three types of glass beads to investigate vibration-induced states. The experiments were performed in a rectangular container (239 cm high x 1.9 cm deep) and the motion of the bed of the bed was recorded digitally via an image processing system. A displacement amplitude of 5 mm was used with relative accelerations $0 < \Gamma < 7$. Approximately 8% of the particles

were dyed black to serve as tracers. They found that the granular layers in a vertical shaker exhibited several types of motion: heaping, coherent, expansion, waves and arching. The wave and arching states were not observed for the very spherical, smooth particles, a finding that was previously reported by Hunt et al. [43].

Yang and Hsiau [47] employed the discrete element method to study convection cells in a two-dimensional vibrated granular bed consisting of glass spheres. The flow patterns and velocity vectors were consistent with 1998 experimental results of the second author. A power law relationship between the mass flow rate J and the dimensionless vibration velocity V_b was reported such that $J \propto V_b^{2.3}$ when the amplitude was constant, and $J \propto V_b^{-0.4}$ when the acceleration was fixed.

Theoretical approaches to the study of granular flows began only within the last 25 years. Ogawa [48] introduced the term "granular temperature" to quantify the dynamic behavior of particle beds in analogy with the behavior of dense gases. This concept was used by Savage and Jeffrey [49], Lun et al. [50] and Jenkins and Richman [51] to develop relatively successful kinetic-theory based models for energetic granular flow, by incorporating energy dissipation due to inelastic collisions. Jenkins and Richman [51] made use of the kinetic theory of dense gases to determine the rate at which momentum and energy were transferred between flow particles and the boundary. Richman and Martin [40] extended the previous model [51] to develop the first theoretical predictions of the solid fraction and granular temperature profiles in a top-open granular bed with a bumpy floor. Their model demonstrated a greater thermalization of the particles adjacent to the vibrating floor, and an expansion of the initial depth of the bed as a consequence of increasing the boundary fluctuation velocity. Granular temperature increased

monotonically from the top to bottom, while the solids fraction reached its maximum at an intermediate level.

1.2.3 Vibration-Induced Densification

As previously noted in Section 1.2.1, Scott & Kilgour [7, 29] used vertical vibrations to disrupt particle beds so as to produce a random close packing. They did not report the values of the vibration parameters that were used. In 1967, D'Appolonia [5] carried out similar vibration tests on air-dry sand using a mechanical vibrator that was able to produce unidirectional harmonic motion. The frequency ω range was 10 to 60 cps with amplitudes a up to 0.01″. Sand was placed in a cylindrical mold (4″ in diameter and 3.5″ high) that was vibrated until the sand volume remained constant over the last 20 minutes of the test. The change in volume of the sample was measured with a depth micrometer.

A density-acceleration plot was used to show the effect of dimensionless acceleration Γ, from which it was found that the largest density occurred at $\Gamma \approx 2$, and the density increase was minimal when $\Gamma < 1$. Additionally, they reported that dry sand with zero-surcharge required less time to reach the maximum density under the vibration for $\Gamma = 1.5$. What was unclear in the experiment was their observation that an increase in acceleration produced a decrease in compacted density.

In 1995, Knight et al. [9] carried out a systematic experimental investigation of the evolution of bulk density in a tapped granular material using a noninvasive, capacitive technique. Their apparatus consisted of mono-disperse, 2mm-diameter spherical soda-lime glass beads confined to a 1.88cm diameter Pyrex tube, which was mounted vertically on a Bruel and Kjaer 4808 vibration exciter. Four parallel plate capacitors were

arranged along the tube's length to measure the bulk density (or equivalently solids fraction) at four depth sections. The bed was prepared in a low-density initial state by flowing high pressure, dry nitrogen gas through the tube from the bottom. The initial height of the beads before tapping was 87cm, corresponding to an initial column packing density of 0.577 ± 0.005. Smooth tube walls and the low static friction reduced the occurrence of convection. A 30Hz sine wave was fed to the exciter, producing a single shake, or "tap" followed by a one-second-relaxation period. They found the evolution of solids fraction against the number of taps depended not only relative acceleration but also number of taps. At $\Gamma = 1.4$, significant relaxation was clearly observed at the base of the column, but only after an extended tapping time. However at $\Gamma = 1.8$, the behavior changed radically as the density began to immediately increase immediately, a trend that continued until $t = 200$, at which time, the rate of increase was dramatically reduced. At values of Γ greater than 2.7, the data appeared to collapse onto a single curve. Near the top of the bed, a sharp transition in densification behavior was noted between $\Gamma = 1.4$ and $\Gamma = 1.8$, similar to what was seen at the bottom of the tube. However, the difference in density between the $\Gamma = 1.8$ and $\Gamma = 2.3$ data were minimal. The data strongly suggested that the evolution of density versus the number of taps was depth dependent. Another discovery was that a steady state density was not attained for accelerations greater than $\Gamma > 2.7$ up to $t = 10{,}000$.

The authors proposed a four-parameter phenomenological model to fit their experimental data, i.e,

$$\rho(n) = \rho(\infty) - \frac{\rho_\infty - \rho_0}{1 + B\ln(1 + n/\tau)} \tag{1.1}$$

Here, ρ_∞ is the steady-state density (which is dependent on the acceleration history), τ is a relaxation time, and B is a constant that is also dependent on Γ. The relationship between the relative acceleration and packing density is contained in the parameter B, although a model for this was not specified. It is noted that this model was explained by Linz [24] who carried out an asymptotic analysis on the stroboscopic decay law (derived from his physical model of the compaction process) for the inverse ratio $\nu^{-1} \equiv \left(\frac{\nu - \nu_\infty}{\nu_o - \nu_\infty} \right)^{-1}$.

In 1998, Nowak et al. [11] extended the experiments of Knight et al. by investigating the frequency dependence and amplitude of density fluctuations as a function of vibration intensity Γ. They found at certain intensities and after long periods of vibration, the system attained a steady-state density having a well-defined average with large fluctuations. The magnitude of the fluctuations depended on the depth at which measurements were made as well as the vibration intensity (that is, an increase in Γ resulted in larger fluctuations about the mean density). In addition, they reported a rather large value of solids fraction $\rho = 0.656$ in comparison to other experiments in the literature [7, 29-35]. It is likely that this discrepancy was a consequence of the influence of the walls as the aspect ratio (particle to cylinder diameter) $d/D \approx 9.4$ was small.

In 1991, Baker and Mehta [52] used Monte Carlo simulations to investigate the structure and "dynamics" of frictionless, mono-disperse spheres subject to vibration. The continuous evolution of particle positions and velocities that occurs during a physical process is replaced by a time-ordered, discrete set of static configurations. Their study focused principally on how shaking intensity affected solids fraction and the steady-state

mean coordination number. Emphasis was placed on the role of cooperative structures within the shaken assembly, such as bridges and "holes". Their results suggested the existence of a critical acceleration Γ_c below which the solids fraction would increase with time, and when $\Gamma > \Gamma_c$, the solids fraction decreased with "time".

Rosato and Yacoub [53] carried out discrete element simulation to model the densification process experienced by a bed of frictional, inelastic spheres of diameter d in a rectangular vessel whose floor is subject to high frequency f and low amplitude $a/d <$ 0.1 sinusoidal oscillations in 1999. They selected two values of relative acceleration (i.e., 1.02 and 6.4) corresponding to $a/d = 0.1$ and $f = 20$ and 50Hz respectively to assess their influence on the coordination number and solid fraction of spheres. They found that at Γ = 6.4, the evolution of the coordination number distribution proceeded at a faster rate than what occurred when Γ = 1.02. Also evaluated was the evolution of the mean solids fraction, whose value was computed as a space-time average taken within the central region of the bed over five second time intervals. Good fits of the data to both the phenomenological model of Nowak et al. (equation (1.1) above) and the exponential decay model of Takahashi and Suzuki [54] were found. The simulations also showed that at Γ = 6.4, very little difference in solids fraction between the center and top of the bed existed, while at Γ = 1.02, the solids fraction was larger near the center of the bed. This behavior is in qualitative agreement with the reported experiments [9] in which density decreases toward the surface at $\Gamma < 1.8$, while greater homogeneity is achieved at higher accelerations.

1.3 Objectives

A survey of the literature reveals that physical experiments, computer simulations and theoretical approaches have been extensively used to investigate the random packing of particles, vibration-induced fluidization and densification. However, the phenomenon of densification under continuous vibrations appears to have received relatively little attention. This dissertation presents an experimental investigation coupled with analogous discrete element simulations in an effort to understand the conditions favorable to the occurrence of densification. A large parameter space is taken into account, consisting of particle properties, containment geometry, initial poured states, and a wide range of vibratory amplitudes and frequencies.

Several important insights have been gained from the results of this work, that is,

- identification of the factors that control the pouring process,
- a quantification of the system's dynamic steady state,
- recognition of factors to predict the final relaxed solids fraction, and
- the relationship between the dynamic and final relaxed states.

1.4 Outline of Dissertation

Chapter 1 presents a concise overview of some of the relevant literature on the packing of particles, vibration-induced fluidization and densification, followed by the motivation and specific objectives and structure of the investigation. Chapter 2 describes the experimental results obtained for mono-disperse acrylic spheres and polyethylene pellets, which provide a backdrop for the computer simulations. Chapter 3 provides an overview the discrete element method, the algorithm and hard sphere and soft sphere models.

Details of the simulation code, including the integration method, force models, and definitions of various computed physical quantities are given in Chapter 4. Chapter 5 consists of the results from the simulation of pouring process with different two normal force contact models, and the results are compared with those from other experiments and simulations [7, 30, 55]. Chapter 6 shows the effects of various parameters on the dynamic steady state of the system before the final relaxation process. Here results are qualitatively compared with the experiments of Thomas et al. [41]. In Chapter 7, densification results are discussed, comparisons are made with specific physical experiments [5], and a relationship between dynamic and relaxed state is established. In addition, the evolution of overall or bulk solids fraction is reported that includes an examination of the particle structure that develops against the solid wall, and comparisons with the work of others. Lastly, the summary and conclusions are present in Chapter 8, and some suggestions for future research are given.

CHAPTER 2

PHYSICAL EXPERIMENT

Densification of bulk solids by vibration often occurs in industrial solids handling systems, and for different materials at different vibration conditions, the densification processes can be very different. In this chapter, two series of physical experiments using acrylic spheres and polyethylene pellets are carried out to highlight the difference. Additionally, the results from these experiments supply physical data that can be used for comparison purposes with the computer simulations that are discussed in subsequent chapters.

Before imposing vibration on the granular bed, an initial poured particle bed is needed. In order to minimize the effects of the initial configuration, the pouring process should be carried out so as to produce as best as possible almost same initial state for each trial.

2.1 Experimental Equipment

The experimental system consists of a fixed acrylic cylinder, several acrylic rings and a piston mounted onto a Bruel & Kjar shaking head. Figure 2.1 diagrams the apparatus, whose components are as follows:

1) Bruel and Kjar Vibration Exciter Control Type 1050
2) Bruel and Kjar Power Amplifier Type 2707
3) Bruel and Kjar Vibration Exciter type 4801/Vibration Head Type 4812
4) Accelerometer

5) Kistler Dual Mode Amplifier Type 5010

6) Acrylic cylinder

7) Fixing Plate

8) Exciter plate

9) Electrical Balance Type XP-1500

10) Acrylic particles with different diameters.

11) Polyethylene pellets with different shapes and friction coefficient.

12) Colorful sand with different diameters.

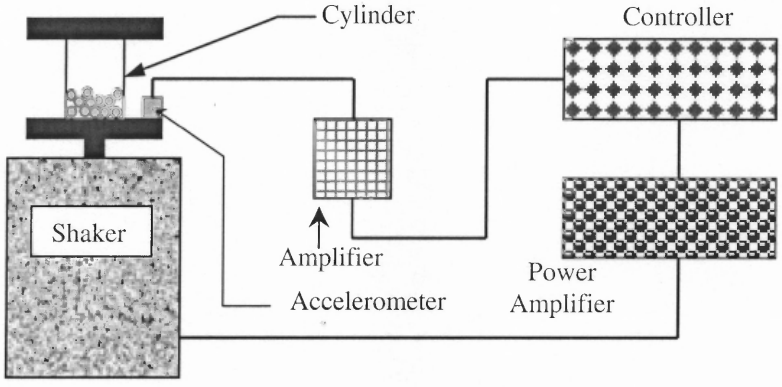

Figure 2.1 Schematic drawing of vibration assembly.

An accelerometer mounted to the shaking platform provides feedback so that precise control over the excitation amplitude and frequency is obtained. The displacement of the piston is sinusoidal in nature.

2.2 Particle Pouring Experiment

The objective of first stage of the experiment is to obtain an initial poured particle bed of acrylic spheres. Multiple trials were conducted on uniform systems over a number of different particle diameters. The procedures for this part of the experiment is as follows:

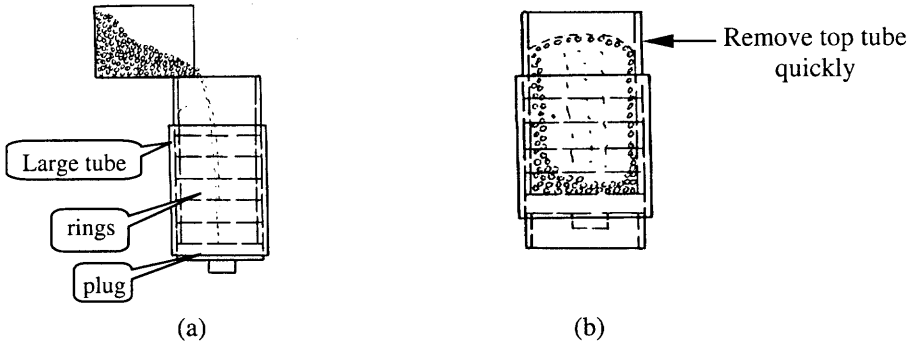

Figure 2.2 Pouring procedures.

- Insert five rings (ID2.5″, OD2.75″, h = 0.75″) in a larger tube (ID2.75″, OD3.00″, h = 5.5″) and use a plug as a bottom. The top of rings should be lower than the top of tube.
- Weigh the rings, plug and tubing separately.
- Insert a tube with same ID and OD as that of the rings from the top, and then pour particles with certain diameter into the container until the particles reach the top of bigger tubing (see Figure 2.2 (a)).
- Use a tube with same ID and OD as those of rings; slowly push the particles bed and rings from the bottom until the top surface of rings meets with that of the big tube (see Figure 2.2 (b)).
- Quickly remove the top tube to make a flat surface.
- Weigh the total assembly (including particles).
- Calculate the weight of particles.
- Repeat the experiment for 20 times.
- Determine the average weight of particles.

- Calculate the overall solids fraction and its deviation.
- Change the size of particles and repeat the experiments.

In the pouring experiments, five different sphere diameters (d) are used. Denoting D as the cylinder inner diameter, the aspect ratio is given by D/d.

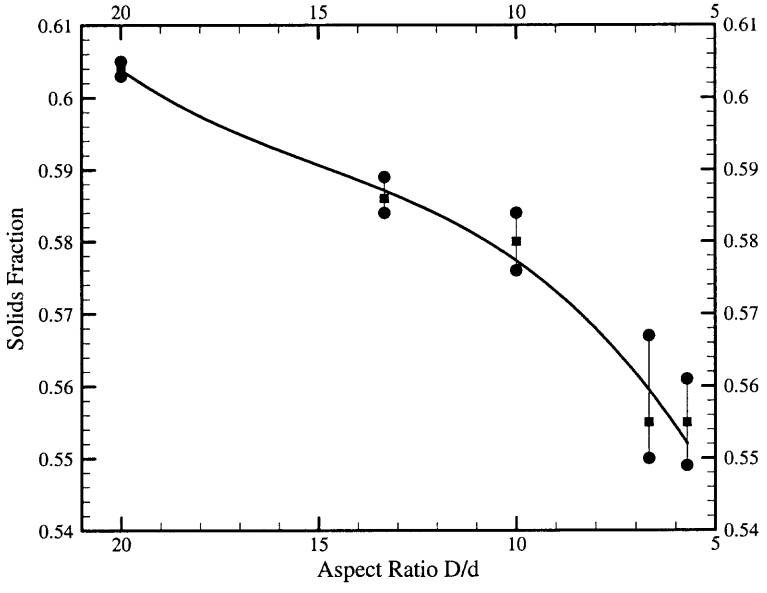

Figure 2.3 Solids fraction versus aspect ratio D/d for the pouring experiment. The vertical bars represent the spread of the data over 20 trials and the solid curve is included to show the overall trend.

From Figure 2.3, it is clear that with the increase of the aspect ratio, the poured solids fraction increases. The reason for this is that near the container wall, there are more voids, which affect the overall poured solids fraction. From the error bars, it is clear that the use of 1/8″ acrylic spheres gives the most stable initial poured state because the error bar is the smallest. Thus the 1/8″ spheres are chosen for the vibration experiments.

2.3 Vibration Experiment using 1/8″ Acrylic Spheres

After producing the initial poured particle bed, vibrations are imposed to this system under different conditions by selecting various amplitudes and frequencies.

The cylinder is filled with mono-disperse acrylic spheres of diameter d = 1/8″. The initial undisturbed bed depth is H = 3.75″, and the bed aspect ratio is H/D_{cy} = 1.5. A sinusoidal signal is used to vibrate the piston over a range of amplitudes $0.04 \leq a/d \leq 0.24$ and frequencies between 25Hz–100Hz, corresponding to relative accelerations Γ between 0.94 and 11.54. The vibration time is 10 minutes. In order to reduce the buildup of static charge, the inside tube wall and particles are treated with a household anti-static agent. In summary, the following procedures are followed.

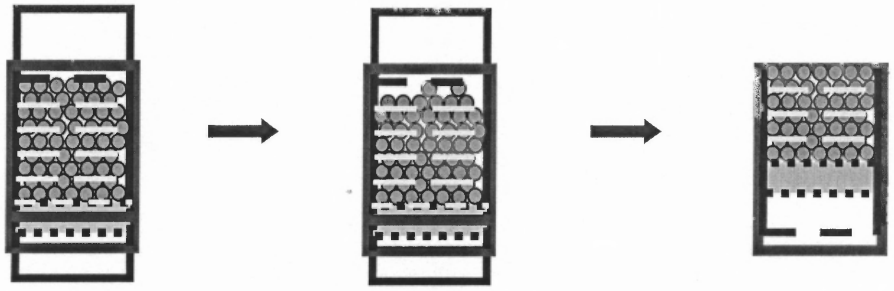

Figure 2.4 Vibration experimental procedures.

- Obtain the initial poured bed.
- Attach the particle bed to the vibrator, and then vibrate it at different frequencies and amplitudes for 600s.
- Because of the difficulty of measuring the heights of the compacted particle bed, remove the top ring to produce a flat surface, and then to calculate the overall average solids fraction.
- Use the following equation to calculate the improvement of solids fraction:

$$\text{Improvement of Solids Fraction} = \frac{\rho_2 - \rho_1}{\rho_1} \times 100(\%) \tag{2.1}$$

where ρ_1 is the poured solids fraction, ρ_2 is the solids fraction after 10 minutes of vibration and relaxation. The detailed experimental parameters are shown in the **Appendix,** while the experimental results are summarized in Figures 5 ~ 11.

From Figure 2.5, it can be seen that when a/d = 0.04, the solids fraction increases with the relative acceleration Γ, but the improvement is relatively slow. When $\Gamma \leq 1$, the total particle bed just moved with the floor and no relative movement could be observed, including convection. However, when Γ was slowly increase beyond approximately 2, motion of the particle at the surface was visible.

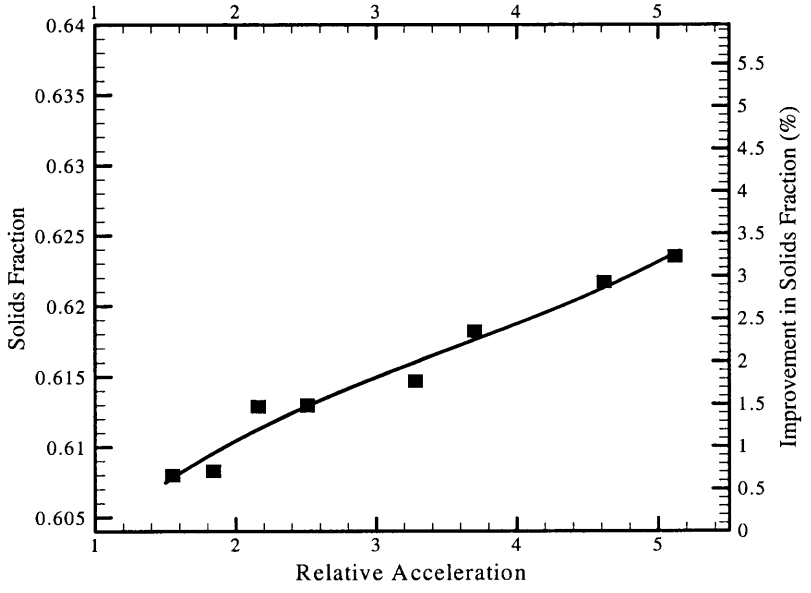

Figure 2.5 Solids fraction versus relative acceleration at a/d = 0.04. The solid line is a best fit curve to show the trend.

When *a/d* is between 0.06 and 0.12 (Figures 2.6 to 2.9), the particle bed attains a "maximum density" ($\rho \approx 0.636$) when Γ is between 5 and 7, followed by an expansion upon a further increase of Γ.

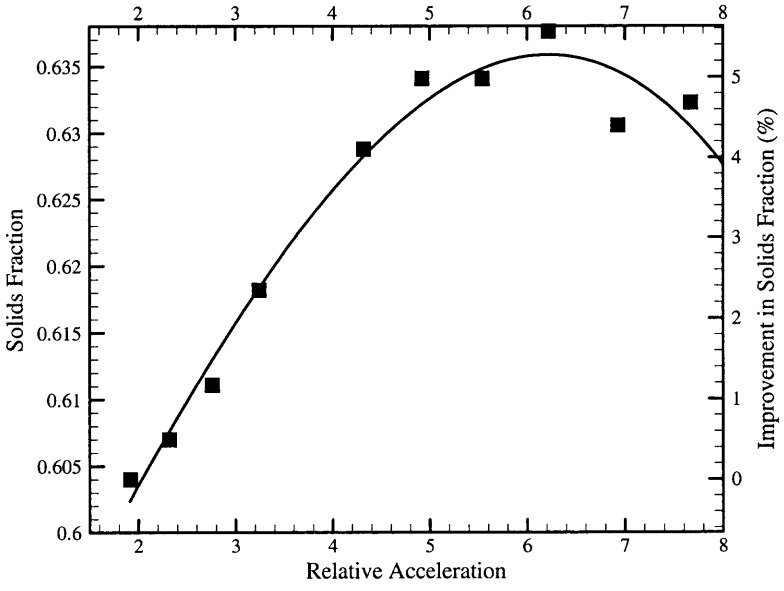

Figure 2.6 Solids fraction versus relative acceleration at *a/d* = 0.06. The solid line is a best fit curve to show the trend.

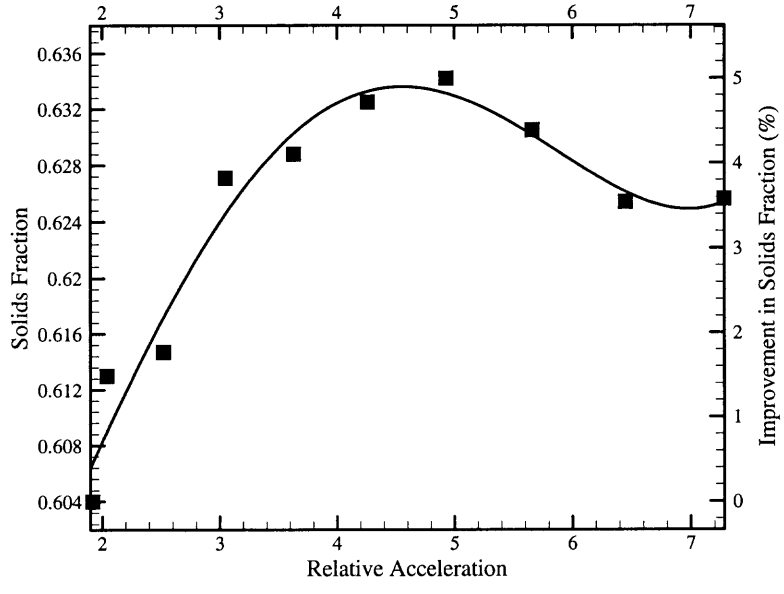

Figure 2.7 Solids fraction versus relative acceleration at *a/d* = 0.08. The solid line is a best fit curve to show the trend.

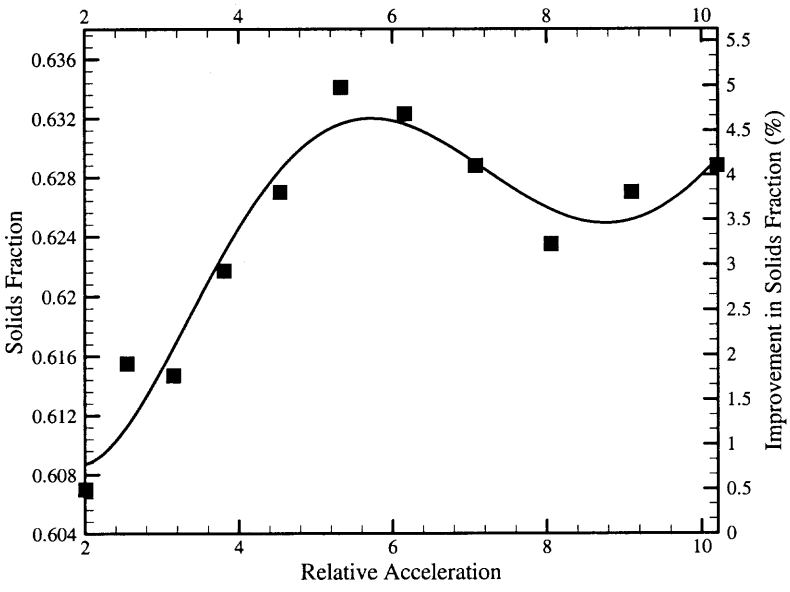

Figure 2.8 Solids fraction versus relative acceleration at $a/d = 0.10$. The solid line is a best fit curve to show the trend.

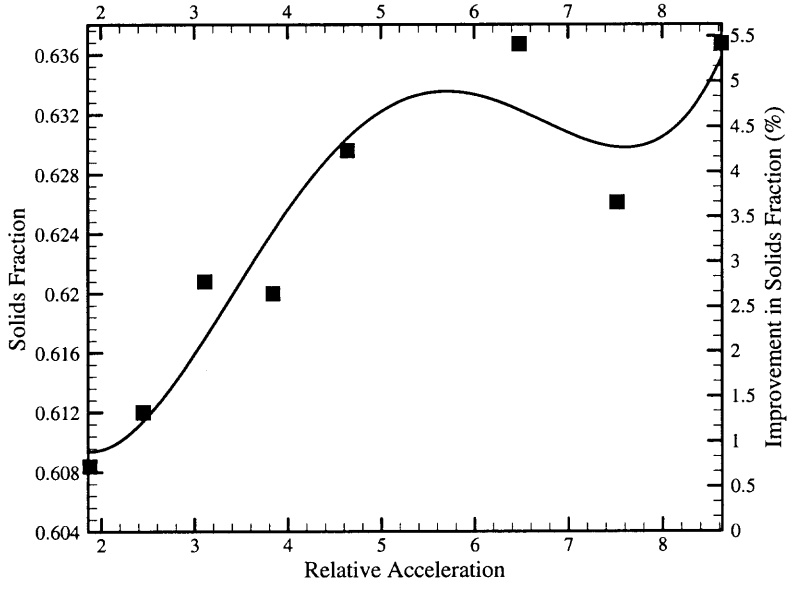

Figure 2.9 Solids fraction versus relative acceleration at $a/d = 0.12$. The solid line is a best fit curve to show the trend.

Here, convection was clearly noticed near the boundary and this motion became stronger as Γ was increased. This result suggests that densification dominates at small Γ, and after reaching a peak, convection effects begin to appear which reduces the bulk solids fraction.

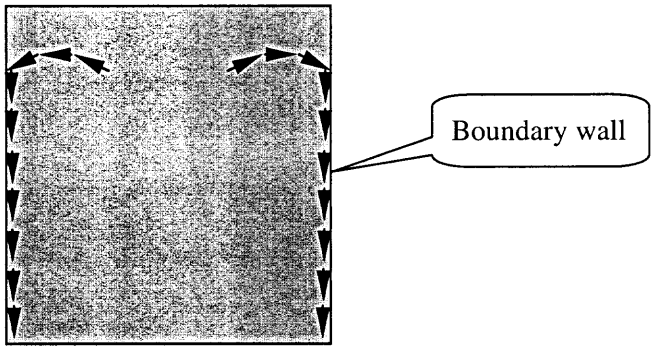

Figure 2.10 Fluidization pattern during vibration.

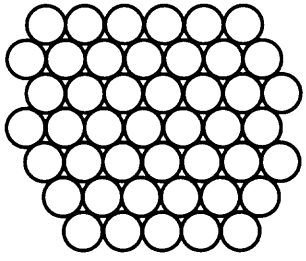

Figure 2.11 Structure seen from sidewall.

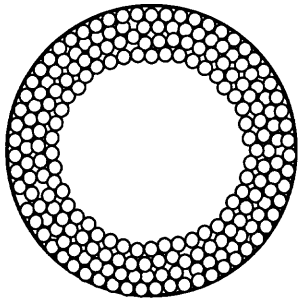

Figure 2.12 Structure seen from top.

At the point when the system has reached its "maximum density", a tightly packed particle structure (depicted in Figure 2.11) adjacent to the cylinder wall was formed. The arrangement as seen from the top is sketched in the Figure 2.12. Careful observations during the experiment seemed to indicate that the wall structure could be destroyed if a strong bulk convection was present during the vibrations. It is conjectured

that the rearrangement of particles adjacent to the cylinder walls that is promoted by convection is an important contributor to achieving a substantial (about 5%) improvement in bulk solids fraction in these experiments. However, it is clear that the cylindrical geometry and aspect ratio (D/d) are key factors that facilitated the easily obtained maximum (between 0.63 and 0.64) in solids fraction. Along these lines, Nowak et al [11] also pointed that compaction process in their experiments was affected by the aspect ratio (D/d = 9.4) that was used. In fact, they reported a bulk solids fraction of ρ = 0.656, which is substantially larger than the value associated with a random close packing ρ = 0.6366 [7].

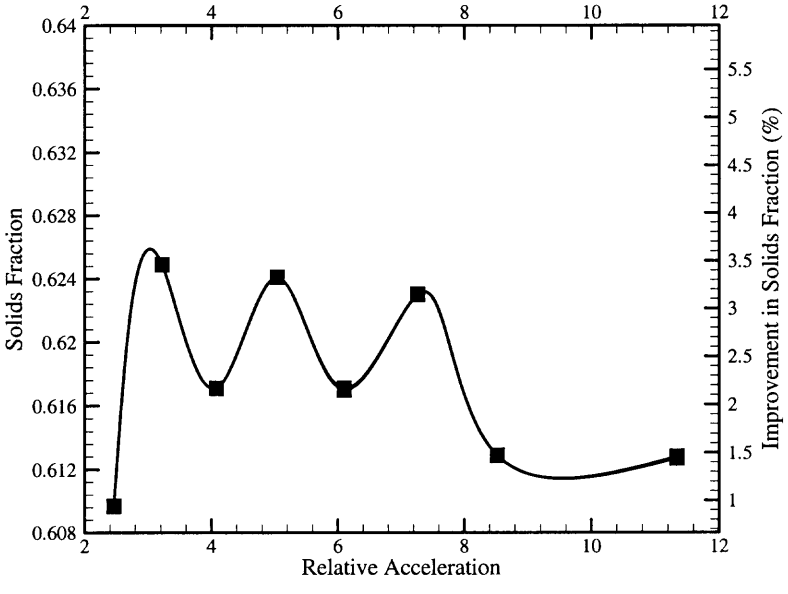

Figure 2.13 Solids fraction versus relative acceleration at a/d = 0.16. The solid line is a best fit curve to show the trend.

When *a/d* is 0.16 Figure 2.13 shows several oscillations of the solids fraction as a function of the relative acceleration with some moderate improvement over the initial poured state, in contrast to the behavior shown in Figures 2.6 – 2.9. It is noted that bulk convection was visible during these experiments.

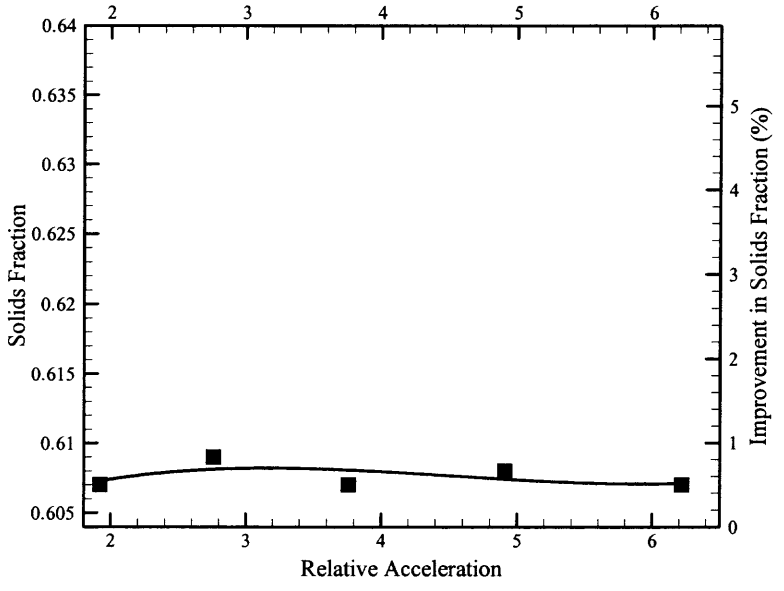

Figure 2.14 Solids fraction versus relative acceleration at *a/d* = 0.24. The solid line is a best fit curve to show the trend.

When *a/d* is 0.24 (Figure 2.14), the solids fraction remains almost constant. Very energetic particle movement was noted, although bulk convection was not at all apparent. At this amplitude, expansion of the bed depth occurred that is characteristic of a fluidized granular system.

2.4 Vibration Experiment with Polyethylene Pellets

2.4.1 Materials' Description

Three kinds of materials are used, designated as #1, #2, and #3 for reference.

Material #1: polypropylene, >= 99%

Appearance: 1/8″ diameter pellets with irregular shapes; whitish color

Solid density: 0.88–0.92g/cm^3

Material #2: 1-Hexene, polymer with ethane, >=99%

Appearance: 1/8″ diameter pellets, like a cylinder, more regular than 1#

Solid density: 0.89–0.965g/cm^3

Material #3: 1-Hexene, polymer with ethane, >=99%

Appearance: 1/8″ diameter pellets, like an oval, with very smooth surface

Solid density: 0.89–0.965g/cm^3

2.4.2 Experimental Procedures

The apparatus used here is depicted in Figure 2.2 (or Figure 2.4).

- Insert five rings (ID2.5″, OD2.75″, h = 0.75″) into the large tube (ID2.75″, OD3.00″, h = 5.5″) and use a plug as a bottom. The top of the rings should be lower than that of tube.
- Insert a tube with the same ID and OD as those of the rings from the top, and then pour particles into the container until they reach the top of the large tube. Then using a tube with same ID and OD as those of the rings, slowly push the particle bed and rings from the bottom until the top surface of the rings meets with that of large tube.
- Quickly remove the top tube to produce a flat surface.
- If the surface has been damaged (i.e., not flat in some places), add some particles to make the surface as flat as possible.
- Vibrate the poured bed using various frequencies and amplitudes. After finishing the vibration, measure the maximum, minimum and medium distances between the top of the rings and the surface of the particle bed.
- Repeat the experiment for 3–4 times.
- Calculate the improvement of solids fraction using equation (2.1)

2.4.3 Observations During the Experiment

The first interesting phenomenon is the transition of the top surface during the vibration. The slope angle is introduced to describe this transition (see Figure 2.15). The relation between slope angle and relative acceleration Γ at amplitudes $a = 0.005''$, $0.01''$ and $0.02''$ are displayed in Figures 2.16 – 2.18, respectively.

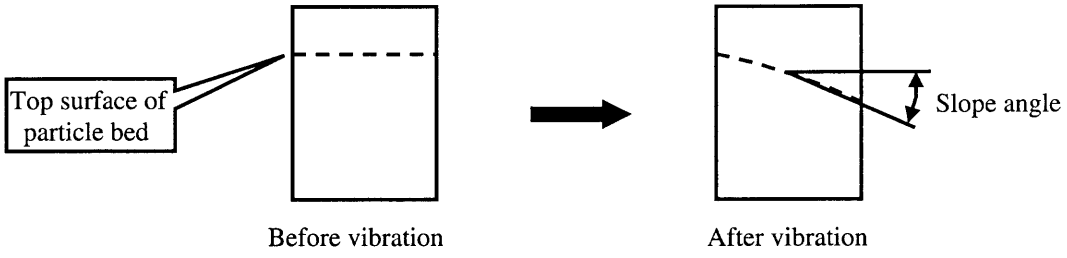

Figure 2.15 Top surface of particle bed.

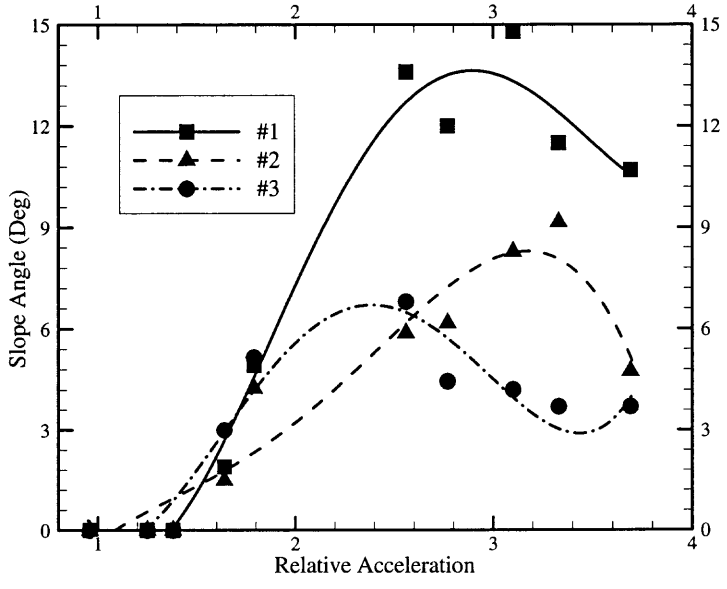

Figure 2.16 Relationship between relative acceleration Γ and surface slope angle at amplitude $a = 0.005''$.

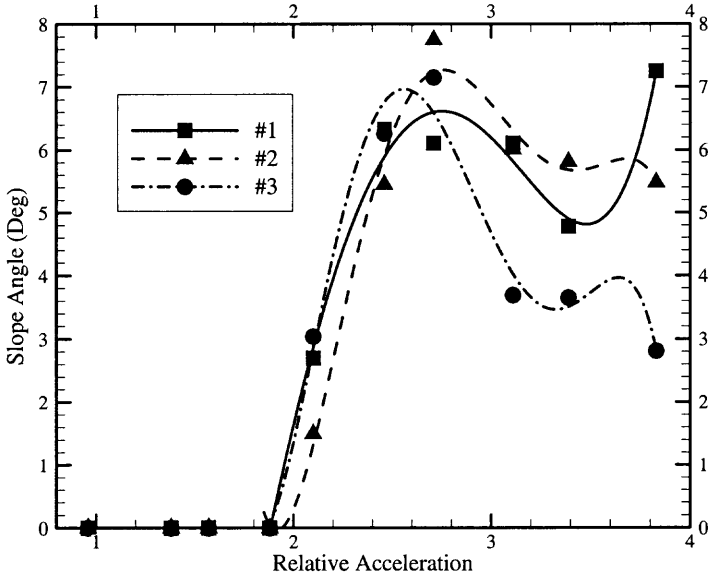

Figure 2.17 Relationship between relative acceleration Γ and surface slope angle at amplitude $a = 0.01''$.

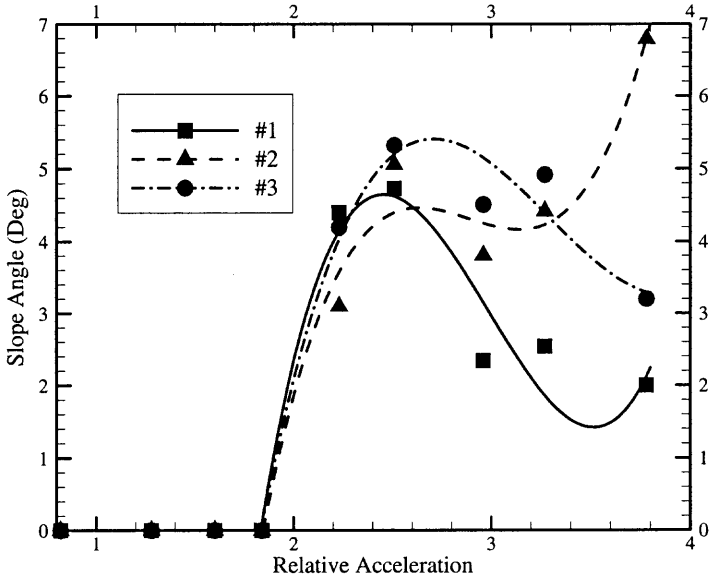

Figure 2.18 Relationship between relative acceleration and surface slope angle at amplitude $a = 0.02''$.

Because the inner surface of the rings is very smooth, convection between the particles and inner surface is not observed. In addition, particle movement at the surface of the particle beds occurs readily under the large relative acceleration ($\Gamma \approx 2$). When the relative acceleration Γ is less than 1.5, the slope angles are all smaller than 3°, when the relative acceleration Γ reaches about 2.5 – 3.0 (see Figures 2.16 – 2.18), the slope angle reaches its repose angle, then slope angle decreases with the increase of relative acceleration Γ.

2.4.4 Densification of Particle Beds

The results of improvement in bulk density versus relative acceleration Γ are presented in Figures 2.19 – 2.22.

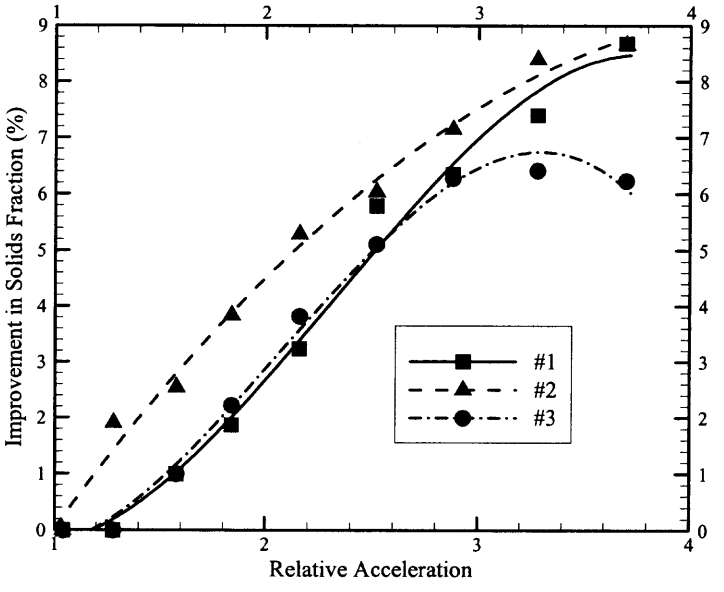

Figure 2.19 Relationship between relative acceleration and improvement of solids fraction at $a = 0.005''$.

From the Figure 2.19, where amplitude a is equal to 0.005", materials *#1* and *#2* show a continuous improvement in solids fraction. However, for material *#3*, when $\Gamma \approx 3$, the solids fraction reaches its "maximum value", and then drops only very slightly with a further increase in relative acceleration.

From the Figures 2.20 to 2.22, it can be seen that at the lower Γ values, the solids fraction increases with the relative acceleration. Upon attaining their "densest" state, the beds all experience a decrease in density with further increase in the relative acceleration. It can also be seen that material *#2* is more sensitive to the vibration in the sense that it responds to the vibration more quickly. However, material *#1* exhibits the greater improvement in bulk solids fraction. An inspection of the data points for Material *#3* indicates that it attains its largest solids fraction at a smaller acceleration value than the other pellets.

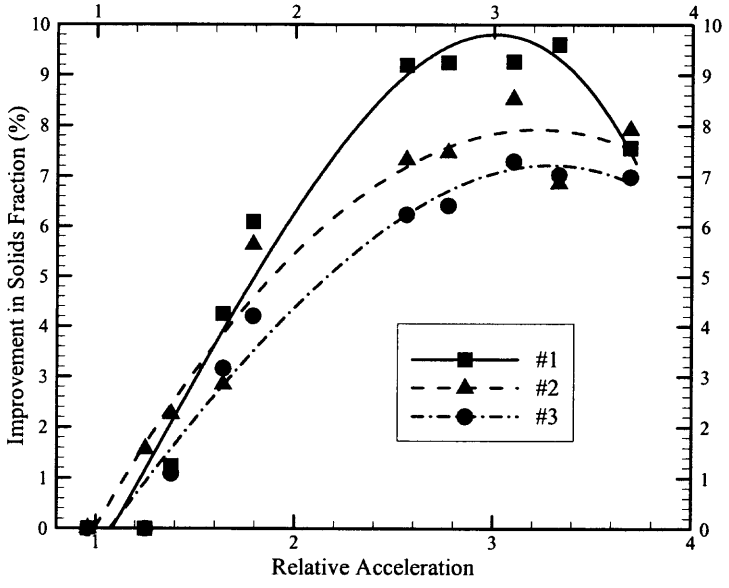

Figure 2.20 Relationship between relative acceleration and improvement of solids fraction at $a = 0.01$".

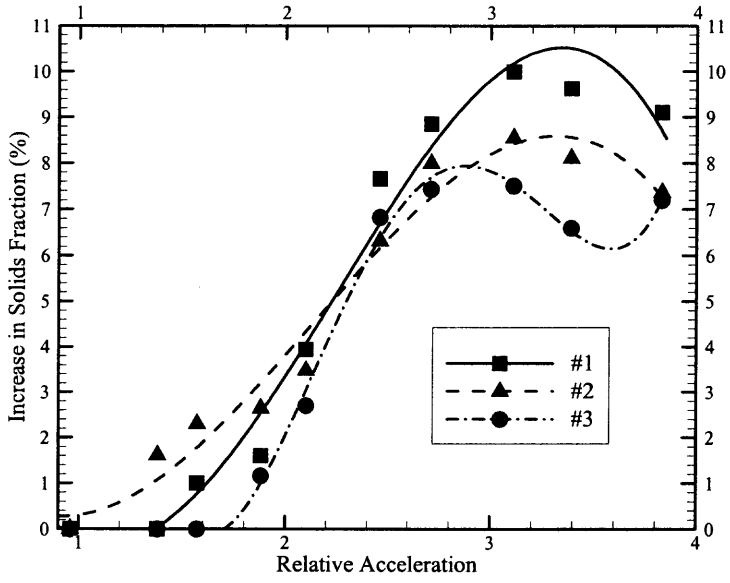

Figure 2.21 Relationship between relative acceleration and improvement of solids fraction at $a = 0.015''$.

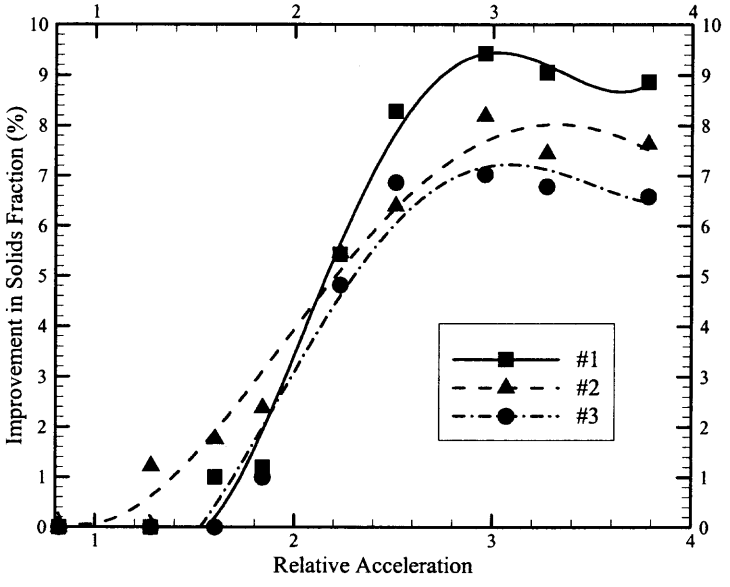

Figure 2.22 Relationship between relative acceleration and improvement of solids fraction at $a = 0.02''$.

2.4.5 Analysis of the Experimental Results

The following reasons are believed to contribute to the phenomenon just described.

(1) Material *#1* has the most irregular shape and thus the largest dynamic friction coefficient. Hence, the material finds it difficult to respond to low relative acceleration because not enough energy is supplied to destroy its initial structure. But when the energy reaches a certain level, the particles may rotate and translate to a greater extent than the other materials used in the experiments. In addition, the initial (poured) bulk density is the smallest compared with the other materials. This may be why material #1 shows the greatest improvement in the bulk solids fraction with acceleration compared with the other materials.

(2) Material #2 appears to be the most sensitive to the vibration in that the curves show the earliest response as compared with the other materials.

(3) Material *#3* has the largest flow ability because of the rather ellipsoidal shape of the particles. This feature is in line with the trends in Figures 2.20 to 2.22, i.e., that the system attains its maximum solids fraction at lower relative accelerations compared with the other materials. The data also indicates that the system first begins to respond to the vibrations at higher acceleration values, or in other words, it requires greater kick to initiate the process of particle rearrangement so that the solids fraction increases.

2.5 Observations and Results

For mono-disperse acrylic spheres $d = 1/8''$:

1) The aspect ratio d/D affects the poured solids fraction, with the increase of d/D, the solids fraction decreases because of the effect of the container wall.

2) The displacement amplitude a influences densification behavior as a function of acceleration. When a/d is between 0.06 and 0.12, the particle bed attains a "maximum density" for relative accelerations Γ between 5 and 7. When a/d is 0.16 and 0.24, the particle bed does not attain a "maximum density" within 600 seconds.

3) Depending on the selected vibration parameters, the occurrence of bulk convection can either accelerate or hinder the densification process.

For multi-disperse polyethylene pellets:

1) Particle shape and friction coefficient have significant effects on densification process and fluidization during the vibration.

2) Three different materials show different behaviors during vibration.

3) The beds of polyethylene pellets can attain a 9% improvement in solids fraction which is significantly larger than the results for the spherical particles.

CHAPTER 3

DISCRETE ELEMENT METHOD REVIEW

3.1 Introduction

Computer simulations using discrete particles provide a means of directly accessing the detailed dynamics of the system so that macroscopic quantities can be calculated. For problems involving the flow of dry granular materials, these methods are extremely important and useful in providing microscopic information that cannot be easily obtained in physical experiments. Because constitutive relations needed for continuum modeling of granular systems over the wide range of observe phenomena are scarce, particle simulation methods serve to bridge the gap by providing a means of uncovering the physical mechanisms governing a problem.

The discrete element method (DEM) has its origins within the physics community involved with molecular dynamics modeling of liquids and gases [Alder, etc.]. The method is based on the numerical solution of Newton's equations of motion for systems of interacting particles. In contrast to real molecular systems in which collisions are energy conservative, granular particles dissipate energy when they collide. Hence the incorporate of mechanisms that produce dissipation is an inherent aspect of DEM simulations.

The development of the method in the early 1970's is attributed to Cundall [37], although it is really an outgrowth of molecular dynamics methods used by the physics community. With advances in computing technology, applications of the DEM have seen tremendous growth in investigations on a variety of important solids handling problems,

such as segregation, mixing and agglomerate degradation [56, 57] and shear flows [58, 59]. In dry particle systems (i.e., those for which there is no fluid phase), solid-solid interactions provide the means of transferring momentum and energy. Consequently, all discrete element simulations feature contact detection algorithms together with contact interaction models. Examples are the two-dimensional polygonal particles of Walton [60] and Hopkins [61], and three-dimensional polyhedral particles of Ghaboussi and Barbosa [62]. In general, DEM simulations can be categorized by the type of contact model, either "hard" or "soft".

3.2 Hard Sphere Models

Hard sphere interactions can be defined as those in which collisions occur instantaneously (without deformation of the impacting objects). Energy loss in is achieved through restitution and friction coefficients which, in combination with the pre-collisional particle velocities, yield post-collision velocities.

The basic algorithm of a rigid contact model is shown in Figure 3.1 and the processes are as follows: after starting the simulation, the time at which the first collision occurs is computed from the trajectories given by simple time functions. The positions and velocities of all the particles are updated to that time. The collision is then carried out, and the time for the next collision is found. Then, as before, particle positions and velocities are updated to this next collision time, and the algorithm continues. Statistics can be accumulated as the simulation proceeds and computations of average properties carried out at selected times.

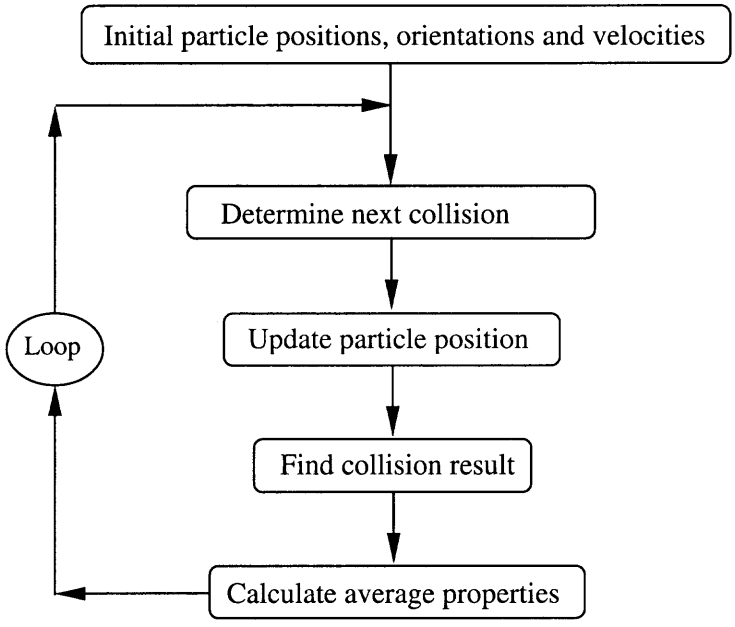

Figure 3.1 Algorithm of hard sphere model.

The simulation using this method is very efficient at low solid concentrations where collisions are infrequent. The hard sphere model cannot be applied directly to situations involving stagnant zones or where particles are in contact for long durations of time. In such cases, modifications can be made to the algorithm when particles are in close proximity.

3.3 Soft Sphere Model

In contrast to hard spheres where collisions are instantaneous, soft spheres go through deformations during a collision so that the contact time is finite. Although binary (two-body) interactions are considered, a particle can be in contact with several particles simultaneously. The exact form of the contact duration depends on the particular collision model being used, although it generally depends on contact stiffness. The interaction

force is a function of a small, allowed overlap between the colliding particles as well as the material properties.

At any time instant, a particle may be in contact with several others so that there is a net force given by the vector sum of the binary or pair interactions. Thus, detailed information about the net force experienced by each particle at discrete times is available. The system is marched forward in time by numerical integration of the equations of motion (i.e., Newton's laws for translation and rotation). The time step for this integration is generally small and can range from 10^{-4} to 10^{-8} seconds, depending on the particles being simulated. The simplified flowchart of Figure 3.2 depicts the framework of the simulation procedure. A book keeping device that tracks contacts as they are formed and broken is denoted as the "link-list". The frequency at which this list is updated depends on the mean solids fraction of the flow.

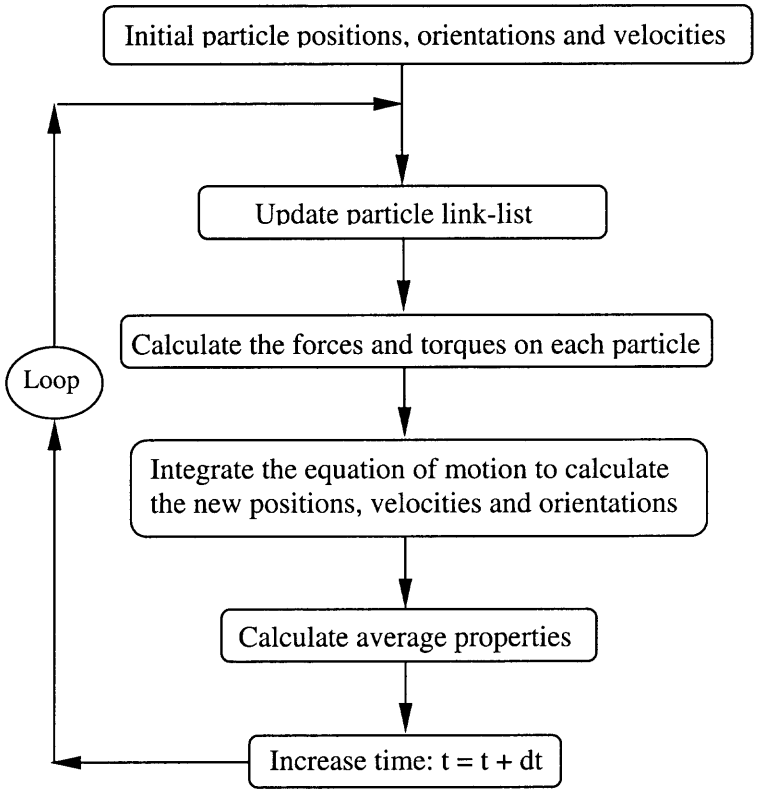

Figure 3.2 Algorithm of soft sphere model.

For dense systems, the use of soft spheres is more attractive since it is not necessary to introduce any corrections to account for long duration contacts between particles. From the perspective of computational intensity, soft sphere models are not efficient for sparse (i.e., low solids fraction) systems where collisions are infrequent. This is the case because particles trajectories are advanced through rather small times steps via the numerical integration of the motion equations. Despite this drawback, soft sphere models are used quite often because of their robustness in handling the gamut of quasi-static to dynamic flow regimes, as well as a wide variety of different materials.

CHAPTER 4

3D DYNAMIC SIMULATION MODEL

4.1 General Structure

The numerical simulations presented in this dissertation employs soft spheres since this method can incorporate elaborate collision interactions, as well as handle static assemblies of particles. Minor modifications to an existing three-dimensional code developed by Walton and Braun [8] are made for the purposes of this investigation. The code itself consists of 16 subroutines that may be partitioned as follows. Note that routine names are shown below in *italics* typeface.

A: Input and initialization of simulation parameters

Datain, Bound, Init, Findrad

B: Inter-particle force calculation

Force, Update

C: Intergrations

Initstep, Integ1, Integ2

D: Diagnostic calculations

Datasave

Subroutine *Datain* reads in the input file *i3ds* that contains information about the total number of particles and their corresponding radii, the cell size, the maximum time, the pouring time, the type of boundaries, the material properties and the vibration parameters. The input file *i3ds* also contains the value for the "search distance" to be used later in the calculation of the particles' link lists. Subroutine *Bound* creates the

configuration for the cell boundaries based on the data read in from *i3ds*. This subroutine can create cell boundaries in the x-z plane and/or in the y-x plane with periodic boundaries in the x-direction. It can also create cylindrical boundaries. In the studies to be presented here, only the floor of the cell is vibrated in the y-direction, i.e. the cell walls remain stationary. Subroutine *Init* will randomly assign initial particle centers and deviatoric velocities to all free (non-boundary) particles. The particle centers assigned are always checked to ensure that boundary conditions are satisfied. The particle radii, which initially have zero values, are expanded to their assigned values in subroutine *Findrad*. After the expansion of the particle radii, a link list for each particle is created and updated by subroutine *Update*. In each particle's link list, the information about all the particles that lie within a surrounding "search distance" is stored. Any overlap between particles is translated as interactive forces that are calculated in subroutine *Forces*. The equations of motion are then integrated, using a Verlet leapfrog algorithm [65], in subroutines *Integ1* and *Integ2* using a time step that is computed in subroutine *Initstep*. For the purpose of gathering statistics, short and long term average parameters are initialized in subroutines *Initcum1* and *Initcum2*, respectively. Subroutine *Diagnos2* is called to compute various quantities of interest, such a mean velocity as well as other transport properties. The output data is then stored in labeled files specified by subroutine *Datasave*.

4.2 Collisional Force Model (Non-Cohesive)

In the soft sphere model, solid-solid interactions contain three basic features.

- a mechanism to calculate normal force at the contact point that pushes the particle apart.
- a mechanism to provide energy dissipation during the collision.
- a mechanism to calculate tangential force that acts on the particle surfaces.

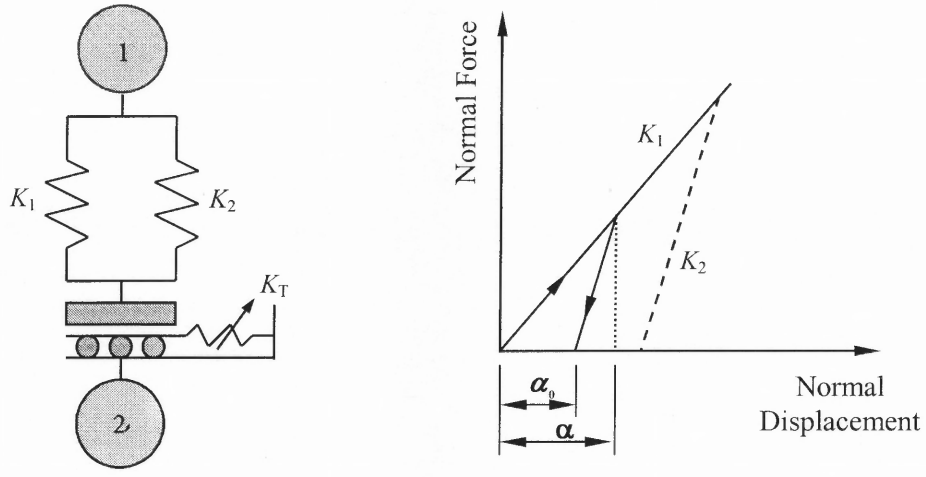

Figure 4.1 Partially latching-spring model.

The partial latching-spring model (Figure 4.1) was developed by Walton-Braun [8, 63, 64] for an elastic-plastic material. They used a "latching spring" that loads with one spring constant and unloads with another as a way of incorporating the energy dissipation. It was found that this to be closer to results of elastic-plastic finite element modeling of impact of spherical particles.

In this model, the loading resistance force is given by a linear spring, with the spring constant denoted by K_1. A stiffer linear spring with constant K_2 is used during the unloading process. In the case where the restitution coefficient is independent of relative

normal impact velocity, the relationship between e, K_1, K_2 can be shown [Lan's dissertation] to be given by,

$$e = \left(\frac{K_1}{K_2} \right)^{\frac{1}{2}} \tag{4.1}$$

During a collision, the normal force obeys,

$$\begin{cases} N_L = K_1 \alpha & \text{for loading} \\ N_U = K_2(\alpha - \alpha_0) & \text{for unloading} \end{cases} \tag{4.2}$$

where α is the relative approach (overlap) after initial contact, and α_0 is the value of residual overlap where the unloading curve goes to zero. Further details can be found in [8, 63, 64].

The tangential force model used here is incrementally slipping friction model also developed by Walton and Braun [8, 63, 64]. The idea is that the tangential stiffness K_T of a contact (in the direction parallel to the friction force) decreases with tangential displacement until it is zero, at which point full sliding occurs. The effective tangential stiffness, K_T is given by

$$K_T = \begin{cases} K_0 \left(1 - \dfrac{T - T^*}{\mu N - T^*} \right)^{\gamma} & \text{for slip in one direction } (T \text{ increasing}) \\ K_0 \left(1 - \dfrac{T^* - T}{\mu N + T^*} \right)^{\gamma} & \text{for slip in the other direction } (T \text{ decreasing}) \end{cases} \tag{4.3}$$

where T is the total tangential force; μ is the coefficient of friction; N is the total normal force; γ is a fixed parameter usually set to 1, and T^* is the loading reversal value, which is initially zero, and then subsequently set to the value of the total tangential force, T, wherever the magnitude changes from increase to decrease, or vice versa. It is scaled in

proportion to any change in the normal force from the previous time step. K_0 is the initial tangential stiffness assigned by the equation,

$$K_0 = \begin{cases} \tau K_1 & \text{for loading} \\ \tau K_2 & \text{for unloading} \end{cases} \tag{4.4}$$

where τ is the ratio of tangential and normal stiffness, a parameter that is normally less than unity. The new tangential force T' (parallel to friction force) is given by the expression

$$T' = T + K_T \Delta s \tag{4.5}$$

where Δs is the amount of relative surface displacement between the contact particles during time step Δt.

Thus, in order to calculate the total tangential force acting between each pair of particles, it needs to keep only two history dependent quantities, T and T^* from one time step to the next. The simulation model assumes that the displacements from one time step to the next step are relatively small.

4.3 Numerical Method

The particle translational and rotational accelerations in y direction are calculated by Newton's law,

$$\begin{cases} \dot{v}_y^n = \dfrac{F_{iy}^n}{m_i} \\ \dot{\omega}_y^n = \dfrac{M_{iy}^n}{I_i} \end{cases} \tag{4.6}$$

where the superscript n refers to the current time step; $m_i = \frac{1}{6}\pi d_i^3 \rho$ is the mass of particle i, where d_i is the diameter of particle i, and ρ is the material density. $I_i = \frac{1}{10} m_i d_i^2$ is the mass moment of inertia, while F_{iy} and M_{iy} are the inter-particle force and momentum, respectfully, acting on the particle i. The new velocities and positions of N particles are found by integrating the Eq. 4.6 via a leap-frog method [65] using a backward Euler approximation at $t = 0$. For the translational motion (rotation equations are analogous), the following equations can be obtained,

$$\begin{cases} \mathbf{v}_i^{t+1/2} = \mathbf{v}_i^{t-1/2} + \dfrac{\mathbf{F}_i^t}{2m_i}\Delta t \\ \mathbf{x}_i^{t+1} = \mathbf{x}_i^t + \mathbf{v}_i^{t+1/2}\Delta t \\ \mathbf{v}_i^{-1/2} = \mathbf{v}_i^o - \dfrac{\mathbf{F}_i^o}{4m_i}, \end{cases} \quad t \geq 0,\ i = 1, 2, \cdots N, \quad i = 1,2,\ldots N \tag{4.7}$$

where $\mathbf{F}_i$ is the net force on the i^{th} particle.

4.4 Time Step and Material Properties

The time step Δt used in this study is derived from the normal force model by considering the time spent in the unloading period during a collision. The detailed derivation is given by Y. Lan in his dissertation [66]. Thus,

$$\Delta t = \frac{\pi e \sqrt{\dfrac{m}{2K_1}}}{n} = \frac{\pi e \sqrt{\dfrac{\pi d^3 \cdot \rho}{12K_1}}}{n} \tag{4.8}$$

where e is the restitution coefficient, m is mass of particle, K_1 is spring stiffness for loading, n is the desired (user-input) number of time steps for one contact (usually $n \sim 40$), d is the diameter of sphere and ρ is the density of the material. Equation (4.8) shows

that time step depends on the material properties e, d, ρ, K_1. In particular, it is clear that K_1 has close relationship with Δt. If the K_1 is very large, the time step will be very small and computation time will be very long. However, if K_1 is very small, the particle will be too soft, and thus the deformation or overlap can be greater than one to two percent of the particle diameter, which is what occurs during the collision of real particles. The Hertzian model can be used to estimate the value of the stiffness K_1 of the loading spring [66], i.e.

$$\alpha_{max} = \left[\frac{15m\upsilon_{max}^2 \cdot \left(1-\nu^2\right)}{4 \cdot E\sqrt{d}} \right]^{\frac{2}{5}} \tag{4.9}$$

$$K_1 = m \cdot \left(\frac{\upsilon_{max}}{\alpha_{max}} \right)^2 \tag{4.10}$$

where α_{max}, υ_{max} are the maximum overlap and impact velocity respectively between two spheres during collision. In these expressions, ν is the Poison's ratio, and E is Young's modulus of the material.

By substituting Equation (4.9) into Equation (4.10), one finds that

$$K_1 = \left[\frac{4E\sqrt{d \cdot \upsilon_{max}}}{15m \cdot \left(1-\nu^2\right)} \right]^{\frac{4}{5}} \tag{4.11}$$

In the study, the value of K_1 approximated from Equation (4.11) is generally between 100,000 and 20,000,000 N/m^2 depending on different material properties used.

4.5 Boundary Conditions

Experiments and theoretical studies have shown that boundary conditions greatly influence the behaviors of particle beds [44, 66]. In this investigation, both the bottom and sidewalls are chosen to be solid. The top surface is open and vibrations are supplied from the floor (Figure 4.2).

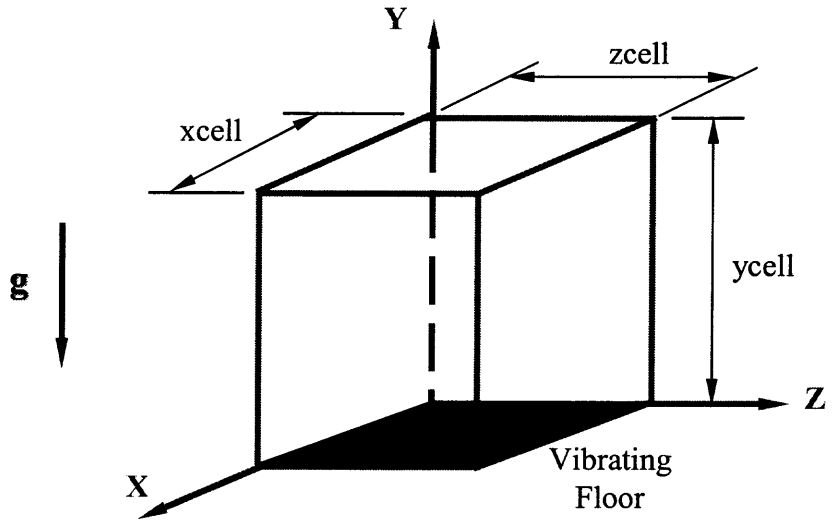

Figure 4.2 Computational cells and boundary conditions.

The solid plane is modeled as a rigid sphere whose motion is unaffected by collisions with the flow particles. The velocity of the floor $\upsilon(y)$ is given by

$$\upsilon(y(t)) = vamp \cdot \cos(2\pi \cdot f \cdot t) \tag{4.12}$$

where $vamp = 2\pi f * a$, and f and a are the vibration frequency (Hz) and amplitude (m).

4.6 Diagnostics and Data Analysis

The main thrust of this investigation is the densification process induced through vibrations. In both the physical experiments and computer simulations, three procedures take place (pouring, vibrating, and relaxing) that correspond to the states depicted in Figure 4.3. The poured state is that obtained immediately after the particles have been deposited and have come to rest in the vessel. The dynamic state refers to the condition of the system while under vibration and in a steady state condition. Finally, the relaxed state is what results after the external vibrations are terminated.

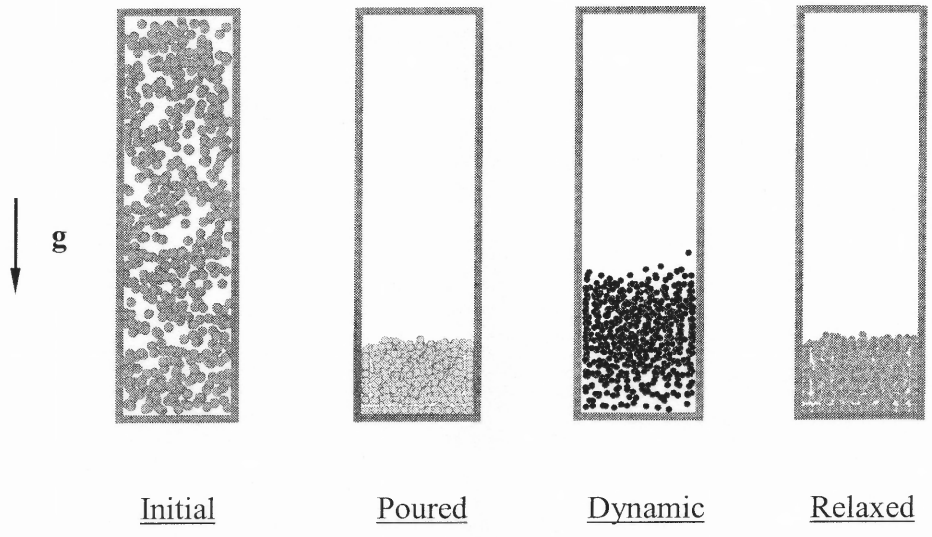

Figure 4.3 States corresponding to pouring, vibration and relaxation.

In order to describe or characterize these states, four quantities are computed, namely, the solids fraction, improvement in solids fraction, granular temperature and translational energy ratio.

4.6.1 Solids Fraction

Two spatial averaging methods are employed to compute the solids fraction. The bulk solids fraction represents the mean value for the entire computational cell, while the local

average provides information on the depth profile of the solids fraction. In order to calculate local average solids fraction, the computational cell is partitioned into "zones" or layers along its depth. The depth of each zone is generally equal to the diameter of the sphere so t hat a particle may occupy up to two layers. An instantaneous zone diagnostic is computed as a mass-weight average of all particles that occupy a zone at some time *t*.

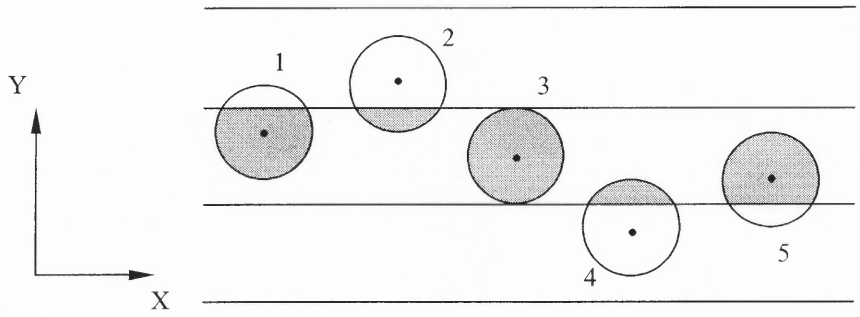

Figure 4.4 Only shadow portions of particles contribute to the average.

In Figure 4.4, only the mass contained in the lower parts of particles *1* and *2*, total mass of particle *3* and the upper parts of particles *4* and *5* are included when the average for zone *y* is calculated. So the instantaneous solids fraction of the layer at time *t* is given by,

$$SF(y,t) = \frac{\sum_{i \in y} Vol_i(y,t)}{Vol(y)} \tag{4.13}$$

4.6.2 Improvement in Solids Fraction

The poured state of the system can be affected by a number of factors, such as deposition intensity, size of the vessel relative to the particle size, particle shape and material properties. The question thus arises as to how one can compare the relaxed states of

systems that have different initial or poured configurations. This can be done by computing the *improvement* in solids fraction as a relative difference in solids fraction, i.e.

$$ISF = \left(\frac{\rho_{relaxed}}{\rho_{poured}} - 1 \right) \times 100 \tag{4.14}$$

If $ISF < 0$, the bulk solids fraction after vibrations are terminated is the same as it was after particles were poured into the vessel.

4.6.3 Granular Temperature T_d

In analogy to the definition of temperature in thermodynamics, the granular temperature T described the kinetic energy of the granular mass due to fluctuating velocities. It is commonly defined by,

$$\frac{3}{2} \cdot T = \frac{1}{2} C(y,t)^2 \tag{4.15}$$

where $C(y,t)$ is the root-mean-square (rms) deviatoric velocity, whose y-zone mass-weighted average at time t is calculated as,

$$C(y,t) = \left(\frac{\sum_{i \in y} \hat{m}_i(t)(\upsilon_i(t) - u(y,t))^2}{\sum_{i \in y} \hat{m}_i(t)} \right)^{1/2} \tag{4.16}$$

Here, $\hat{m}_i(t)$ is the mass fraction of particle i in zone y, $\upsilon(y,t)$ is the velocity of particle i at time t. The quantity $u(y,t)$ is the instantaneous mean velocity in zone y, and computed as,

$$u(y,t) = \frac{\sum_{i \in y} \hat{m}_i(t) \cdot \upsilon_i(t)}{\sum_{i \in y} \hat{m}_i(t)} \tag{4.17}$$

Granular temperature is made non-dimensional by dividing it by the product "*gd*", so that T_d is computed as,

$$T_d = \sqrt{\frac{T}{gd}} \tag{4.18}$$

where g is the gravitational acceleration and d is the diameter of a particle.

4.6.4 Translational Energy Ratio *R*

Momentum is supplied to the flow particles through inelastic collisions with the floor, and thus the entire system is activated. How the energy supplied by the moving floor is partitioned into the bed particle influences the "phase" of the system. The translational energy ratio R is defined as a ratio of kinetic energies. If it refers to the kinetic energy of the vertical motion to the lateral motion, then R is computed as,

$$R \equiv E_y(y,t)/E_x(y,t) = \frac{\sum_{i\in y} \hat{m}_i(t) * (v_{iy}(t))^2}{\sum_{i\in y} \hat{m}_i(t) * (v_{ix}(t))^2} \tag{4.19}$$

A large value of R as defined by equation (4.19) indicates on the average, that particle bed's motion is primarily in the vertical direction. Note that because there is no effective difference in the behavior of the particle assembly in the x and z directions, it is sufficient to compute only the energy ratio defined by (4.19). In Section 6.1 (Chapter 6), a categorization of the system's "local phase" as either "solid", "thermal" or "thermal-solid" is described in terms of the R values. It is important to mention that R only partially describes the partition of energy supplied by the floor since particles also rotate.

CHAPTER 5

POURING PROCESS OF UNIFORM-SPHERE BEDS WITH SOLID SIDEWALLS

In this chapter, a detailed parameter study of the process by which a "poured" state is obtained is presented. Because of the control on particle properties afforded by the simulation, it is possible to obtain some clear insights.

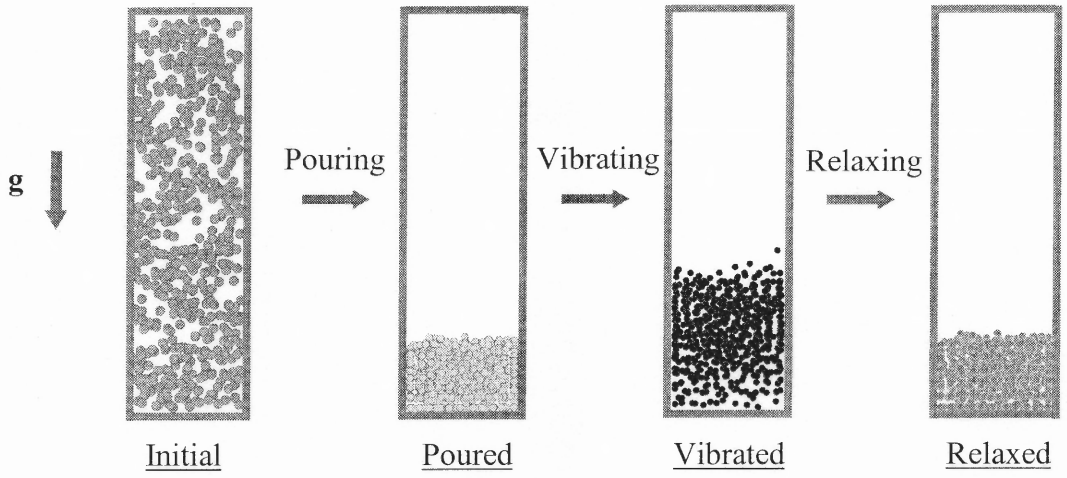

Figure 5.1 Three steps and four states in vibration simulation.

The four steps in an individual vibration experiment are shown in Figure 5.1, which depicts four states and three processing steps.

- Pouring process to attain a stable state (poured)
- Vibration for a period of time to obtain a dynamic state (dynamic)
- Relaxation to attain another stable state (relaxed)

The initial state (defined by the particle positions) is determined in the code via a random number generator that distributes particles uniformly within the computational cell so that solids fraction is homogeneous along the three coordinate directions.

For the pouring process of mono-disperse spheres, the following aspects are considered:

1) Effect of initial positions of particles
2) Effect of material properties
   - Particle friction μ
   - Restitution coefficient e
   - Normal stiffness K_1
   - Material Density v
3) Effect of aspect ratio d/L of container
4) Effect of wall friction μ_w
5) Effect of different pouring methods
6) Effect of size of particle system N
7) Comparison with experimental results of other researches

In order to compare with some experiment results using very soft spheres, such as lead, a normal force model with variable restitution coefficients has been used in Section 5.8. The physical reason for the non-constant restitution coefficient in this case is based on the fact that e is known [Goldsmith, etc.] to be a monotonically decreasing function of normal relative impact velocity beyond a value that depends on the particle material properties.

In the simulation, the material properties for acrylic spheres of diameter d = 1/4" are chosen. All other parameters are kept constant, except for the particle friction coefficient. The operating parameters are listed in Table 5.1.

Table 5.1 Simulation Operating Parameters

Number of Particles N	605
Diameter of Particles (m)	0.00635
Density of Particles (kg/m^3)	1200
Normal Stiffness of Particles (N/m^2)	2.8×10^6
Particle Friction Coefficient μ_p	0.01 to 0.8
Wall Friction Coefficient μ_w	0.01 – 0.8
Cell Dimension ($L*W*H$) in meter	$0.06 \times 0.06 \times 0.2$
Coefficient of Restitution (e)	0.9

5.1 Effect of Initial Positions of Particles

In the physical pouring experiment (see Chapter 2), 20 trials were completed for each sphere diameter that was used. It was found there that the small fluctuations in the poured solids fraction decreased with the aspect ratio (L/d) (see Figure 2.3). The simulation is carried out to duplicate the same phenomena through the use of a random number function capable of generating different sequences of numbers depending on the *seed* that is used. For a specific aspect ratio, the code has been re-run 10 times, corresponding to 10 different sequences of random numbers to generate ten pre-poured (before gravity is activated) systems. Upon completion of the pouring process, the mean solids fraction and its fluctuation was calculated. This procedure was done for 4 different aspect ratios with the data plotted in Figure 5.2.

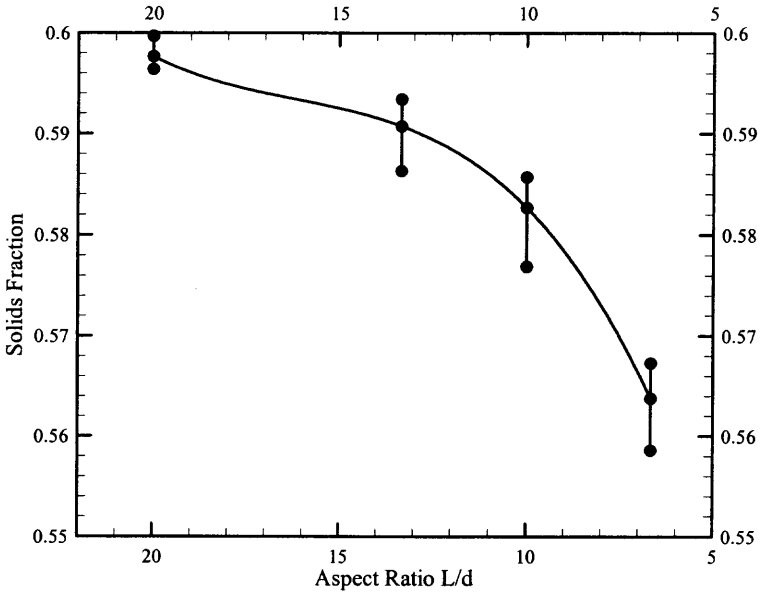

Figure 5.2 Effect of initial positions of particles on poured solids fraction, $N = 605$, $\mu_p = 0.1$, $\mu_w = 0.3$.

From the Figure, it is clear that with the increase of aspect ratio (L/d), the average poured solids fraction increases, and its fluctuation decreases – a trend that is in good agreement with the results of the physical experiments (Figure 2.3).

5.2 Effects of Material Properties

As mentioned in Chapter 1, researchers used different materials to carry out experiments, and it is known that different materials have different material properties. In this section, an exploration of the influence of particle properties (friction coefficient, normal restitution coefficient, loading stiffness and material density) on poured bulk density is carried out. A description of the simulation case studies for each property follows.

5.2.1 Effect of Particle Friction Coefficient μ_p

Figure 5.3 summarizes the results of the simulations in which particle friction coefficient was varied, from perfectly smooth ($\mu = 0$) to very rough ($\mu = 0.8$), while the wall friction coefficient (μ_w) was fixed at 0.30. As the trend in the figure indicates, particles that are more frictional produce a less dense poured structure. The reason for this behavior is that a high particle friction coefficient promotes the formation of large voids in the packing. When the friction is smaller, the probability of the formation of arches between particles becomes smaller, which results in a smaller void volume.

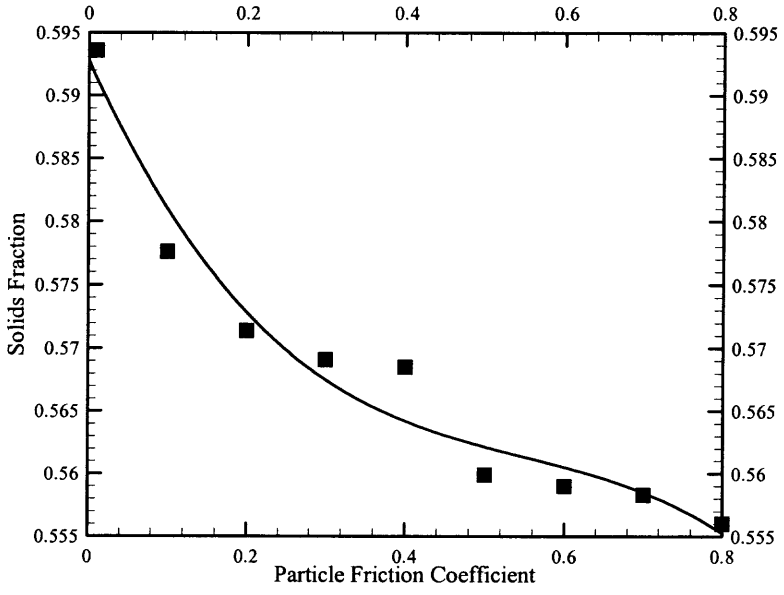

Figure 5.3 Relationship between poured solids fraction and friction coefficient for $N = 605$, $\mu_w = 0.3$.

5.2.2 Effect of Restitution Coefficient *e*

For the height of the computational cell used in this study, very little effect of restitution coefficient on bulk solids fraction was found, as can be seen in Figure 5.4.

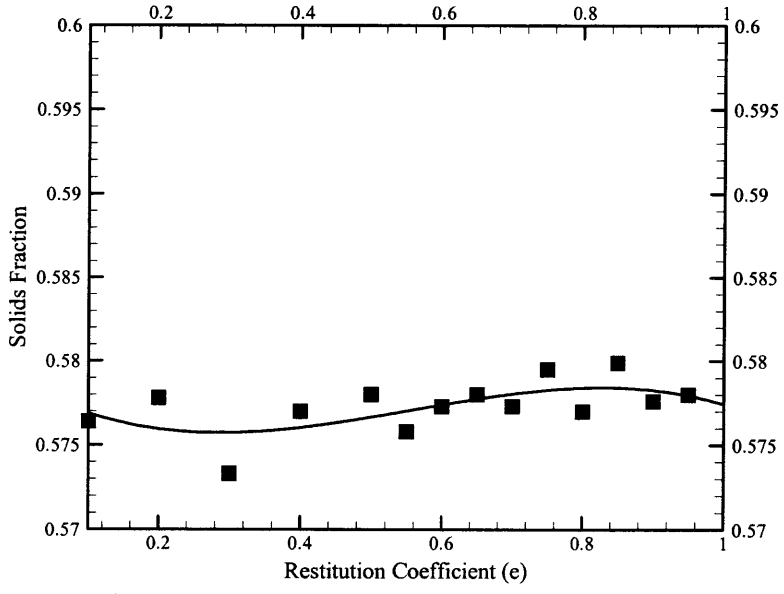

Figure 5.4 Effect of restitution coefficient on poured solids fraction, $N = 605$, $\mu_p = 0.1$, $\mu_w = 0.3$.

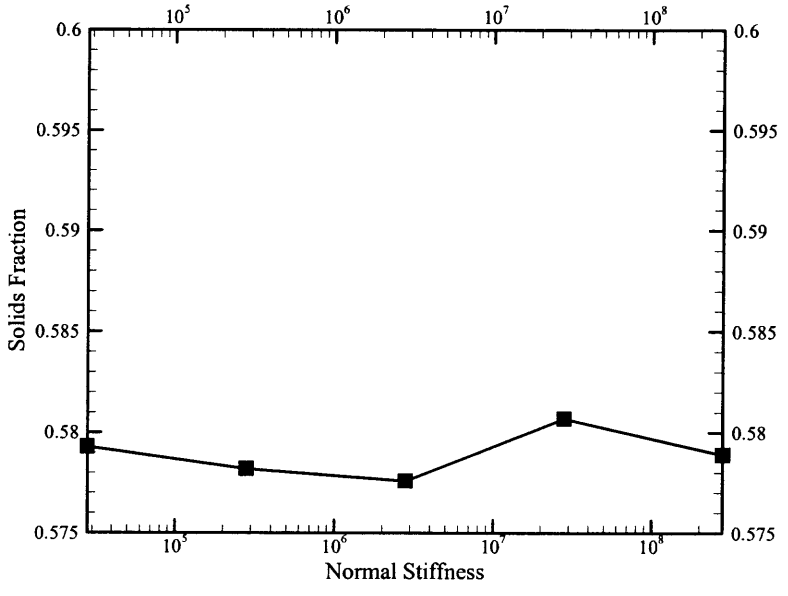

Figure 5.5 Effect of normal stiffness on poured solids fraction, $N = 605$, $\mu_p = 0.1$, $\mu_w = 0.3$.

5.2.3 Effect of Normal Stiffness K_1

The loading stiffness K_1 of the particles was changed over a range of four orders of magnitude. Figure 5.5 indicates that the mean solids fraction remained relatively constant.

5.2.4 Effect of Material Density

From the Figure 5.6, it is noted that the poured solids fraction increases slightly with the material density, albeit it is very small (less than 1%) for the height of the computational cell.

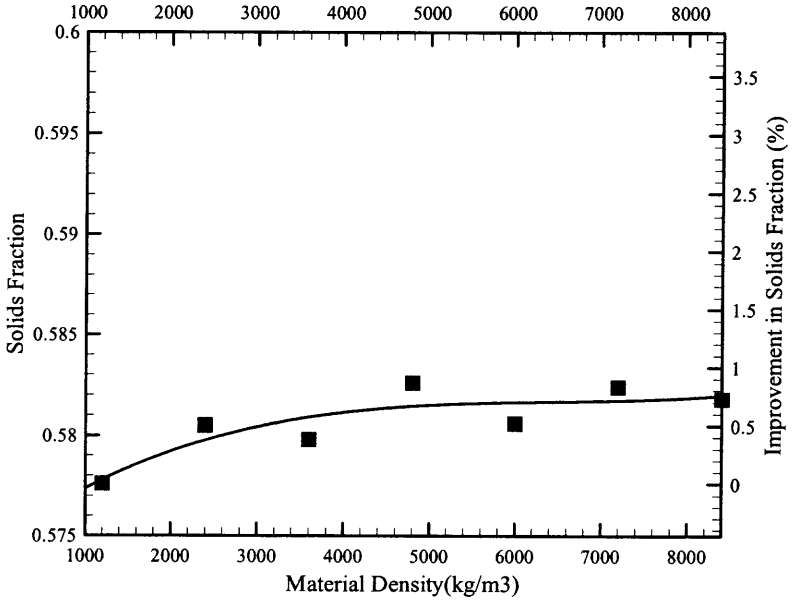

Figure 5.6 Effect of material density on poured solids fraction, $N = 605$, $\mu_p = 0.1$, $\mu_w = 0.3$.

From the above simulations, it is very clear that material density, normal stiffness and restitution coefficient have only a minimal influence on the poured solids fraction. However, particle friction appears to be the most important factor to affect the poured bulk density.

5.3 Effect of Aspect Ratio of Container *L/d*

In order to produce a variety of aspect ratios *L/d*, the dimensions of the computational cell in the *x* and *z* directions was varied uniformly (see Figure 5.7) while the particle diameter *d* and cell height (*ycell*) was kept constant. The initial solids fraction distribution along the cell height was maintained by changing the number of particles used.

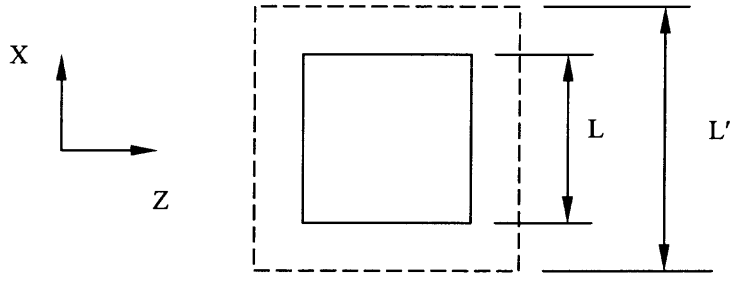

Figure 5.7 Section areas of the computational cell.

Figure 5.8a indicates the poured solids fraction is quite sensitive to the aspect ratio, i.e., it increases with the dimensions of the base of the computational cell. So as the cell becomes wider, the influence of the walls in arranging the particles to form greater voidage begins to disappear. The trend of the data in Figure 5.8a is in good agreement with that obtained in the physical experiments and shown in Figure 2.3. It is possible to extrapolate the simulated curve to the limit of a container of infinite width (or base dimensions) $d/L \rightarrow 0$, thereby finding what is often references as the "random loose" packing density. The linear extrapolation, shown in Figure 5.8b, yields a value of 0.61, which is in good agreement with the results of Scott [7] and Bennett [33].

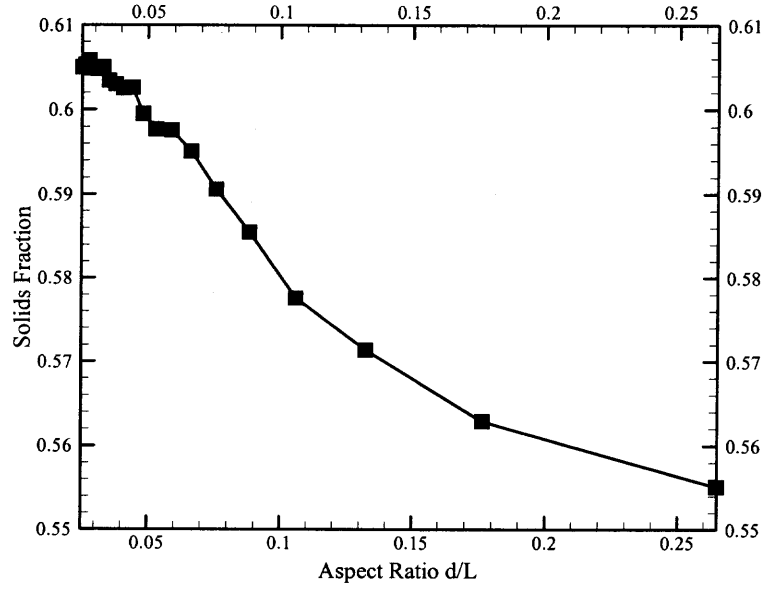

Figure 5.8a Relation between poured solids fraction & aspect ratio.

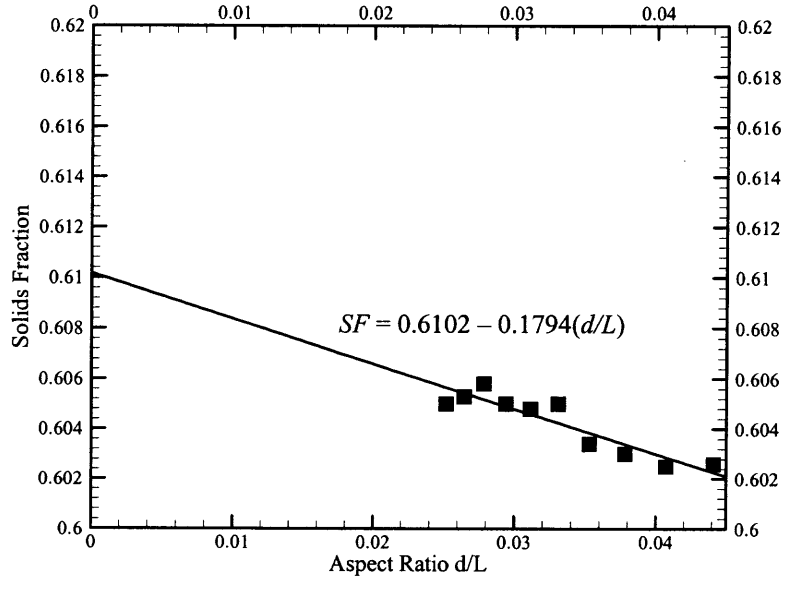

Figure 5.8b Solids fraction of random "loose" packing obtained via a linear extrapolation of the simulation data.

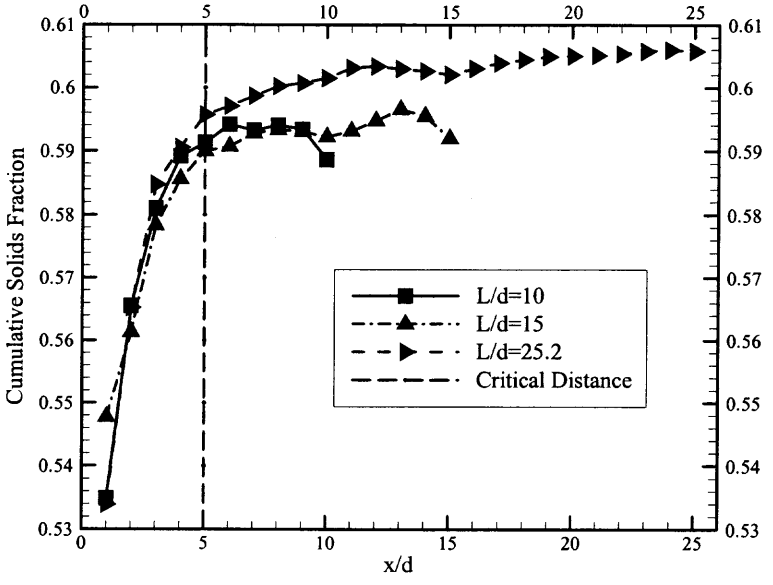

Figure 5.9 Cumulative solids fraction in the wide direction.

From the Figure 5.9, the width profiles of cumulative solids fraction indicate the effect of side walls on the overall solids fraction.

Table 5.2 Cumulative Solids Fraction and Ratios

	L/d=10	*L/d*=15	*L/d*=25
Solids Fraction at *3d*	0.581626	0.578329	0.584788
Solids Fraction at *4d*	0.589173	0.58561	0.590585
Solids Fraction at *5d*	0.591289	0.59	0.59573
Max. Solids Fraction	0.594169	0.596562	0.605987
$\rho_{3d}/\rho_{max.}$	97.9%	96.9%	96.5%
$\rho_{4d}/\rho_{max.}$	99.2%	98.2%	97.5%
$\rho_{5d}/\rho_{max.}$	99.5%	99%	98.3%

Table 5.2 shows the cumulative solids fraction and the ratios at three *L/d* values. If it is assumed that the wall no longer influences the results from the solids fraction ratio reaches 98%, the table shows that this occurs at approximately 5 particle diameters from the wall. This result is in agreement with the literature [67].

5.4 Effect of Wall Friction Coefficient μ_w

To study the effect of wall friction, its value is changed from 0.01 to 0.8 while keeping all other parameters constant. As expected, Figure 5.10 shows that the wall friction has little effect on the poured solids fraction. In this simulation, the aspect ratio *L/d* was approximately 10.0.

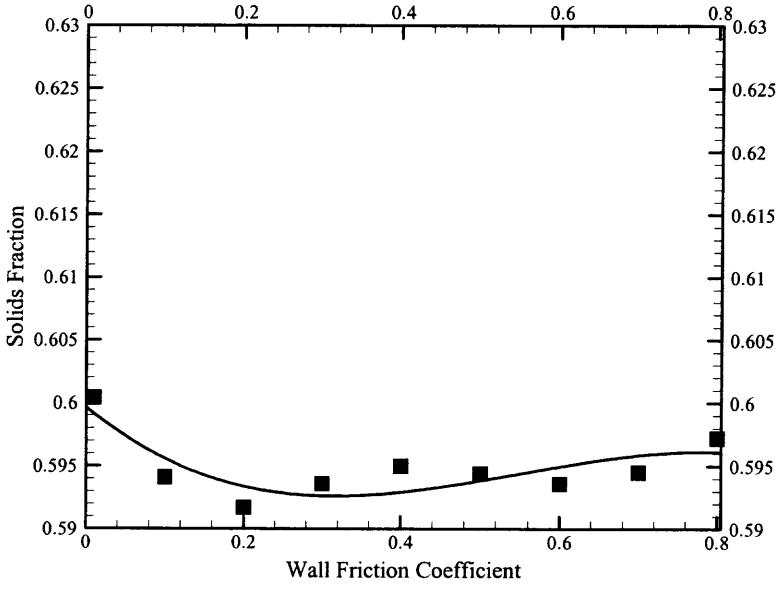

Figure 5.10 Effect of wall friction on poured solids fraction, $N = 605$, $\mu_p = 0.1$.

5.5 Effect of Different Pouring Methods

In order to examine the effect of different pouring methods, the number of particles (N = 605) is fixed, while the y coordinates of all particles are changed by uniformly increasing their values by a fixed distance $\boldsymbol{P}$ (called the "pouring height", as in Figure 5.11). Then, the system is allowed to collapse under the action of gravity.

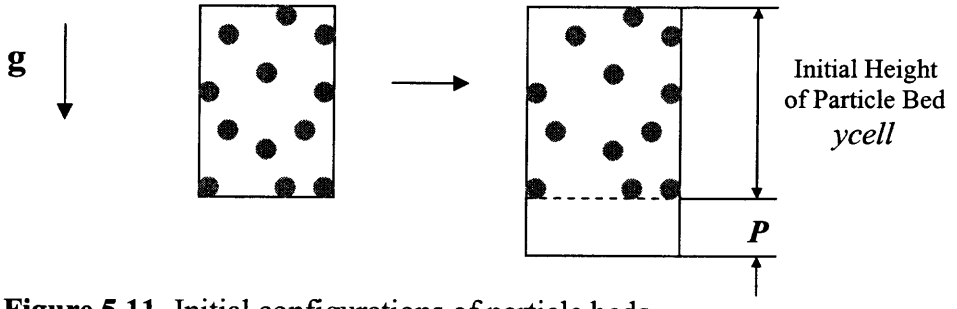

Figure 5.11 Initial configurations of particle beds.

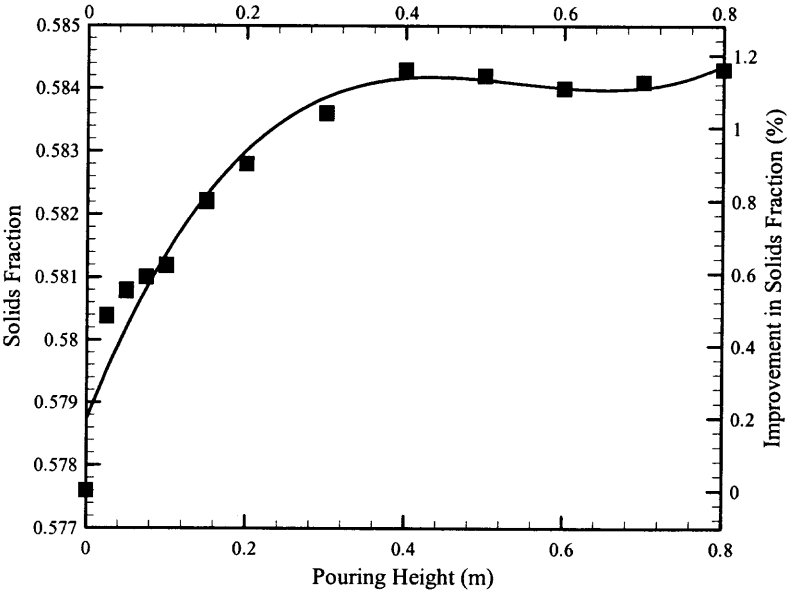

Figure 5.12 Effect of pouring height on poured solids fraction, N = 605, μ_p = 0.1, μ_w = 0.3.

The results of this procedure summarized in Figure 5.12 indicate only a very small increase in solids fraction. In order to assess if the height at which the pouring takes place is important, the value of *ycell* of particle bed is varied up to one meter.

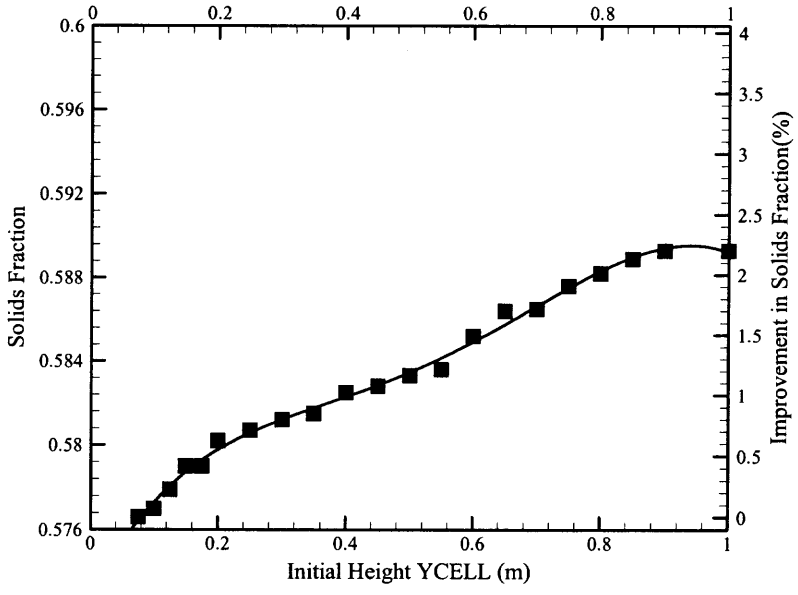

Figure 5.13 Effect of initial height on poured solids fraction, $N = 605$, $\mu_p = 0.1$, $\mu_w = 0.3$.

The result in Figure 5.13 again shows only a small increase in solids fraction of not more than 2.5%. While the trend is qualitatively similar to the physical experiments of Macrae et al. [30], the quantitative values are smaller. They used several different materials, each of which showed that larger bulk densities were obtained as the height of the drop was increased. The quantitative difference between the simulation and experiment may be due to the fact that very different deposition methods were used. In the experiments, the material was poured in as a stream, in contrast to the simulation in which spheres are distributed throughout the computational cell volume before gravity was activated.

5.6 Effect of Size of System on Solids Fraction

Since all the results obtained up to this point are for a small system (only of N = 605 particles), larger systems are simulated. Here the initial height *ycell* is set to 0.2m, while the number of particles in the system is varied. This means that the initial solids fraction of the system was larger at N was increased.

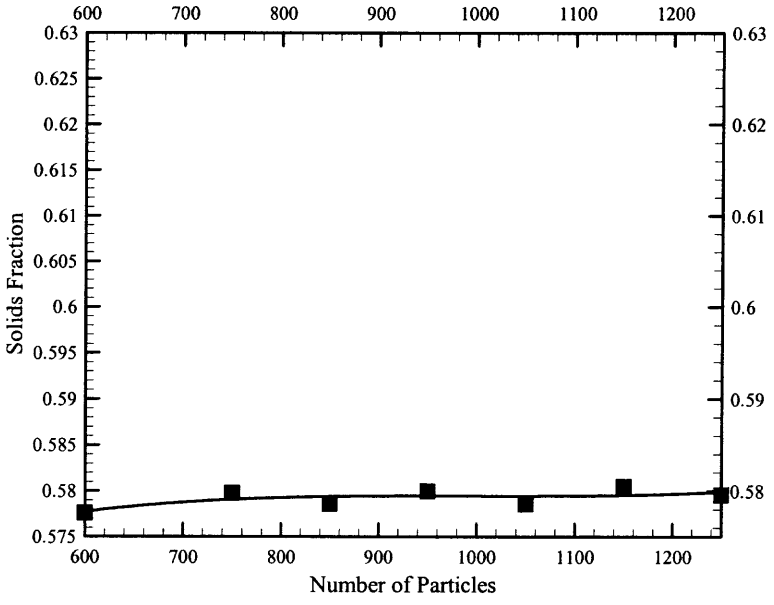

Figure 5.14 Effect of size of system with a constant *ycell*, $\mu_p = 0.1$, $\mu_w = 0.3$.

Figure 5.14 indicates that this procedure did not result in a drastic changed in bulk solids fraction over the ranged considered. The result is quite different if the initial solids fraction of the particle bed is fixed, while the number of particles in the system is changed (i.e., so that the particle beds have different initial heights *ycell*).

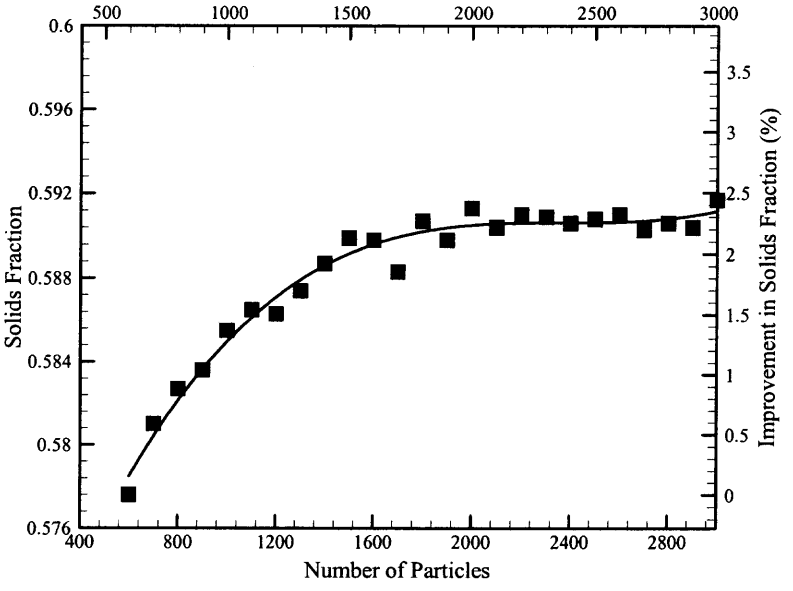

Figure 5.15 Effect of size of system with constant initial solids fraction, $N = 605$, $\mu_p = 0.1$, $\mu_w = 0.3$.

Figure 5.15 shows that as the number of particles N increases, the bulk density grows and then flattens out. The reason for the behavior in the figure can be explained in terms of the depth of the poured bed. For small system sizes, particles that rain down may disturb the already formed thin layer at the bottom of the cell so that voids are created thus reducing the mean solids fraction of the final, poured configuration. However, as the depth of the "stable" layer at the bottom develops for larger systems, the kinetic energy of particles falling from above onto this layer is quickly dissipated through the layer so that the effect on the voidage of the growing deposit is reduced. Beyond approximately 2000 particles, the process is stabilized and the bulk solids fraction flattens out.

5.7 Comparison with Experimental Results

In order to verify the correctness of the pouring simulation, a study is carried out with steel, glass and lead particles that can be compared with the experiments of Scott and Kilgour [7] and Macrae and Gray [30]. The size of spheres in the simulation is 1/4" (6.35 mm). The physical properties of the materials (i.e., density, Young's modulus and Poisson's ratio) are obtained from a handbook [68], while restitution coefficients are obtained from the experimental results of Goldsmith [55] and Marcre [30]. Since restitution coefficient for real materials is a decaying function of relative normal impact velocity, an average value was selected over the maximum expected value of impact velocity, which is approximated as

$$\upsilon_{\max} = \sqrt{2g \cdot Ycell} = \sqrt{2 \times 9.8 \times 0.2} \cong 2.0(m/s) \tag{5.1}$$

With this value of $\upsilon_{\max}$, equation (4.11) is used to compute the loading stiffness K_1 of the three materials. Additionally, in order to omit the effect of boundary, $L/d = 25.2$ is chosen. Table 5.3 lists the simulation parameters selected the steel, glass and lead particles.

Table 5.3 Main Simulation Operation Parameters for Three Materials

Materials	Steel	Glass	Lead
Material Density ρ (kg/m^3)	7900	2450	11340
Normal Stiffness K_1 (N/m^2)	1.5e+7	5.0e+6	2.0e+6
Restitution Coefficient e	0.9	0.8	0.4

Table 5.4 Comparison of Simulation with Experiments

Materials	Simulation	Experiments
Steel spheres	0.6034	0.596-0.608 [7, 30]
Glass spheres	0.6007	0.599-0.605[7, 30]
Lead spheres	0.5979	0.607 [30]

Table 5.4 shows that the simulated results fit within the range of experimentally obtained values for the steel and glass spheres. However, the agreement with the lead particles is not as good, with approximately a 1.5% discrepancy. The reason for this is that a constant restitution coefficient was used, which is not reasonable for lead spheres for the particle velocities in the simulation. In the next section, a velocity-dependent feature in the code is used for the lead spheres in an attempt to improve the result.

5.8 Modification of Normal Force Model

In this section, a variable coefficient of restitution mode is activated in the code for the soft lead spheres and the results are compared with the experiments of Goldsmith [55]. The derivation of the model developed by Walton and Braun is repeated here for completeness.

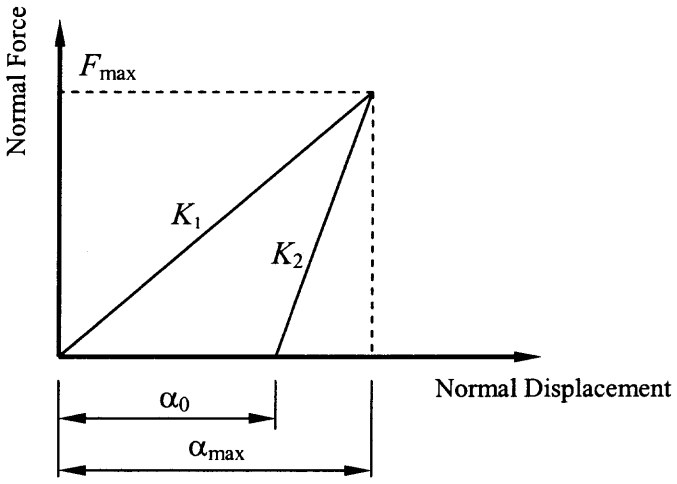

Figure 5.16 Normal force model.

The loading stiffness K_1 and unloading stiffness K_2 are linear functions of the maximum force F_{max} achieved before unloading (see Figure 5.16), so that,

$$F_{max} = K_1 * \alpha_{max} = K_2 * (\alpha_{max} - \alpha_0) \tag{5.2}$$

Equation (5.2) is rearranged to yield,

$$K_2 = \frac{K_1 * \alpha_{max}}{\alpha_{max} - \alpha_0} = K_1 + K_1 \cdot \frac{\alpha_0}{\alpha_{max} - \alpha_0} \tag{5.3}$$

$$K_2 = K_1 + K_1 \cdot \alpha_{max} \cdot \frac{\alpha_0}{\alpha_{max} \cdot (\alpha_{max} - \alpha_0)} = K_1 + F_{max} \cdot \frac{\alpha_0}{\alpha_{max} \cdot (\alpha_{max} - \alpha_0)} \tag{5.4}$$

By introducing a parameter S, defined as,

$$S = \frac{\alpha_0}{\alpha_{max} \cdot (\alpha_{max} - \alpha_0)} \tag{5.5}$$

a simple equation for the unloading stiffness is obtained, i.e.,

$$K_2 = K_1 + SF_{max} = SK_1\alpha_{max} \tag{5.6}$$

From the Equation (4.11)

$$\alpha_{max} = \sqrt{\frac{m}{K_1}} \cdot \upsilon_{max} \tag{5.7}$$

so that a substitution of equations (5.6) and (5.7) into (4.1), the yields,

$$e = \left(\frac{1}{1 + S \cdot \upsilon_{max} \cdot \sqrt{m/K_1}} \right)^{\frac{1}{2}} \tag{5.8}$$

The value of S is an input parameter in the simulation. Equations (5.5) and (5.7) indicate that S is not a constant because the relative normal impact velocities between colliding spheres is variable. Therefore, a value of S was selected to obtain the best match between the experimental data and simulated restitution coefficient.

A direct normal collision between two spheres at a selected impact velocity is simulated using a restitution coefficient taken from physical experiments in the literature [55]. With this data, equation (5.8) is solved to compute S for an input value. Then the impact velocity is changed, and the new restitution coefficient e is computed directly from the simulation using the previously determined value of S. The computed e is compared with data from Goldsmith [55] and procedure repeated to generate a curve of restitution coefficient against impact velocity.

The restitution coefficient as a function of impact velocity obtained from the simulation is compared with the data of Goldsmith in Figure 5.17. The lines are included in the figure to highlight the trends. The comparison is reasonable, although there is some deviation at higher impact velocities.

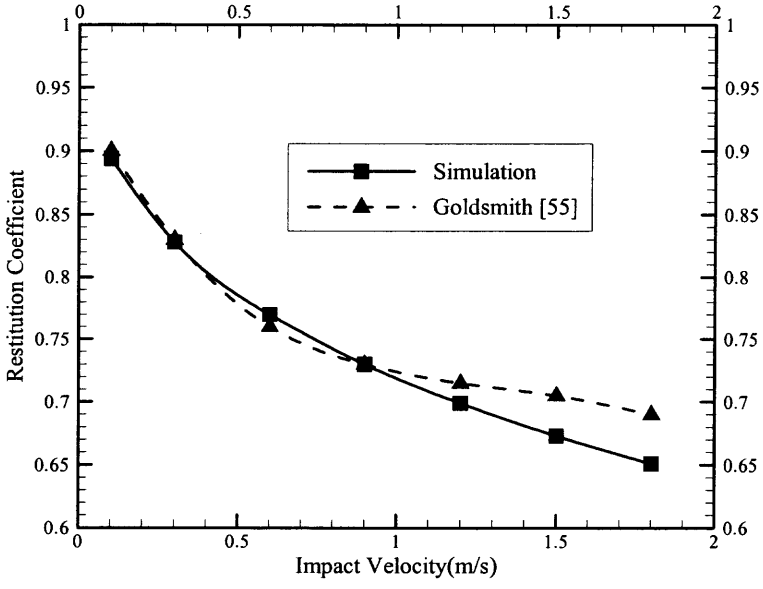

Figure 5.17 Relation between restitution coefficient and impact velocity for steel spheres.

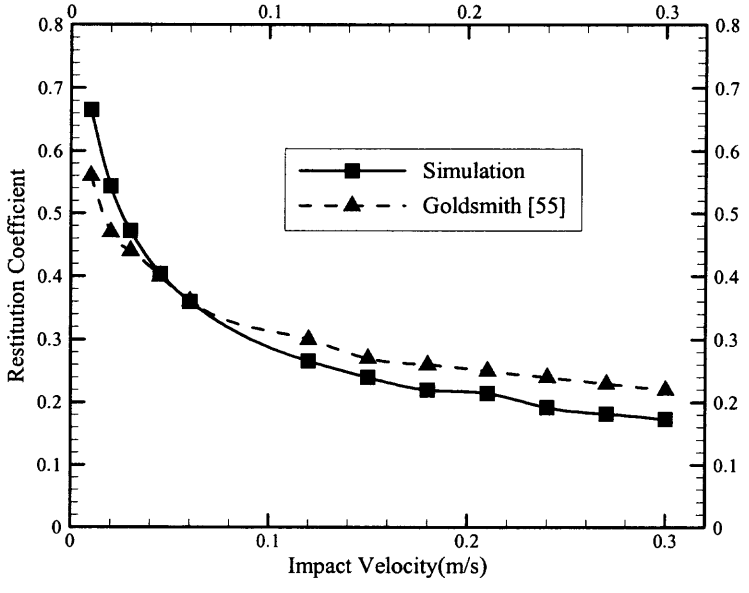

Figure 5.18 Relation between restitution coefficient and impact velocity (lead).

Figure 5.18 shows the results of the simulation as compared with the data for lead spheres. The intersection of the trend curves gives the value of the impact velocity and experimental restitution coefficient that was used to compute *S* from equation (5.8).

Although other strategies are possible to find an appropriate value of S, the technique employed here appears to have given good results.

Table 5.5 Results of Simulation and Physical Experiment of Lead Spheres

Methods	Random Loose Solids fraction
Simulation with constant *e*	0.5979
Simulation with variable *e*	0.6028
Physical experiment	0.607 [30]

A summary of the final results is presented in Table 5.5. This shows a marked improvement in the simulated random loose solids fraction when the variable restitution coefficient model is used. One final point should be emphasized here. Up to this point, only the overall or bulk solids fraction has been used to quantify the pouring process. If two pouring trials product almost the same solids fraction, this does not imply that the detailed microstructures are the same.

This fact is demonstrated in the following example. Two poured systems are generate using particles with e = 0.9 and 0.6. By partitioning the computational cell into layers, the depth profiles of the solids fraction can be computed. Figure 5.19 shows the results in which the bulk solids fractions are very close, and yet the depth profiles are different.

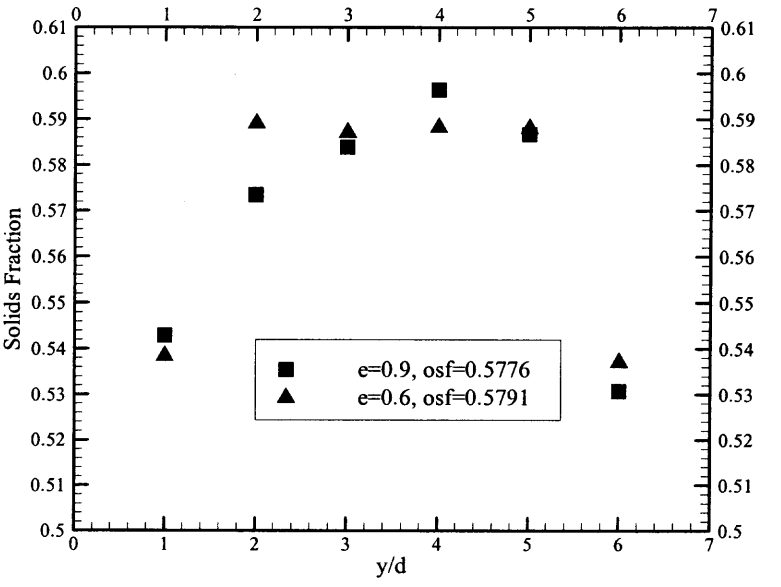

Figure 5.19 The depth profiles of solids fraction.

The results of the above study are summarized as follows.

1. With the increase of aspect ratio, the effect of initial positions of particles on the poured solids fraction disappears and the aspect ratio affects the poured solids fraction, the result from the simulation is very similar to that obtained from the physical experiments and conclusion in "Handbook of powder science" [67].
2. Particle friction coefficient has a pronounced influence on the poured solids fraction.
3. Other material properties, such as restitution coefficient, normal stiffness and material density appear to have only a small influence on the poured bulk solids fraction.
4. Wall friction has little effect on the poured solids fraction.
5. Particle beds with large *ycell* may yield slightly higher bulk densities.

6. By increasing system size while keeping the initial particle distribution along the depth constant, the poured solids fraction first increases and then flattens out.
7. The simulation produces almost the same random loose solids fraction as found in physical experiments in the literature [7, 30].
8. For soft particles, such as lead, a velocity dependent coefficient of restitution model in the code produced good agreement with the experiments of Goldsmith [55] and with the random loose experiments of Macrae [30].

CHAPTER 6

ANALYSIS OF INSTANTANEOUS DYNAMIC STATES

The final bulk density that a vibrated system achieves after the excitations are terminated should depend on the "dynamic" state – that is the condition that the system finds itself during vibrations. The focus of this chapter is on analyzing the dynamic state and its dependence on a number of parameters, i.e., vibration frequency and amplitude, particle friction coefficient μ, restitution coefficient e, container aspect ratio L/d, loading stiffness K_1 and initial solids fraction after pouring.

In order to quantify the dynamic state, depth profiles of solids fraction, granular temperature and translational energy ratio are computed as steady-state values. The data represents steady-state dynamic condition of the vibrated system. In a physical experiment, this would be tantamount to taking instantaneous measurements (if possible) when the bed of particles is being vibrated rather than when the shaking device is switched off.

The parameter that is used to classify the dynamic state (or phase) of the vibrated assembly is the translational energy ratio R in the following manner. The state is termed "thermal" if $R < 10$, "solid" if $R > 100$, and "thermal-solid" if $10 < R < 100$. Because the computed depth profiles of R are not constant, an energized system can exist in more than one state. The results of the study presented in this chapter suggest that there is complex relationship between the parameters, and that particle friction, restitution coefficient and initial poured states appear to have the greatest influence on the dynamic behavior of the system. Table 6.1 lists the parameter selected for the simulations.

Table 6.1 Operating Parameters for the Simulation

Particle Number N	605
Diameter of Particles d (m)	0.00635
Density of Particles (kg/m^3)	1200
Normal Stiffness of Particles (N/m^2)	2.8×10^6
Friction Coefficient of Particles μ_p	0.1
Wall Friction Coefficient μ_w	0.3
Cell Dimension (L*W*H) in meter	$0.06 \times 0.06 \times 0.2$
Coefficient of Restitution e	0.9
Vibration Amplitude a (inch)	0.005 - 0.12
Vibration Frequency (Hz)	5 - 100

6.1 Effect of Vibration Frequency and Amplitude

For this study, particles are assigned a restitution coefficient e of 0.9, a friction coefficient of 0.1 with wall friction set to 0.30. The selection of a shallow configuration (i.e., poured depth of approximately $7d$) and an aspect ratio L/d = 9.4 minimizes the system size (N = 605), so that greater computational efficiency is obtained.

At low acceleration levels, particles are constrained by near neighbors to move within only small neighborhoods of their initial locations, while, for higher accelerations, they can experience significant displacements. This is demonstrated by using two normalized amplitudes a/d and a range of frequencies that correspond to accelerations $\Gamma \equiv a(2\pi f)^2/g$ between 0.46 and 99.35. Each system was agitated for three seconds, starting from the same initial poured solids fraction ρ_o = 0.5775 (parameters μ_p = 0.3 and

$\mu_w = 0.1$, $e = 0.9$). Diagnostic quantities were computed at $t = 3$ seconds for both the high and low relative accelerations since little difference in the depth profiles of solids fraction and granular temperature was found beyond this point. In order to verify the simulation of vibration process, two vibration conditions (low vibration amplitude and high amplitude) are used. The results are then compared with the observations of Eversque et al. [14], the kinetic theory predictions of Richman & Martin [40] and the experimental conclusion of Thomas et al. [41].

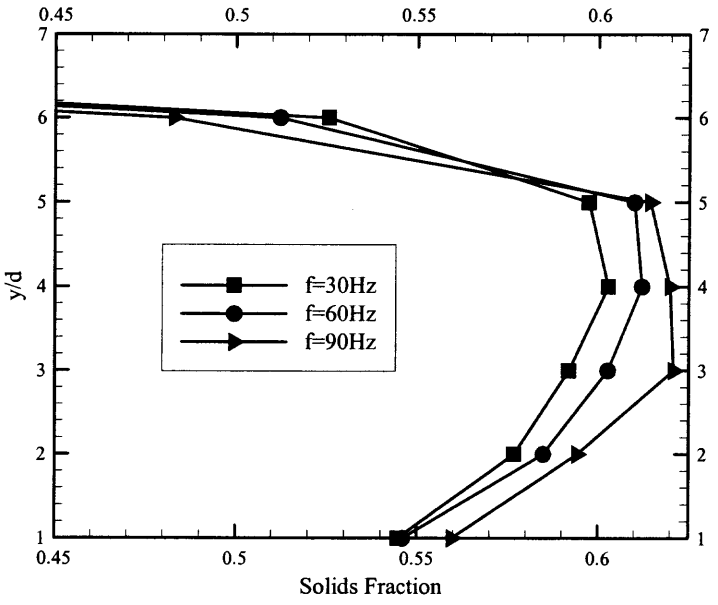

Figure 6.1 Depth profiles of solids fraction ($N = 605$, $a/d = 0.02$, $\mu_p = 0.3$, $\mu_w = 0.1$, $e = 0.9$) for $f = 30$, 60, 90 Hz and $\rho_o = 0.5775$.

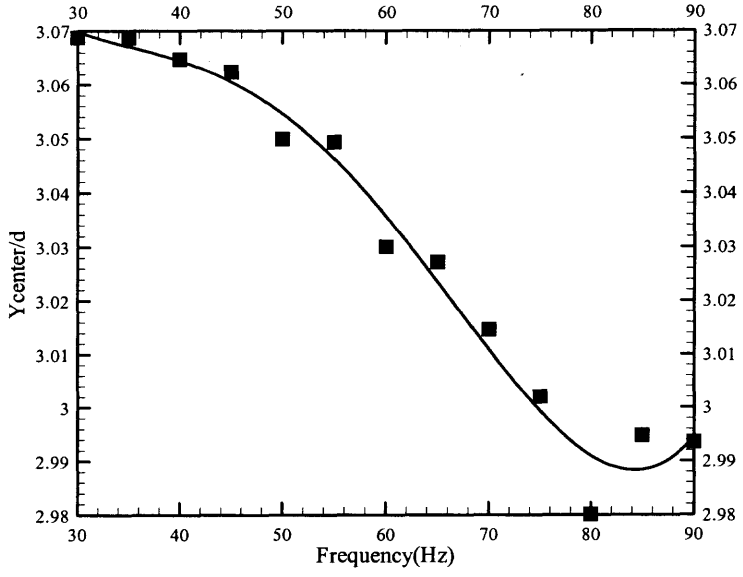

Figure 6.2 Mass center of the system ($N = 605$, $a/d = 0.02$, $\mu_p = 0.3$, $\mu_w = 0.1$, $e = 0.9$) as a function of vibration frequency.

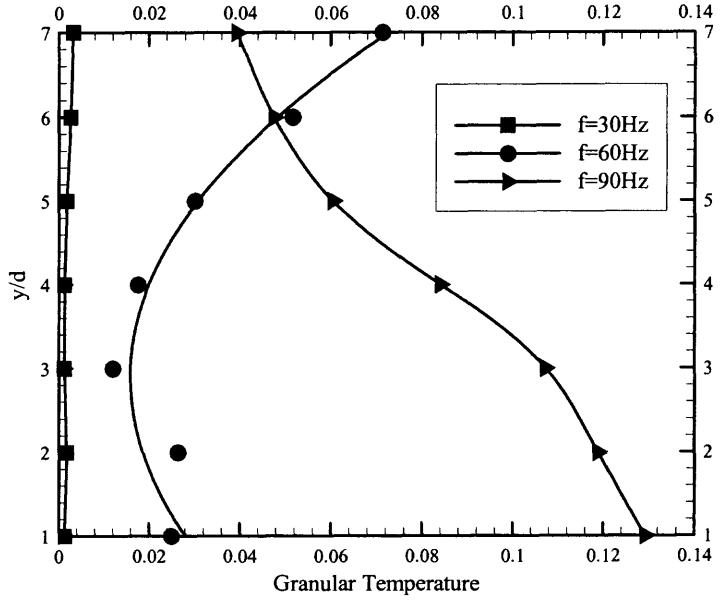

Figure 6.3 Granular temperature depth profiles ($N = 605$, $a/d = 0.02$, $\mu_p = 0.3$, $\mu_w = 0.1$, $e = 0.9$) for $f = 30$, 60 and 90 Hz.

The smaller amplitude vibrations produce minimal agitation in the system (relative to when a/d = 0.48), which is reflected in the scales selected to display the granular temperature profiles in Figure 6.3 and Figure 6.8. The solids fraction depth profiles in Figure 6.1 at a/d = 0.02 and ρ_o = 0.5775 illustrates that the bed depth does not change appreciably when f = 30, 60 and 90 Hz (Γ = 0.46, 1.84 and 4.14). However, as f grows, the solids fraction does increase as the bulk mass shifts towards the floor (Figure 6.2). At 30 and 60 Hz, the granular temperature (Figure 6.3) at the surface of the bed is largest, while at 90 Hz it is the smallest so that particles nearest the vibrating floor experience greater agitation.

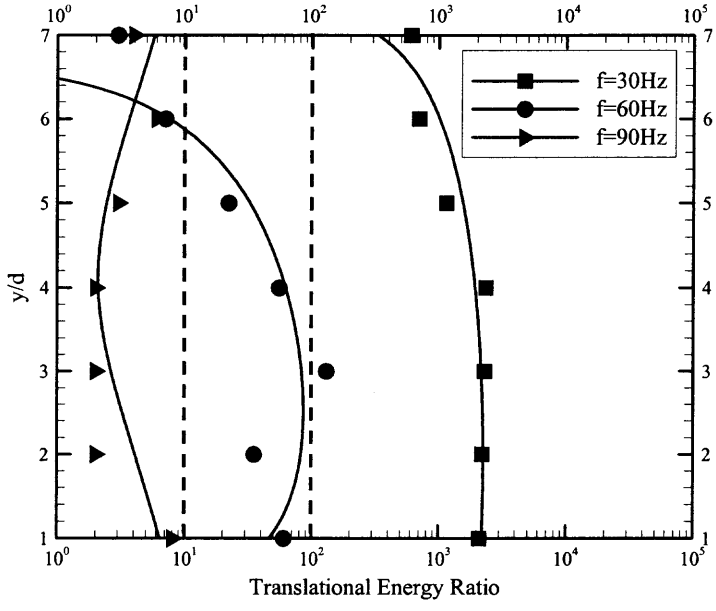

Figure 6.4 Depth profiles of the translational energy ratio R (N = 605, a/d = 0.02, μ_p = 0.3, μ_w = 0.1, e = 0.9) for f = 30, 60, 90Hz.

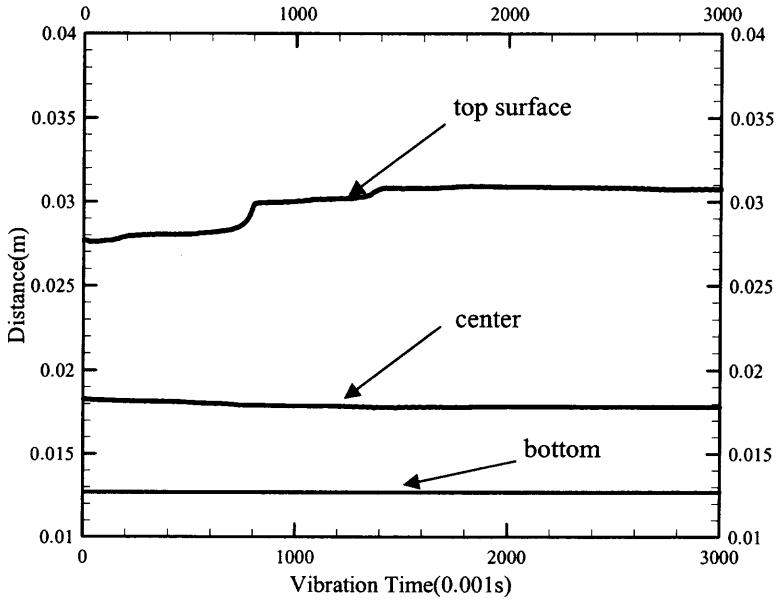

Figure 6.5 Evolution of distances between two particles at bottom and center regions, and near the surface ($N = 605$, $a/d = 0.02$, $f = 30$Hz, $\mu_p = 0.3$, $\mu_w = 0.1$, $e = 0.3$).

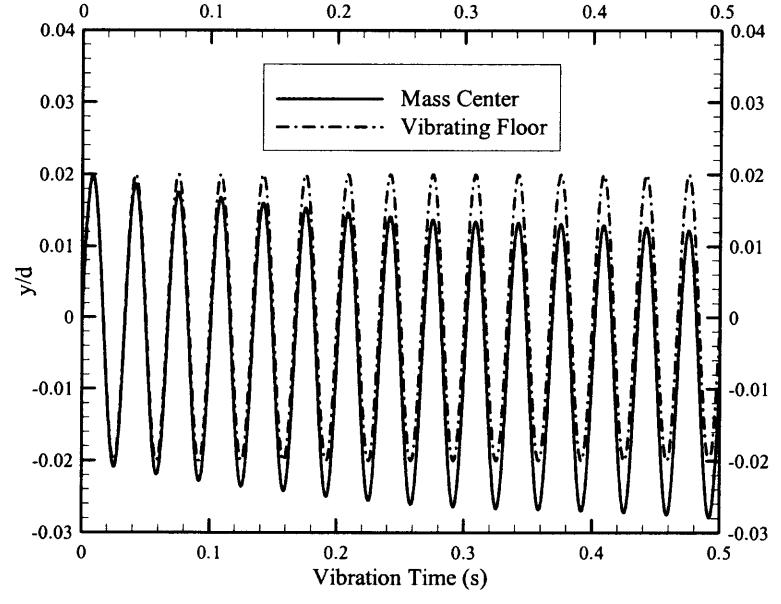

Figure 6.6 Trajectory of the mass center (solid line) and the floor (dashed line) ($N = 605$, $a/d = 0.02$, $f = 30$Hz, $\mu_p = 0.3$, $\mu_w = 0.1$, $e = 0.9$).

The depth profile of the translational energy ratio R and plotted in Figure 6.4 on a log scale features a small gradient with a minimum near the surface. The vertical dotted lines indicate the demarcation between the solid, thermal and solid-thermal phases. At f = 30 Hz, the values of R, which are significantly larger than at the other two frequencies, suggests that the motion of the particles is predominantly in the y-direction. For these vibration conditions, particles do not wander or migrate from their pre-vibrated locations, as substantiated by the evolution of the distance between two arbitrarily chosen particles in three different regions of the bed (Figure 6.5). Furthermore, an inspection of several animation frames revealed that particles moved in a coordinated mode, i.e., in this case up and down together. Indeed, the motion of the mass center is in phase with the vibrating floor at this frequency as revealed in Figure 6.6. Hence, the system is in a "solid" phase.

At f = 60 Hz, there is a very large difference between the value of R at the bottom and the surface of approximately two orders of magnitude. More importantly, R at the surface is relatively small (approximately 5) and therefore, particle velocities (proportional to $\sqrt{R}$) in the x and y directions are comparable. Hence, the thermal phase appears at the surface (in agreement with experiments [14]), and below this, the system is in a solid-thermal state. With an increase of frequency to 90 Hz, values of R are less than approximately 5, (except in the region adjacent to the floor where it is slightly higher) so that a significant fraction of the input kinetic energy has been coupled into the x-direction (also z-direction). This condition, in view of the granular temperature profile shown in Figure 6.4 at 90 Hz, suggests that the entire assembly is in a thermal state, although the bed depth remains constant.

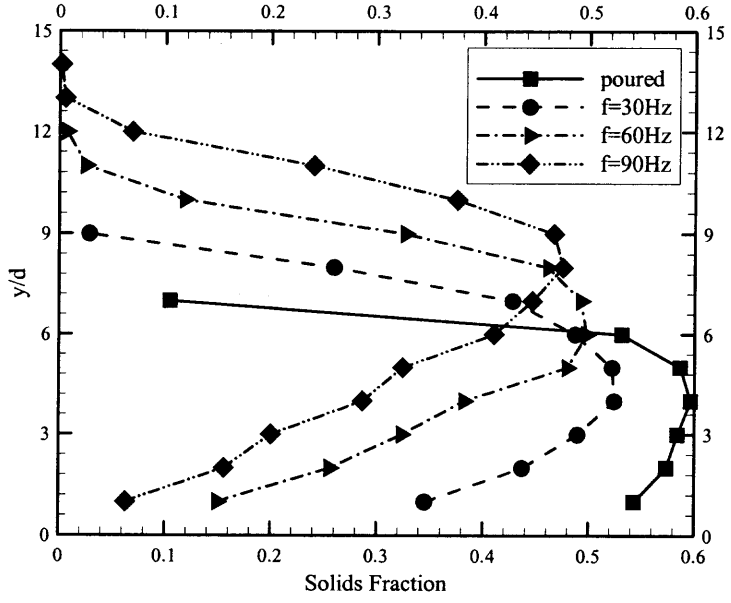

Figure 6.7 Solids fraction depth profiles ($N = 605$, $a/d = 0.48$, $\mu_p = 0.3$, $\mu_w = 0.1$, $e = 0.9$) for the poured state and $f = 30$, 60 and 90 Hz.

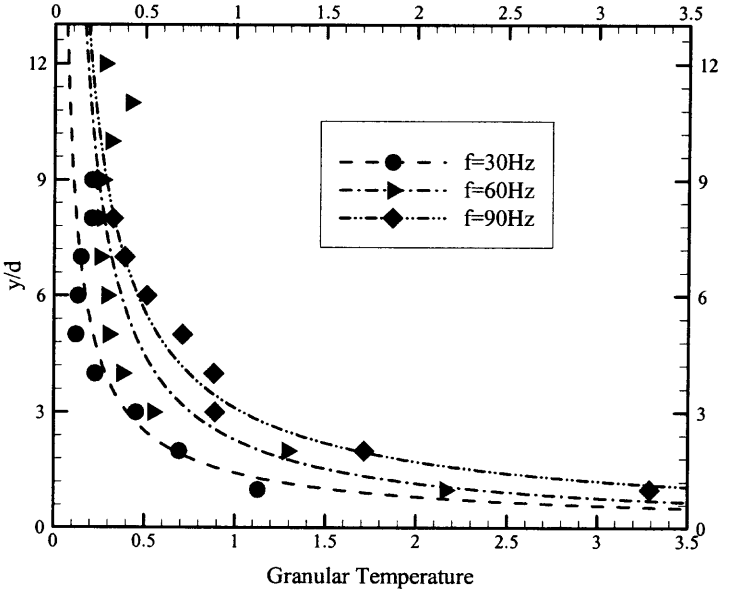

Figure 6.8 Depth profiles of granular temperature ($N = 605$, $a/d = 0.48$, $\mu_p = 0.3$, $\mu_w = 0.1$, $e = 0.9$) for $f = 30$, 60 and 90 Hz.

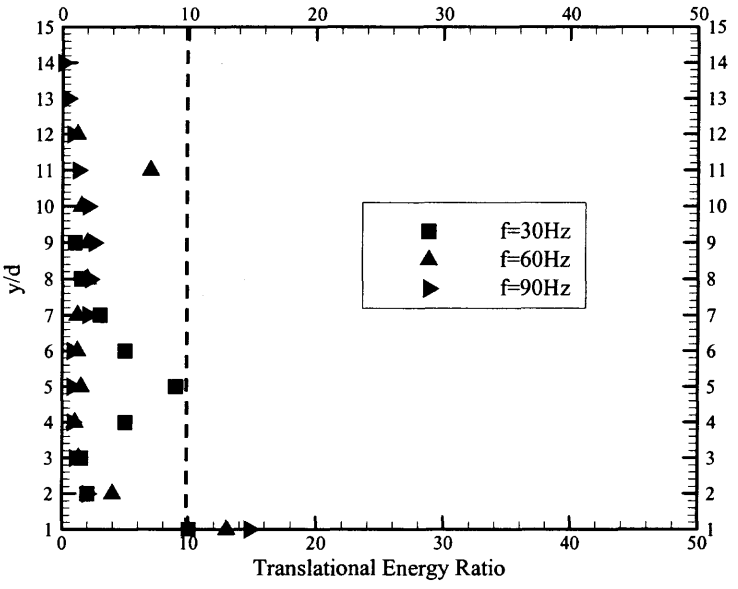

Figure 6.9 Depth profiles of translational energy ratio ($N = 605$, $a/d = 0.48$, $\mu_p = 0.3$, $\mu_w = 0.1$, $e = 0.9$) for $f = 30$, 60 and 90 Hz, the region to the left vertical dotted line delineates the solid phase.

When the floor displacement amplitude is increased to $a/d = 0.48$, the assembly experiences a drastic expansion of its depth as f increases (Figure 6.7), a phenomenon that has been reported in experiments [43]. There is an accompanying upward shift of the mass center and a depletion of particles near the floor. Here, large velocity fluctuations are reflected in a maximum granular temperature (Figure 6.8) that decreases towards the surface, in qualitative agreement with kinetic theory predictions [40]. Particles no longer remain close to their initial positions, but rather migrate. As indicated in the R profiles of Figure 6.9 (i.e., average values of R for each frequency were all less than 4.23), the increased displacement amplitude of the floor causes a shift to the thermal phase, albeit the system possesses a fluid-like nature.

6.2 Effect of Depth of Particle Bed

The depth of the poured bed was approximately doubled to 14*d* by increasing the number of particles (N = 1305) while maintaining the aspect ratio L/d = 9.4 and all other parameters identical to the system discussed in the previous section.

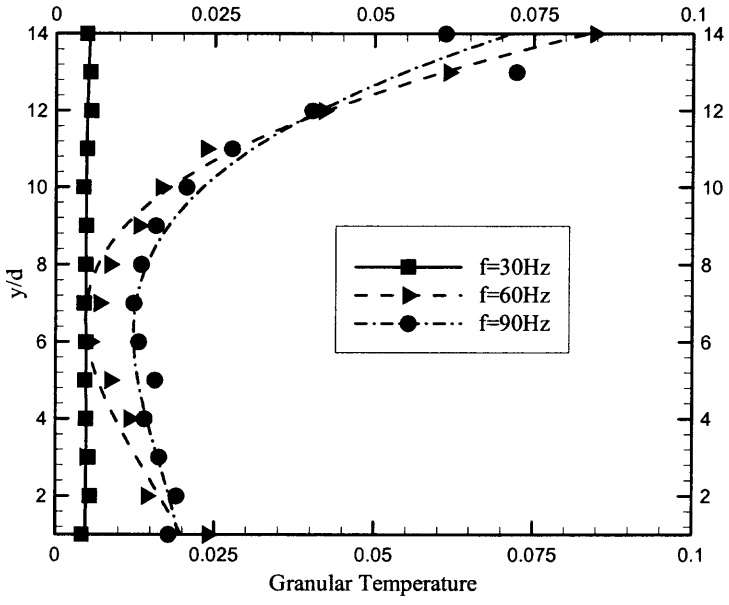

Figure 6.10 Depth profiles of granular temperature (N = 1305, a/d = 0.02, μ_p = 0.3, μ_w = 0.1, e = 0.9) at f = 30, 60, 90 Hz.

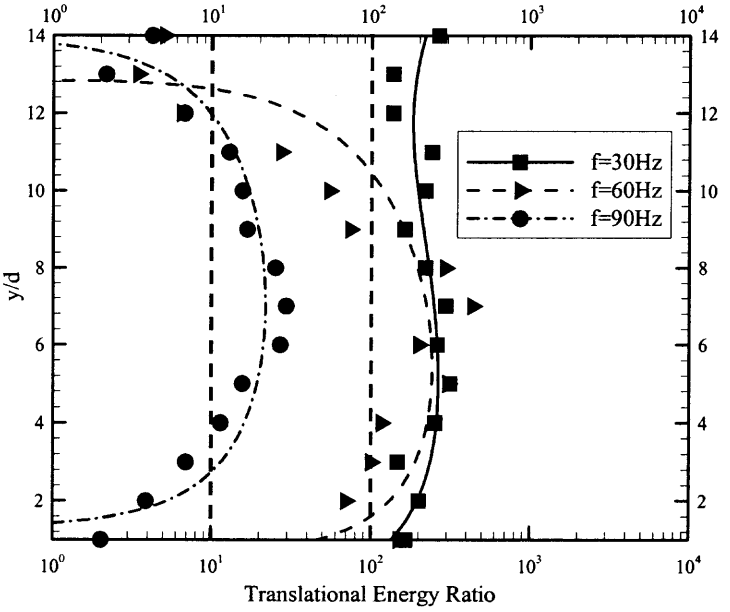

Figure 6.11 Depth profiles of translational energy ratio (N = 1305, a/d = 0.02, μ_p = 0.3, μ_w = 0.1, e = 0.9).

In Figure 6.11, the granular temperature at 30 Hz, (which has no depth gradient), is much smaller than at 60 and 90 Hz, where maximums appears at the surface. Recall that for the shallow bed (Figure 6.3), the highest granular temperature at f = 60 Hz appeared at the surface. At f = 90Hz, however, the depth profiles for the shallow and deep beds are rather different, i.e., the central region of the deep bed is still in solid-thermal phase (Figure 6.11), while the shallow bed is in the thermal phase throughout the depth (Figure 6.4). Such a result is expected since the floor oscillations are less effective in agitating the greater mass overburden of deeper system (where particle velocities are quickly attenuated) as compared to the shallow bed.

From all above analysis, it is clear that a deep particle bed and a shallow particle bed can have different phase patterns under same vibration conditions, which means that bed height has effect on the phase change, in agreement with the conclusion of Thomas et al [41]. The deep particle bed is more difficult to be thermalized because the energy supplied from the bottom will dissipate when transferring to the top, with the increase of height, more energy will disappear during the transfer to the top, which will delay the thermalization of the total particle bed.

6.3 Effect of Friction Coefficient

Frictional properties of the particles are an important characteristic that influences the behavior of the system. Evidence of this was seen in the results summarized in Figure 5.3, which depicts the solids fraction versus friction coefficient μ when particles are "poured". In order to assess the situation when the system is vibrated, the friction

coefficient is varied (μ = 0.0, 0.1, 0.8) in a shallow system (N = 605) for amplitudes a/d = 0.02 and 0.48, and f = 30 Hz.

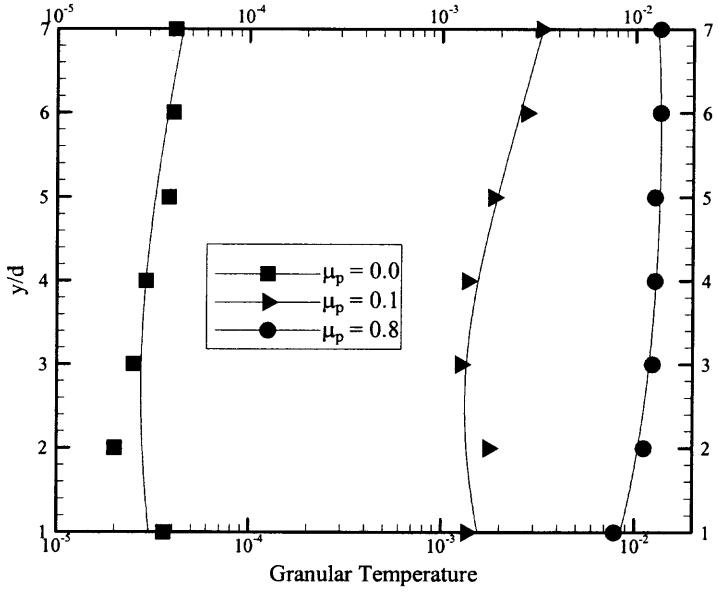

Figure 6.12 Depth profiles of granular temperature for N = 605, a/d = 0.02, e = 0.9, f = 30Hz, $\Gamma \approx 0.46$.

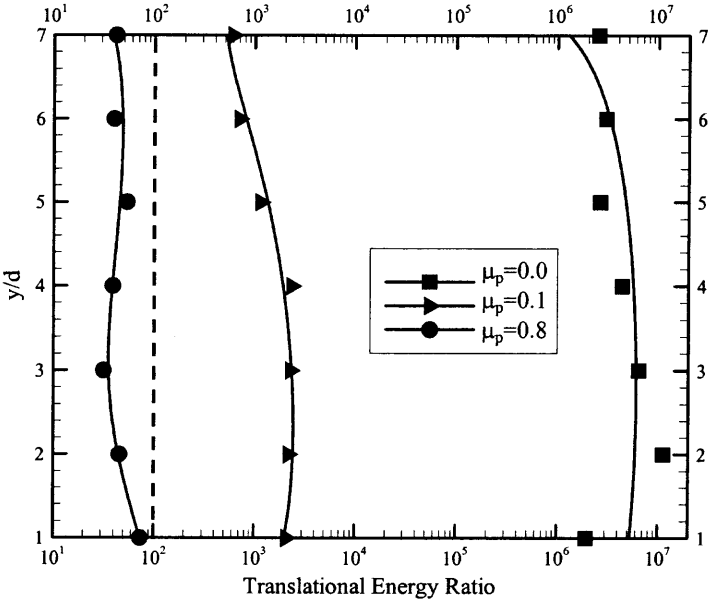

Figure 6.13 Depth profiles of translational energy ratio, for N = 605, a/d = 0.02, e = 0.9, f = 30Hz, $\Gamma \approx 0.46$.

When the vibrations are weak (a/d = 0.02, $\Gamma \approx 0.46$), the bed is not very agitated as evidenced by the rather low granular temperatures in the profiles of Figure 6.12. At these conditions, the system with particles that are more frictional (μ = 0.8) has the largest granular temperature. As was noted previously, particles in this system essentially move in a coordinated manner in that they maintain their relative positions (see Figures. 6.5, 6.6), and so the flow is not collision dominated. It is conjectured that the granular temperature is dictated by the pre-vibrated state in the following sense. Systems with smooth spheres ($\mu = 0$) attain a maximum solids fraction (or equivalently a minimum free volume) when deposited (see Figure 5.3). The resulting tight packing cannot easily be dislodged by weak floor oscillations, thereby yielding a low granular temperature. In contrast, systems with frictional particles are configured with a less dense structure upon pouring so that less energetic floor vibrations can promote larger velocity fluctuations and correspondingly higher relative granular temperatures.

It can be seen in Figure 6.13 that when μ = 0.8, the translational energy ratio is the lowest ($10 < R < 100$), which, according to the definition, signifies that the assembly is in the solid-thermal phase.

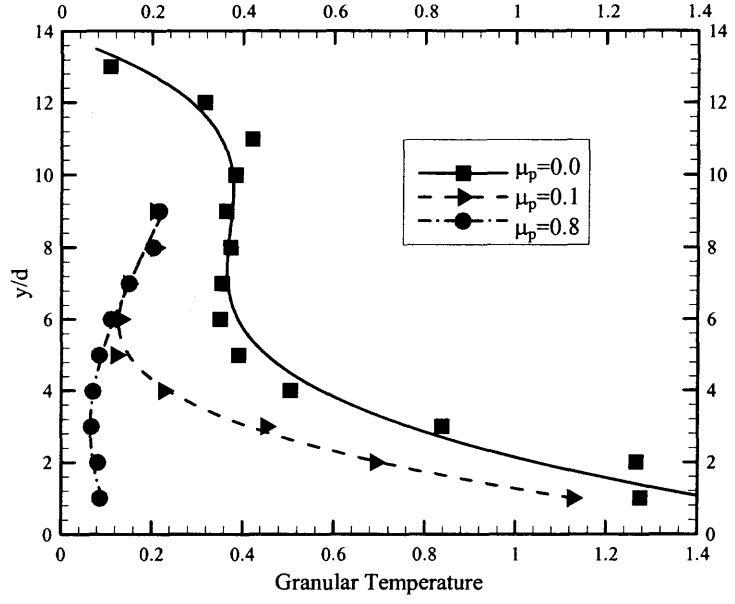

Figure 6.14 Depth profiles of granular temperature, $N = 605$, $a/d = 0.48$, $f = 30$Hz.

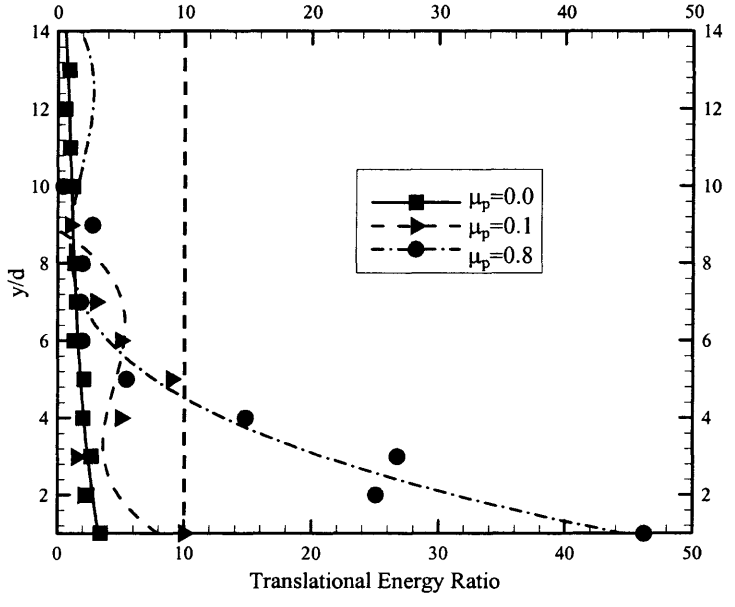

Figure 6.15 Depth profiles of translational energy ratio, $N = 605$, $a/d = 0.48$, $f = 30$Hz, $\Gamma \approx 11$, the region to the left vertical dotted line delineates the solid phase.

When the floor excitations are much stronger (a/d = 0.48, $\Gamma \approx 11$), the smooth particle system (μ = 0, e = 0.9) attains the largest granular temperature (Figure 6.14), expanding to a depth of approximately 13d. The initial pre-vibrated structure is easily destroyed by the energetic floor oscillations so that particle collisions are dominant. Furthermore, according to the R profiles of Figure 6.15 and the phase definitions, the smooth particle system is in a thermal phase, while the frictional bed (μ = 0.8) is only partially thermalized over its upper half. Systems with particles that dissipate more energy during collisions (i.e., those with larger friction coefficients) have available a smaller fraction of the input energy to produce velocity fluctuations, which results in a reduced granular temperature.

6.4 Effect of Normal Stiffness

As mentioned in the Chapter 4, the normal stiffness is derived from the material's Young's Modulus. In the pouring simulation, its effect is not apparent as was shown in Figure 5.5. In this study, three values of normal stiffness K_1 are chosen, while other parameters kept the same. The results are examined for weak (a/d = 0.02, f = 30 Hz) and strong (a/d = 0.48, f = 30 Hz) floor vibrations.

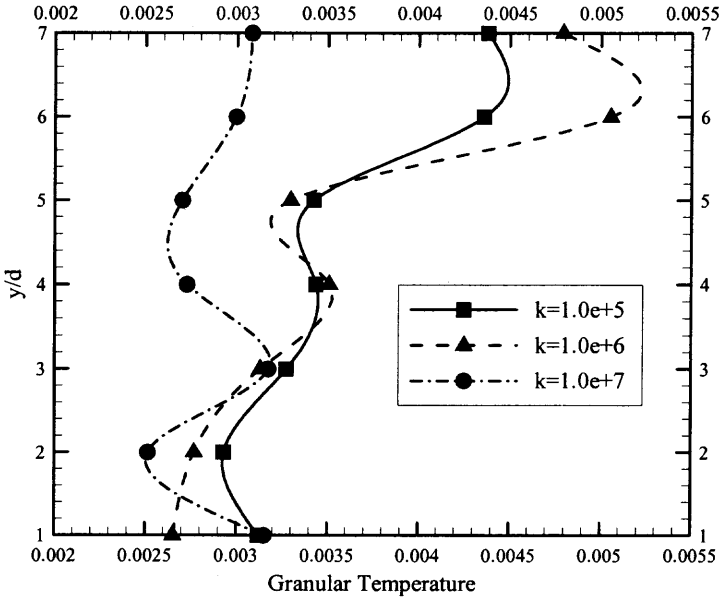

Figure 6.16 Depth profiles of granular temperature, $N = 605$, $a/d = 0.02$, $f = 30$Hz.

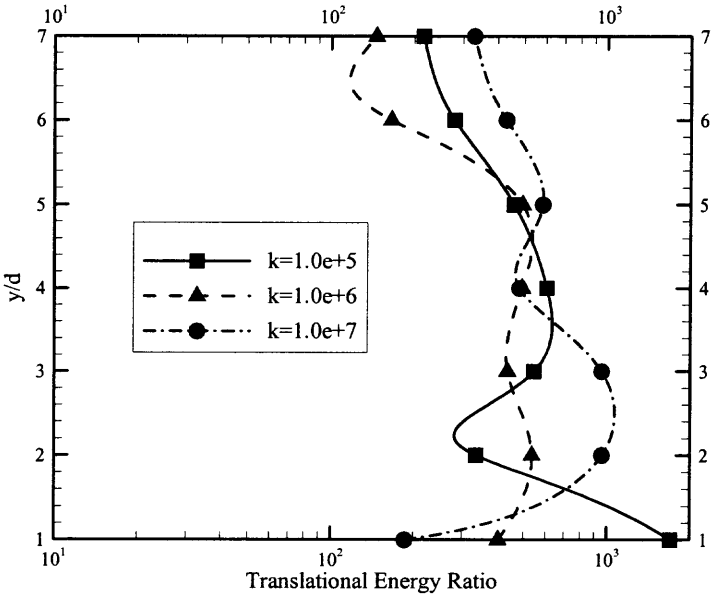

Figure 6.17 Depth profiles of translational energy ratio, $N = 605$, $a/d = 0.02$, $f = 30$Hz.

The depth profiles of granular temperature and translational energy ratio in Figures 6.16 and 6.17, respectively, indicate sensitivity to the value of K_1. However, at the level of floor vibration applied (a/d = 0.02, f = 30 Hz), the systems are in the solid phase since R > 100 throughout the depth, and particles undergo negligible fluctuations.

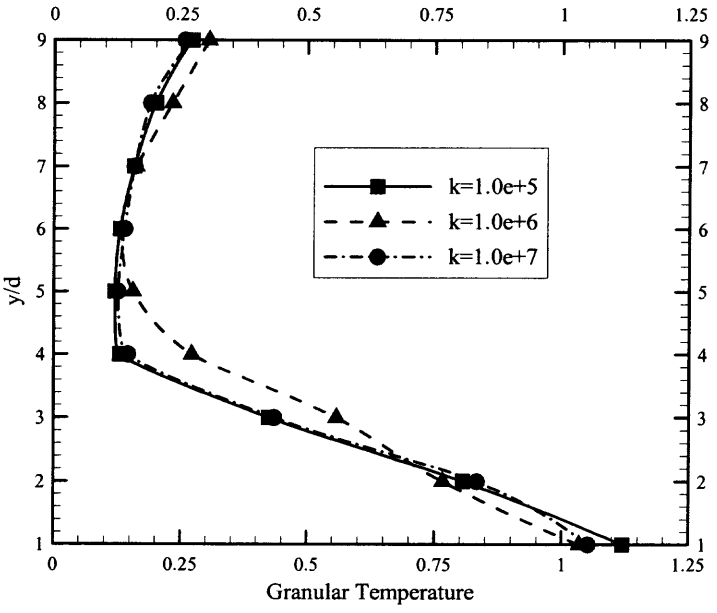

Figure 6.18 Depth profiles of granular temperature, N = 605, a/d = 0.48, f = 30Hz.

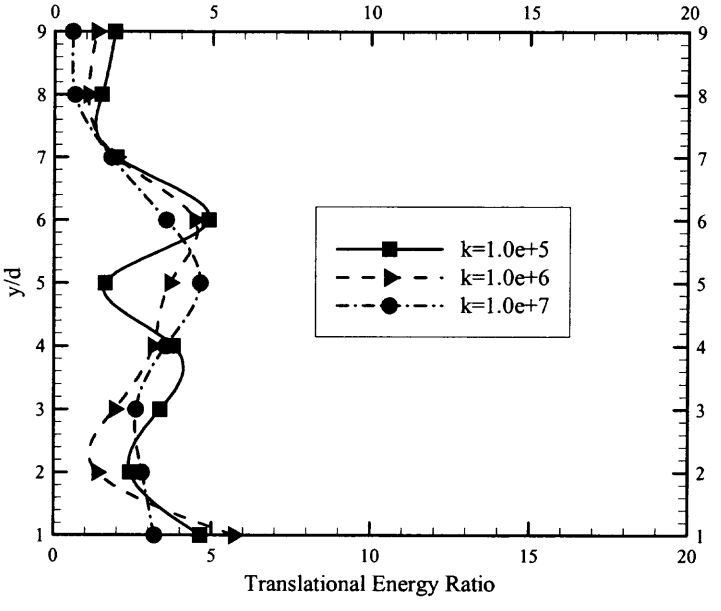

Figure 6.19 Depth profiles of translational energy ratio, N = 605, a/d = 0.48, f = 30Hz.

When the stronger floor vibrations (a/d = 0.02 and f = 30Hz.) are applied, there is little difference in the depth profiles of granular temperature (Figure 6.18) and translational energy ratio (Figure 6.19) for the three K_1 values shown.

6.5 Effect of Restitution Coefficient

As an input parameter to the simulation, the restitution coefficient e provides a means of creating energy dissipation during particle collisions. For a single impact between spheres of masses m_1 and m_2, the energy lost is given by $m_r v_1^2(1-e^2)/2$, where v_1 is the component of incident velocity along the line of centers of one of the particles, and $m_r \equiv m_1 m_2/(m_1+m_2)$ is the reduced mass. Thus it would be expected to see the influence of restitution coefficient on the dynamic granular temperature when particle collisions prevail. This occurs at higher levels of acceleration.

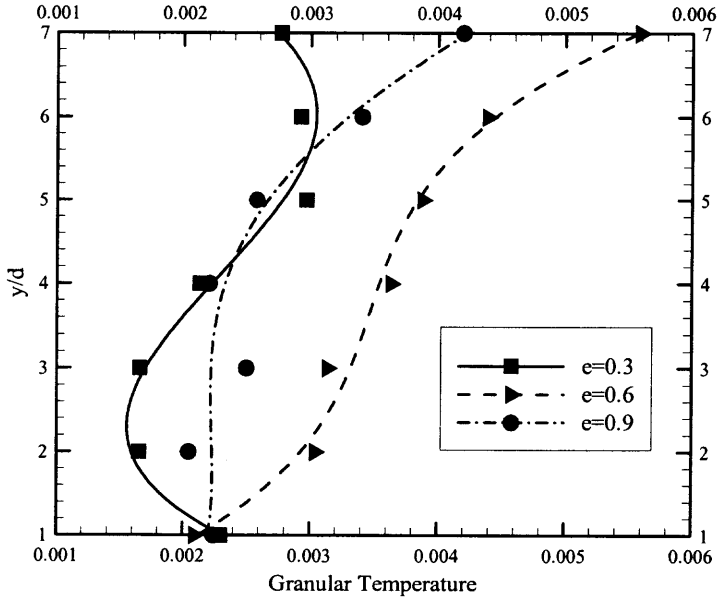

Figure 6.20 Effect of restitution coefficient on granular temperature, N = 605, a/d = 0.02, f = 30Hz.

For each value of e, the dimensionless amplitude a/d is fixed at 0.02, and three frequencies are chosen (f = 30, 60 and 90 Hz, corresponding to Γ = 0.46, 1.84 and 4.14, respectively).

For the small relative acceleration (a/d = 0.02, f = 30Hz.), the granular temperature profiles in Figure 6.20 do not reveal a clear trend on the value of the restitution coefficient. At this level of vibration, particles in the system do not undergo energetic collisions because there is very little relative motion.

The temperature profiles when stronger floor oscillations are used (a/d = 0.02 and f = 60Hz) is shown in Figure 6.21. Here, the system with larger restitution (e = 0.9) experiences a smaller degree of dissipation from collisions, so that a greater fraction of the energy supplied by the floor is available to promote particle fluctuations. Hence, the granular temperature is higher.

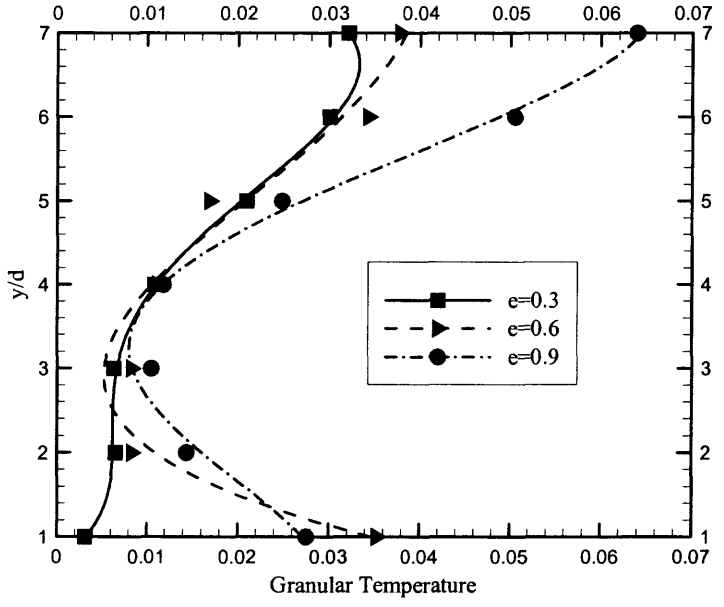

Figure 6.21 Effect of restitution coefficient on granular temperature, N = 605, a/d = 0.02, f = 60Hz.

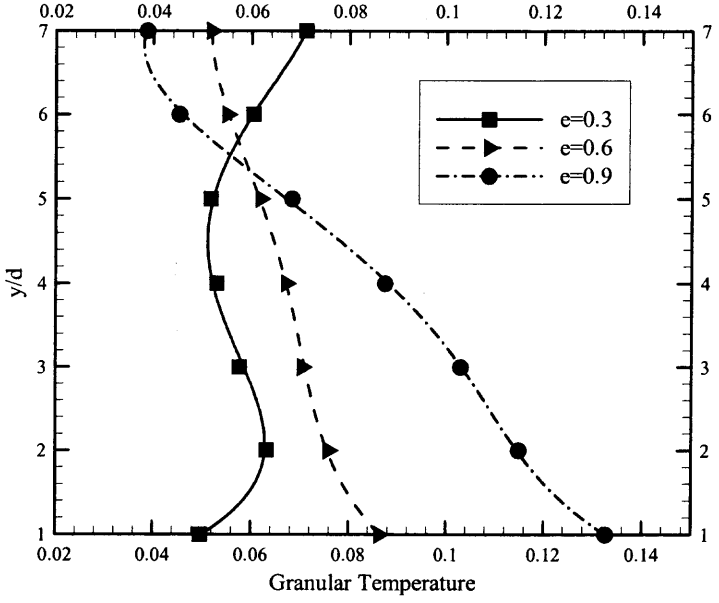

Figure 6.22 Effect of restitution coefficient on granular temperature, $N = 605$, $a/d = 0.02$, $f = 90$Hz.

When the vibration frequency (a/d = 0.02 and f = 90Hz) increases so that Γ = 4.14, Figure 6.22 shows a highly agitated system when e = 0.9, for which the largest temperature appears in the region adjacent to the floor. All of these confirm the explanation.

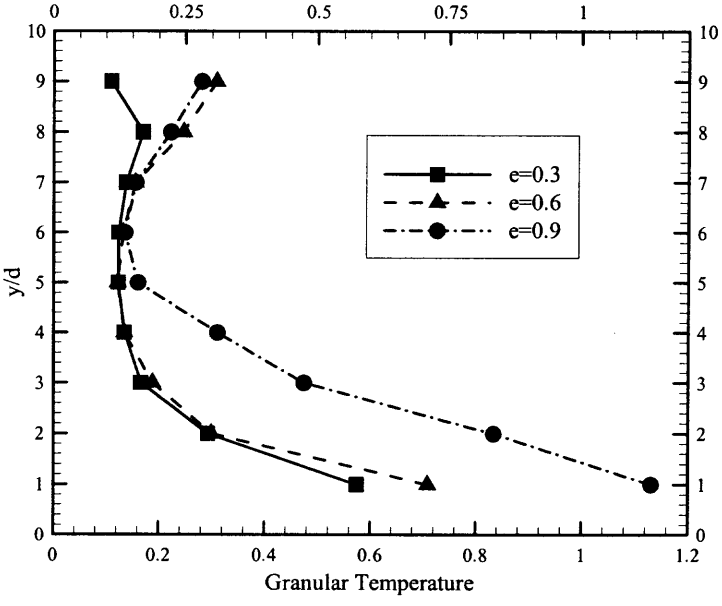

Figure 6.23 Effect of restitution coefficient on granular temperature, $N = 605$, $a/d = 0.48$, $f = 30$Hz.

Finally, when the floor acceleration is increased even further (a/d = 0.48 and f = 30Hz), Figure 6.23 depicts temperature profiles at each value of e that have a similar form, i.e., largest near the floor and decreasing upward to the surface. As expected, particles that are less dissipative (e = 0.9) yield the most agitated system.

From the above analysis, it is clear that when the vibration is weak, the particle bed simply follows the floor, so that particle restitution coefficient does not play an obvious role. As the relative acceleration increases, collisions between the particles become more frequent so that the role of dissipation governed by the restitution coefficient becomes unambiguous.

6.6 Effect of Aspect Ratio of Container

In this study, a constant poured bed depth is maintained as the aspect ratio L/d is varied by adjusting the number of particles in the system appropriately.

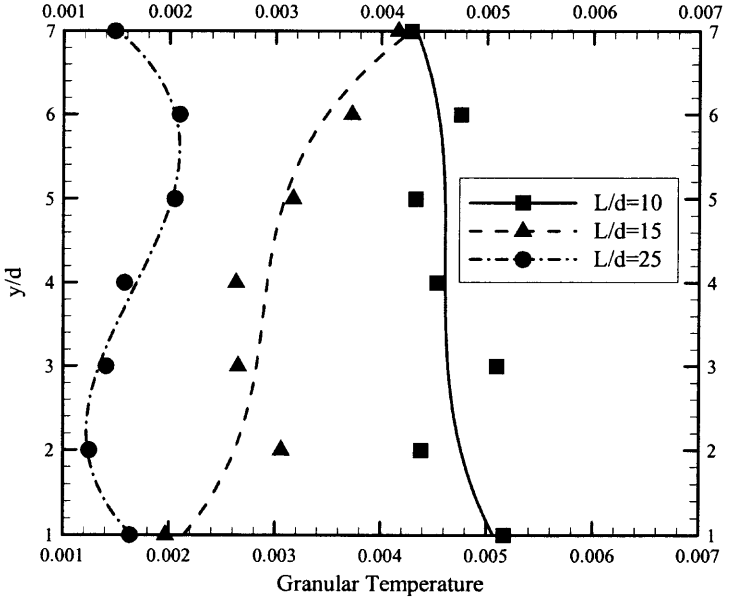

Figure 6.24 Depth profiles of granular temperature, a/d = 0.02, f = 30Hz.

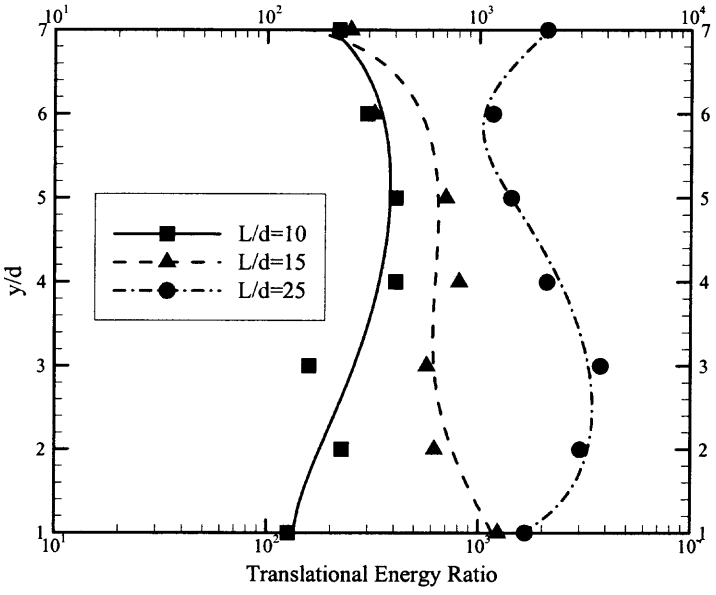

Figure 6.25 Depth profiles of translational energy ratio, $a/d = 0.02$, $f = 30$Hz.

When a weak vibration ($a/d = 0.02$ and $f = 30$Hz.) is imposed on the particle bed, the results in Figures 6.24 and 6.25 shows that the largest granular temperature and smallest translational energy ratio occurs when $L/d = 10$. The reason is that the poured state of this system is the least dense (see Figure 5.8) compared to $L/d = 15$ and 25, so that the free volume enhances particle mobility, which manifests itself in the system having a relatively higher granular temperature, albeit it is small at this level of vibration.

When the frequency is increased to 60 Hz, Figures 6.26 and 6.27 reveal that the temperature and energy ratio profiles are somewhat similar for $L/d = 10$, 15 and 25. The granular temperature is largest at the surface from where it decreases in a monotonic fashion up to within a couple of particle diameters from the floor. It is conjectured that the aspect ratio does not have a pronounced effect on the dynamic states of the assemblies since the magnitude of the vibrations supplied by the base is sufficient to

greatly minimize any influence of the initial poured condition. This is supported by the results shown in Figure 6.28 and 6.29 at $f = 90$ Hz.

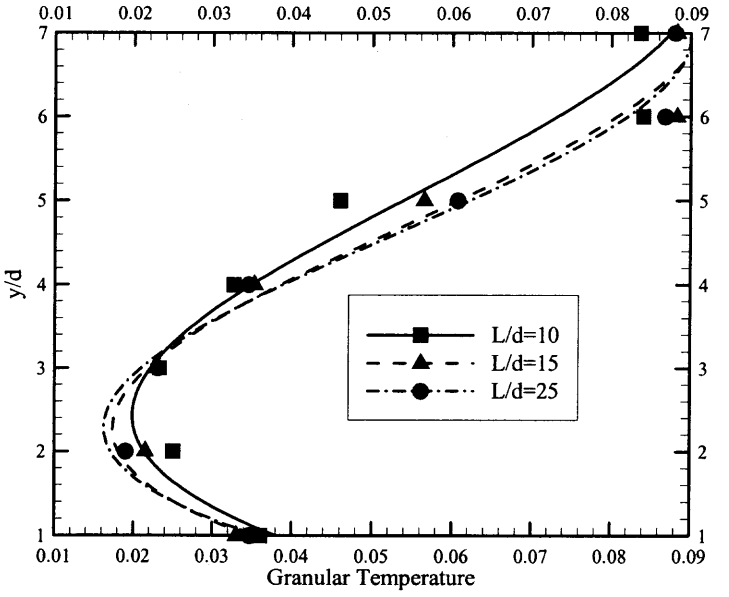

Figure 6.26 Depth profiles of granular temperature, $a/d = 0.02$, $f = 60$Hz.

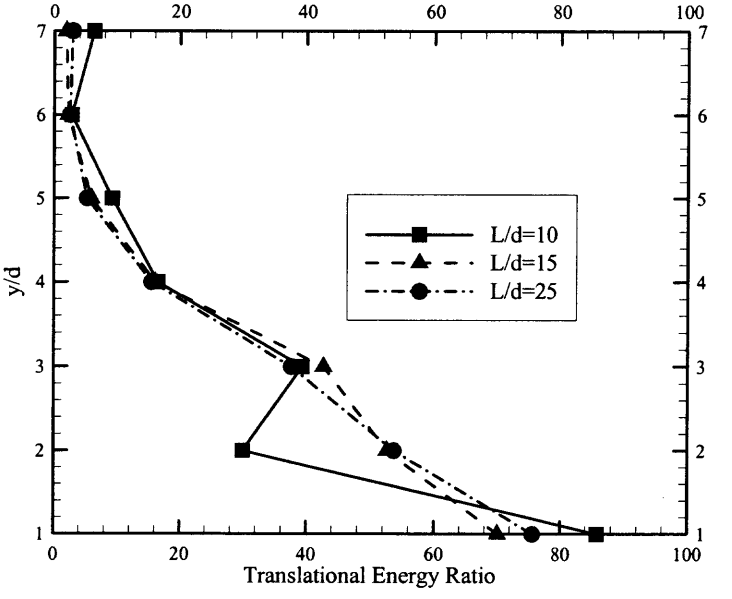

Figure 6.27 Depth profiles of translational energy ratio, $a/d = 0.02, f = 60$Hz.

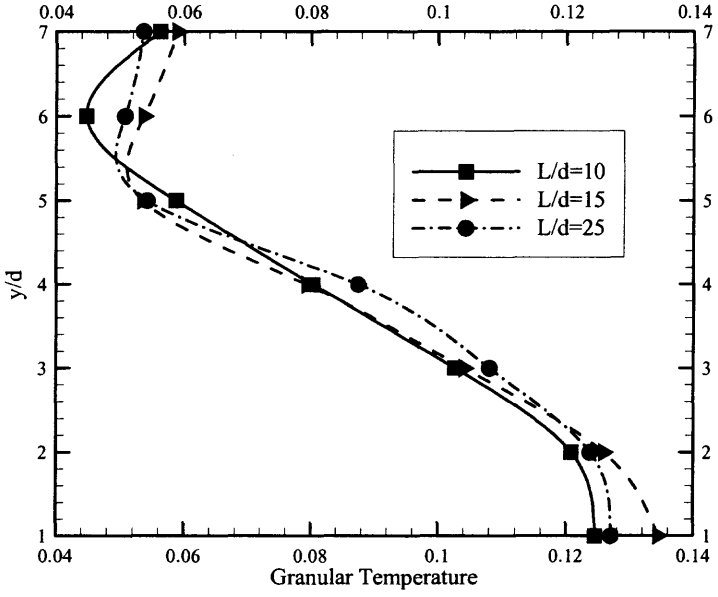

Figure 6.28 Depth profiles of granular temperature, $a/d = 0.02, f = 90\text{Hz}$.

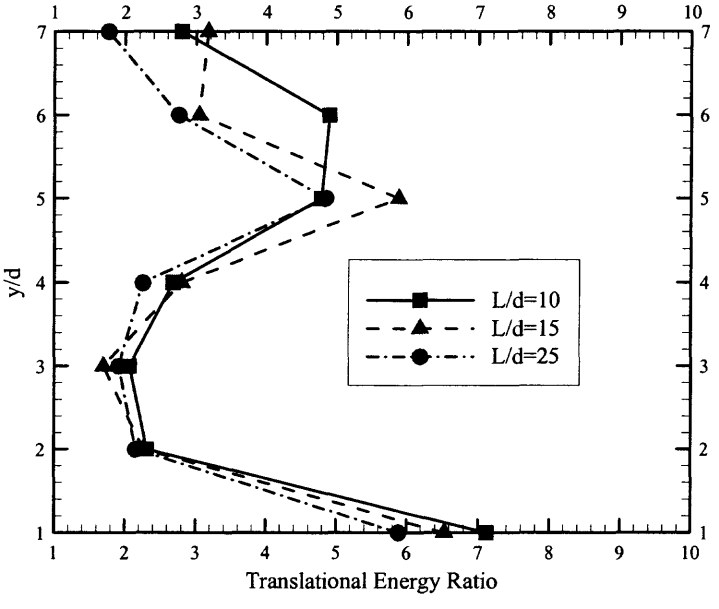

Figure 6.29 Depth profiles of translational energy ratio, $a/d = 0.02, f = 90\text{Hz}$.

6.7 Effect of Initial Poured States

From the above analysis, it is observed that when the relative acceleration is small, the initial poured state is the key that determines the dynamic behavior of the particle assembly. It is also very clear that many factors impact the initial poured states, the difference is that some factors have bigger effects, while others have smaller effects.

6.8 Conclusions

From the above discussion, the following conclusions can be obtained:

1) Under vertical vibrations, fluidization starts from the top surface, in agreement with the experimental observations of Evesque et al. [14]

2) At a large relative accelerations, the depth profiles of granular temperature decrease monotonically from the floor, a behavior that is consistent with kinetic theory predictions [40].

3) At fixed vibratory conditions, the degree of agitation experienced by the particle assembly depends on the depth of the system, a finding in agreement with Thomas et al. [41]. Deeper beds are more difficult to thermalize.

4) At low relative acceleration, particles that are more frictional exhibit a stronger tendency to thermalize to a greater degree. However, at high relative accelerations, the opposite situation exists, i.e., particles with smaller friction coefficients have higher granular temperatures.

5) Normal stiffness has some effect on the dynamic behavior under small relative acceleration, but it has little or no effect under large relative accelerations.

6) Restitution coefficient has little effect on dynamic behaviors under small relative acceleration. At high relative accelerations, with an increase of restitution coefficient, the assembly can be more easily excited.

7) Under large relative accelerations, aspect ratio has little effect on the assembly's dynamic behavior. However, at low relative accelerations, the initial poured state determines dynamic behavior.

CHAPTER 7

RELATIONSHIP BETWEEN INSTANTANEOUS DYNAMIC STATES AND RELAXED SOLIDS FRACTION

The poured and vibrated states of particle beds have been studied in Chapter 5 and Chapter 6. The subject of this chapter is the relationship between the relaxed and dynamic states. The influences of various factors are considered, including:

- Vibration amplitude and frequency
- Bed depth
- Friction coefficient
- Restitution coefficient
- Normal stiffness
- Aspect ratio

Dense random packing is generated, and a phase chart mapping densification improvement verses amplitude and frequency is presented. The essential parameters used in the simulations are given in Table 6.1.

7.1 Effect of Vibration Amplitude & Frequency on the Relaxed States

In 1951, Stewart proposed that a consolidation state of "maximum density" could be attained by the imposition of high frequencies and low amplitudes. In this study, four amplitude ratios are considered (a/d = 0.02, 0.08, 0.24, 0.48) over frequencies ranging between 5Hz and 90Hz. Floor vibrations are applied for 3 seconds, after which the system is allowed to "relax" under gravity until stable. A small system size (N = 605) is used in all cases.

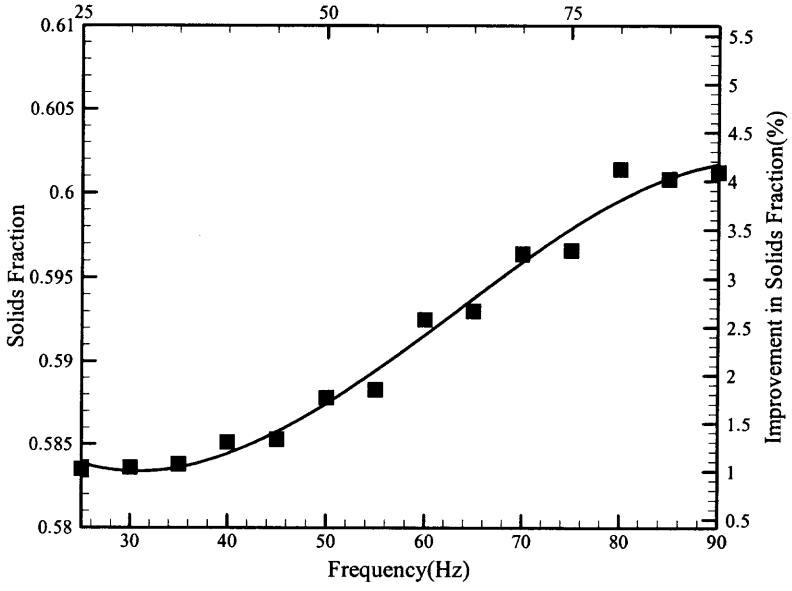

Figure 7.1 Solids fraction behavior against frequency, $N = 605$, $a/d = 0.02$.

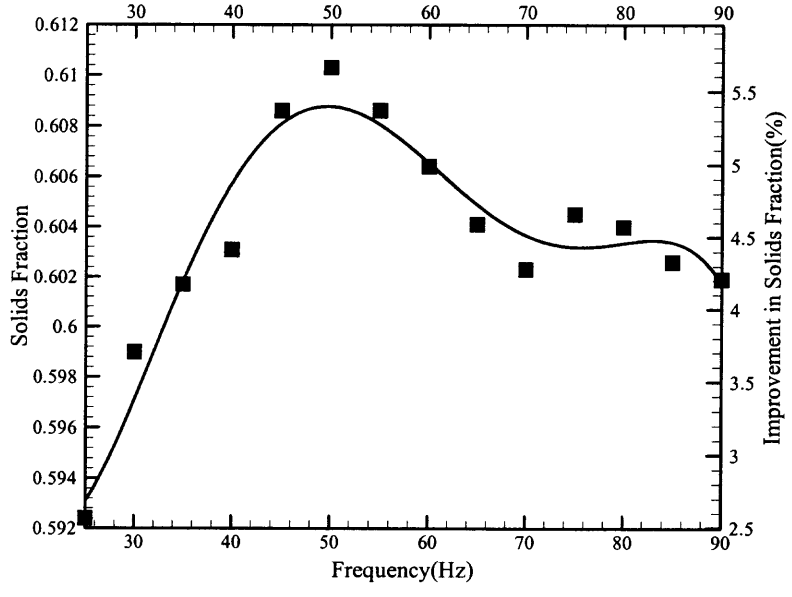

Figure 7.2 Solids fraction behavior against frequency, $N = 605$, $a/d = 0.08$.

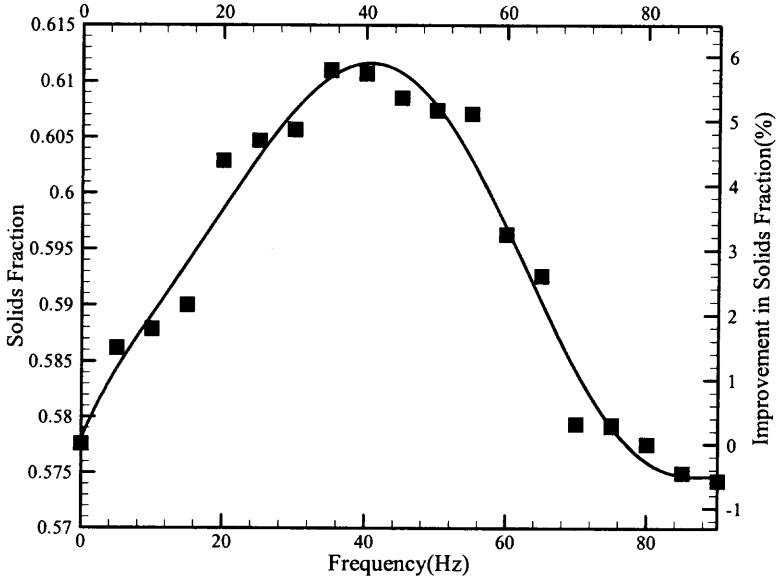

Figure 7.3 Solids fraction behavior against frequency, $N = 605$, $a/d = 0.24$.

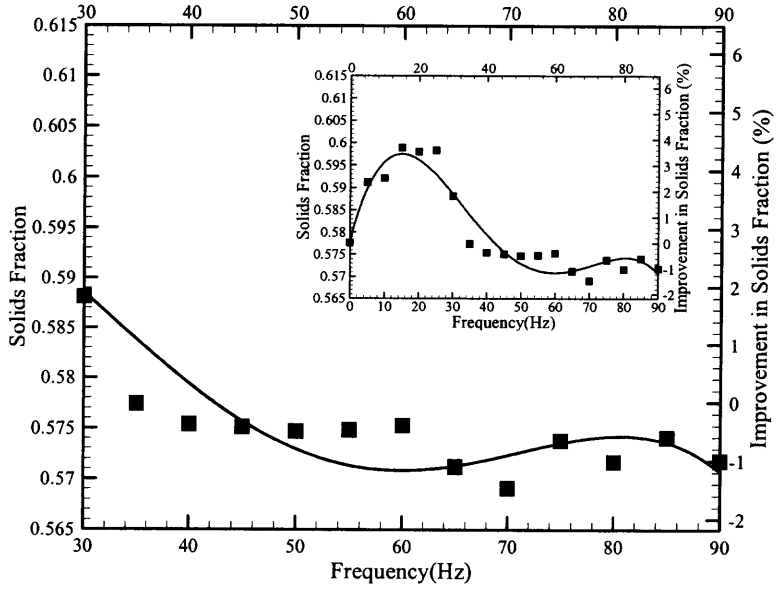

Figure 7.4 Solids fraction behavior against frequency, $N = 605$, $a/d = 0.48$.

The general trend in Figure 7.1 where $a/d = 0.02$ is very much the same as what occurred in the physical experiments (see Figure 2.5). Over the frequency range tested at this amplitude, there is a continual improvement in bulk solids fraction. When $a/d = 0.08$, the curve of Figure 7.2 peaks at approximately 6% near $f \cong 50\,\text{Hz}$, and then it drops slightly with a further increase in frequency. When the amplitude a/d is 0.24, the peak value occurs at approximately 40 Hz, and the curve decays thereafter until, near 80 Hz, no improvement in bulk density is possible at higher frequencies. The occurrence of the peak and decay afterwards is consistent with the experimental observations of Appolonia et al. [5]. Finally, at $a/d = 0.48$, the Figure 7.4 shows only a minimal improvement and that after a critical frequency of approximately 35 Hz, the system does not experience any densification upon relaxation. This trend is analogous to the experiments reported in Chapter 2 (Figure 2.14).

A comparison between the experiments (Figures 2.5-2.14) and the simulation (Figures 7.1-7.4) demonstrates a reasonable qualitative agreement. At peak points, the improvement of solids fraction matches the experimental results, about 6%. Although there are quantitative differences between the simulated and experimental results (possibly attributed to boundary conditions and aspect ratio), the simulation is able to produce all of the important critical phenomena observed in the experiments.

7.2 Relationship between Dynamic States and Relaxed States

At low relative accelerations, the assembly's relaxed solid fraction changes with frequency. Such behavior is evident upon examination of Figures 6.1 – 6.4 in conjunction with Figure 7.1, where the solids fraction increases almost monotonically

with frequency. When f = 30Hz (Figure 6.4), the entire assembly exists in a solid phase, so that the system is only slightly agitated. Consequently, the improvement in mean solids fraction upon relaxation is small. When f = 60 Hz, the top zones are in thermal phase, and the mean solids fraction is larger than the situation at f = 30 Hz. Finally, at f = 90 Hz when the whole assembly is in thermal phase, the system attains the largest improvement in solids fraction after relaxation. Furthermore, as shown in Figures 6.1 and 6.2, more of the bulk mass is displaced towards the floor as frequency increases regardless of the phase of the assembly. It appears that at low relative accelerations, this feature is a key indicator of whether or not the system's bulk solid fraction will improve upon relaxation regardless of its dynamic phase.

The dynamic state of the system at a/d = 0.24 is presented in Figures 7.5 – 7.7. Referring to Figure 7.3, it is observed that at f = 40Hz, the assembly attains the largest improvement in solids fraction upon relaxation. The system is fully thermalized (Fig. 7.7), the maximum granular temperature occurs at bottom, and the greatest fraction of the bulk mass is located within the first four bottom layers.

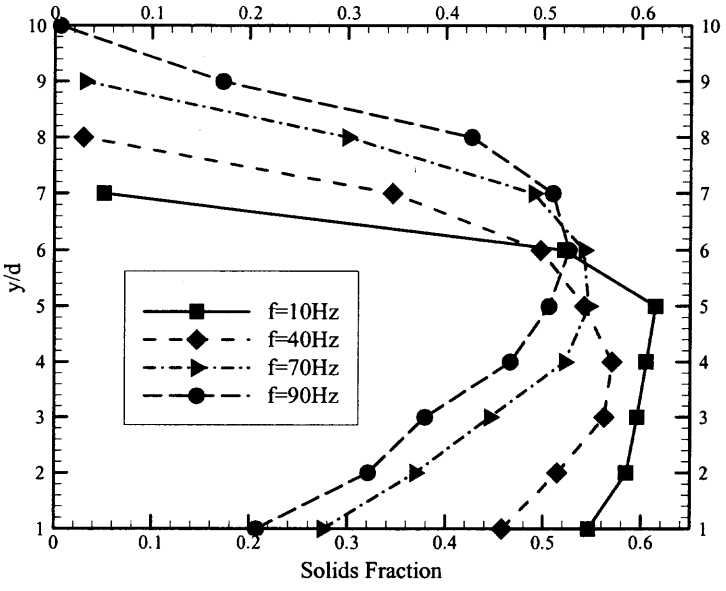

Figure 7.5 Depth profiles of solids fraction, $N = 605$, $a/d = 0.24$.

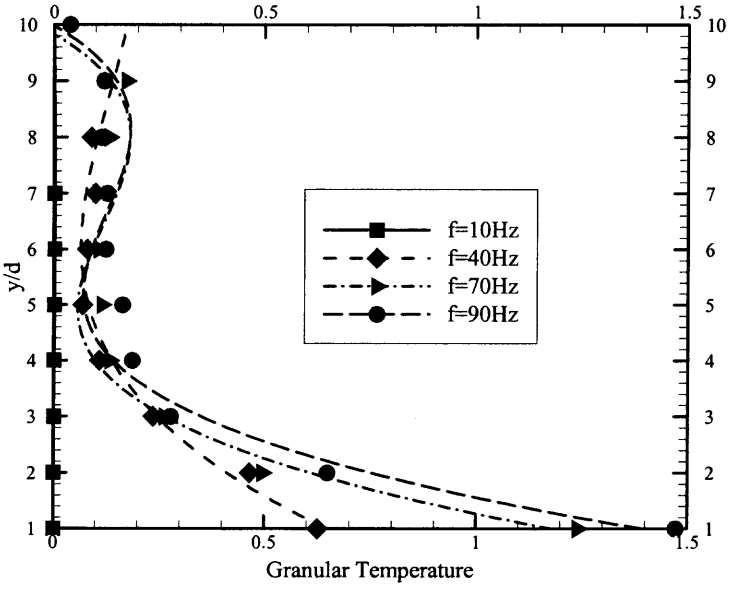

Figure 7.6 Depth profiles of granular temperature, $N = 605$, $a/d = 0.24$.

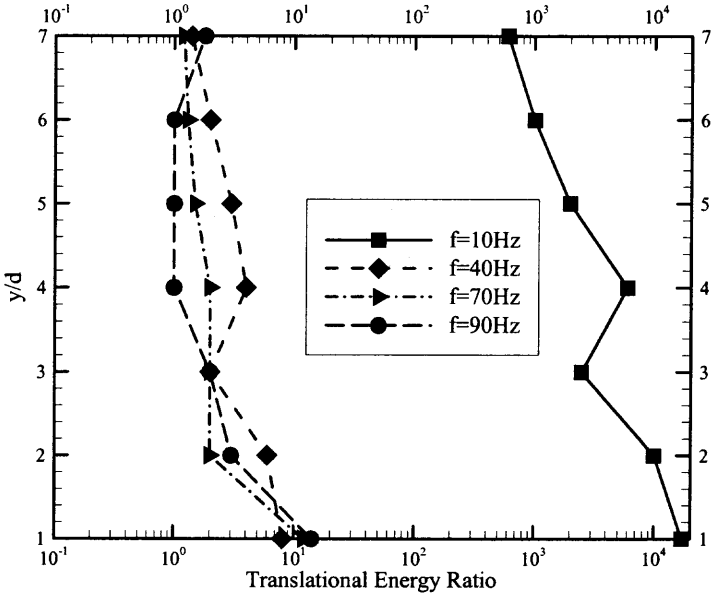

Figure 7.7 Depth profiles of translational energy ratio, $N = 605$, $a/d = 0.24$.

Lastly, at $a/d = 0.48$, the assembly is in a fully thermalized phase throughout its depth at each of the three frequencies ($f = 30$, 60 90 Hz) shown on Figures 6.7 – 6.9, and the granular temperature monotonically decreases from the floor to the surface. However, according to Figure 7.4, the system does not attain a marked improvement in solids fraction at these frequencies when relaxed. Again, the reason (see Figure 6.7) is that the assembly is greatly expanded, almost doubling its depth from the level attained upon completion of the pouring process, so that particles are dispersed throughout the occupied region.

From the above analysis, the following conclusions are made.

1) A large improvement in bulk solids fraction occurs when the pre-relaxed assembly is in a thermal dynamic state and most of the bulk mass lies in the bottom half of the bed.

2) At high relative accelerations (i.e., Figures 7.1 – 7.4), the thermal phase can be divided into *optimum thermal* phase and the *over-thermalized* phase. That is, in the optimal phase, a large improvement (of the order of 6%) in solids fraction occurs upon relaxation, while a system that is over-thermalized experiences little or no change in solids fraction when relaxed.

3) At low relative accelerations, if the assembly has not been fully thermalized throughout its depth and a great fraction of the particle mass lies near the bottom of the bed, the assembly will experience a moderate densification.

7.3 Effect of Bed Height

In order to examine the effect of poured bed height on the relaxed state, the number of particles is increased from N = 605 to N = 1305 while keeping the aspect ratio L/d constant.

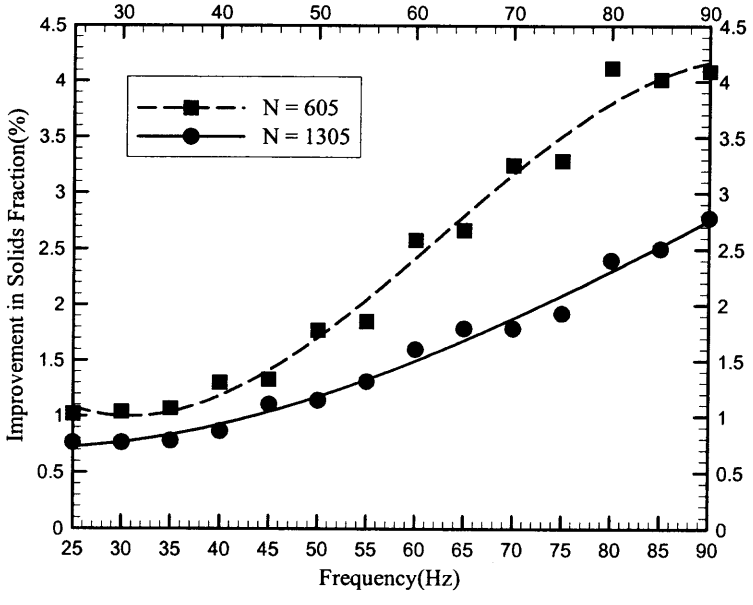

Figure 7.8 Solids fraction evolution with frequency, a/d = 0.02.

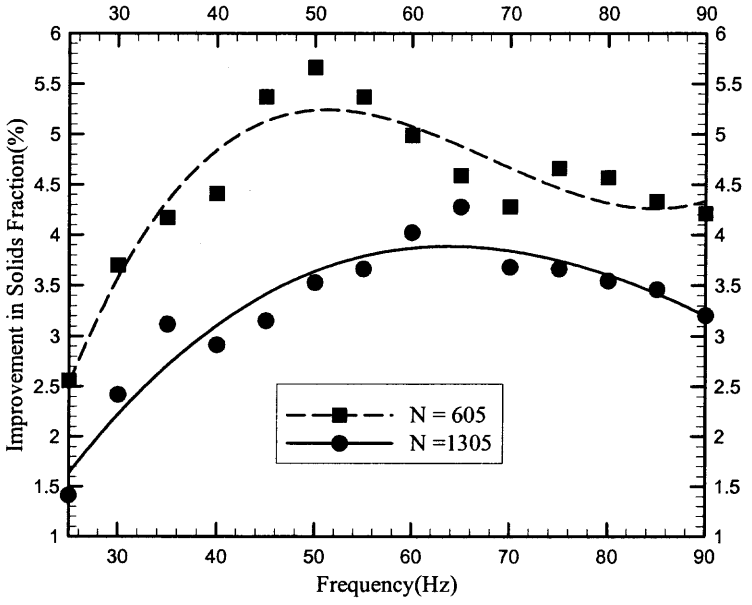

Figure 7.9 Solids fraction evolution with frequency, $a/d = 0.08$.

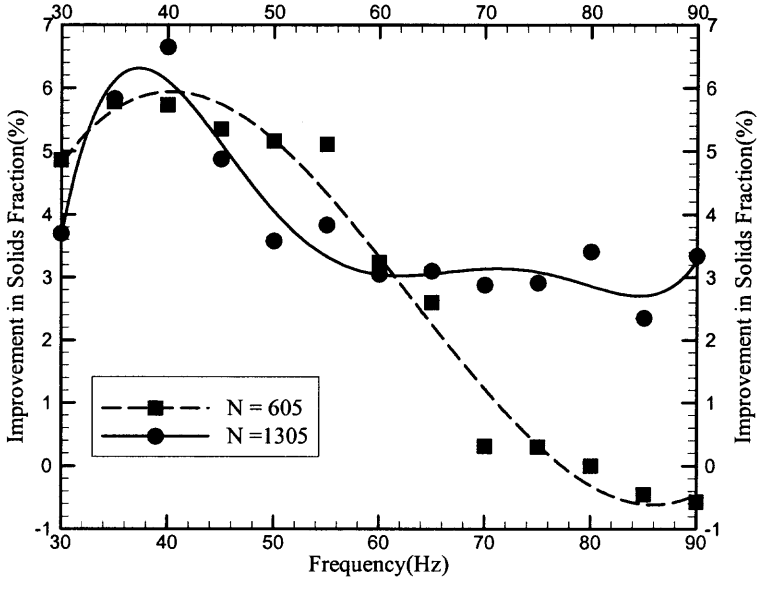

Figure 7.10 Solids fraction evolution with frequency, $a/d = 0.24$.

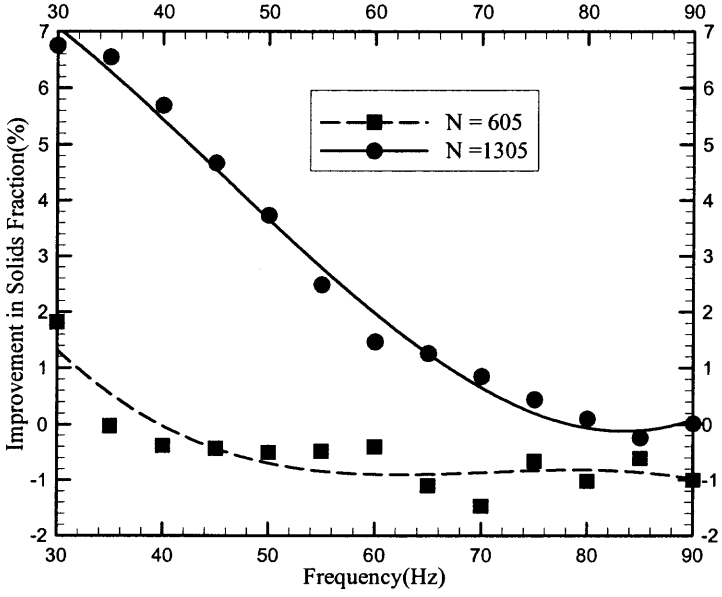

Figure 7.11 Solids fraction evolution with frequency, $a/d = 0.48$.

From the Figures 7.9 - 7.11, it can be observed that when $a/d = 0.02$, both systems have similar trends, the difference being the magnitude of the improvement. This is most likely a consequence of the fact that the larger system does not achieve the same (pre-relaxed) dynamic state (because of its greater mass overburden) as the smaller assembly. When $a/d = 0.08$ (Figure 7.9), the peak improvement of approximately 4.5% occurs at $f \approx 65$ Hz in the deeper assembly, while the values are 5.7% at $f \approx 50$ Hz in the shallow bed. The downward shift in the location of the peak is attributed to the higher relative acceleration required in the deeper assembly to attain a sufficient degree of agitation. A further increase in amplitude to 0.24 (Figure 7.10) produces a peak value of 6.6% at $f =$ 40Hz when $N = 1305$, and a somewhat reduced peak at $f = 35$Hz in the shallower assembly. When $a/d = 0.48$ (Figure 7.11), the larger system attains a maximum solids fraction at $f = 30$ Hz (where optimal dynamic conditions exist). The improvement

monotonically decays to zero at 80 Hz. In contrast, the smaller system is over-thermalized, a peak of less than 2% appears at 30 Hz that quickly decays to zero at 35 Hz, remains around zero up to approximately 60 Hz, after which it begins to oscillate.

Certain generalizations can be deduced from the behavior these two systems. For thin layers, it is possible to produce less dense assemblies after vibration if the acceleration is too high (Figure 7.4). But for deeper systems at the same conditions, some improvement in solids fraction is possible (Figures 7.10 and 7.11). In addition, the relative accelerations corresponding to the peaks in the solids fraction improvement curves increase with the depth of the assembly.

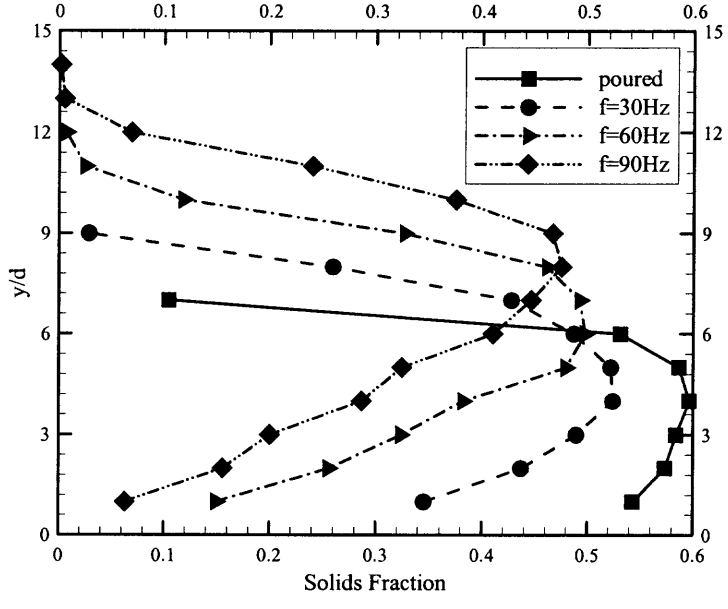

Figure 6.7 Solids fraction depth profiles ($N = 605$, $a/d = 0.48$, $\mu_p = 0.3$, $\mu_w = 0.1$, $e = 0.9$) for the poured state and $f = 30$, 60 and 90 Hz.

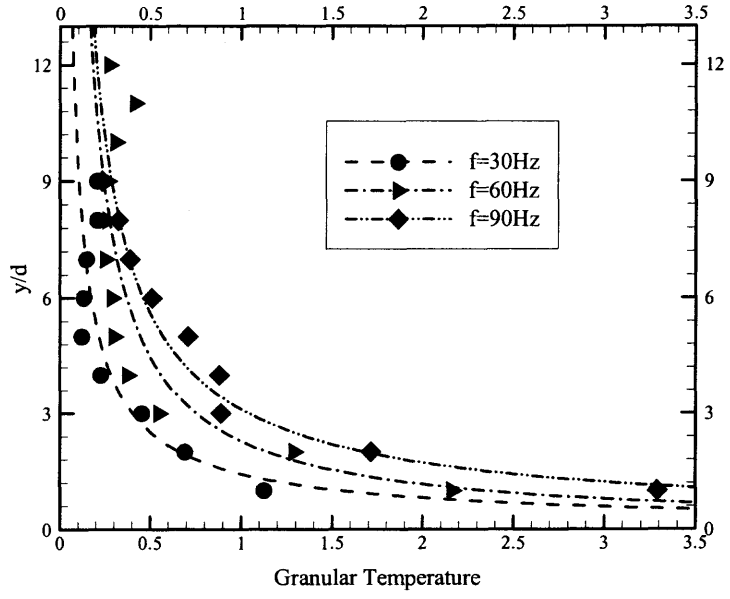

Figure 6.8 Depth profiles of granular temperature ($N = 605$, $a/d = 0.48$, $\mu_p = 0.3$, $\mu_w = 0.1$, $e = 0.9$) for $f = 30$, 60 and 90 Hz.

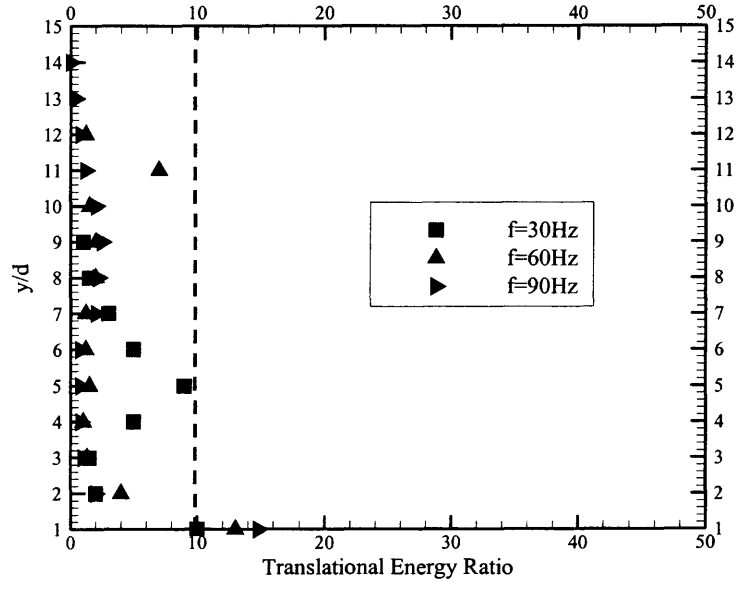

Figure 6.9 Depth profiles of translational energy ratio ($N = 605$, $a/d = 0.48$, $\mu_p = 0.3$, $\mu_w = 0.1$, $e = 0.9$) for $f = 30$, 60 and 90 Hz, the region to the left vertical dotted line delineates the solid phase.

Thus there is a question as to why small systems (shallow beds) do not densify when the relative acceleration is high (Figure 7.4 at $f >$ Hz), but for deep beds at the same vibration conditions an increase in solids fraction takes place upon relaxation (Figures 7.10 and 7.11). In an effort to explain this behavior, reference is made to Figures 6.7, 6.8 and 6.9, where the floor is vibrated at a/d = 0.48 and f = 30, 60 and 90 Hz. As the frequency is increased, the bed expands accompanied by a depletion of particles adjacent to the floor, and a shift of the maximum in the solids fraction profile upwards.

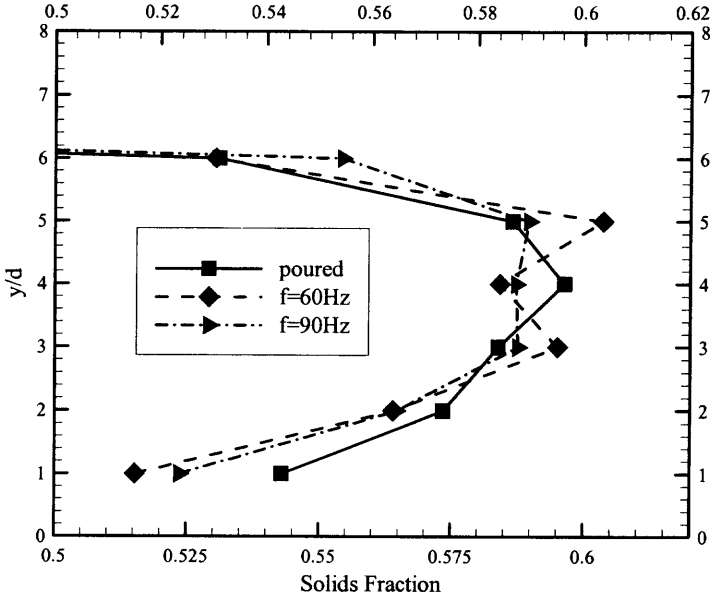

Figure 7.12 Depth profiles of solids fraction for the poured state and at f = 60 and 90Hz when a/d = 0.48 after relaxation (N = 605).

Figure 7.12 shows a comparison of the relaxed solids fraction depth profiles for the poured state and at f = 60 and 90 Hz (N = 605). It can be seen that the region adjacent to the floor forms into a somewhat less dense structure when relaxed in comparison with the initial poured assembly. The dilution of the region adjacent to the floor in the dynamic state may play a role in the overall solids fraction being less than its initial value (i.e., after pouring) when the relative acceleration is too high. Thus, for thin layers at

large values of relative acceleration, the assembly may find itself in a less dense condition after relaxation, which, in a physical experiment, occurs upon stopping the vibrations.

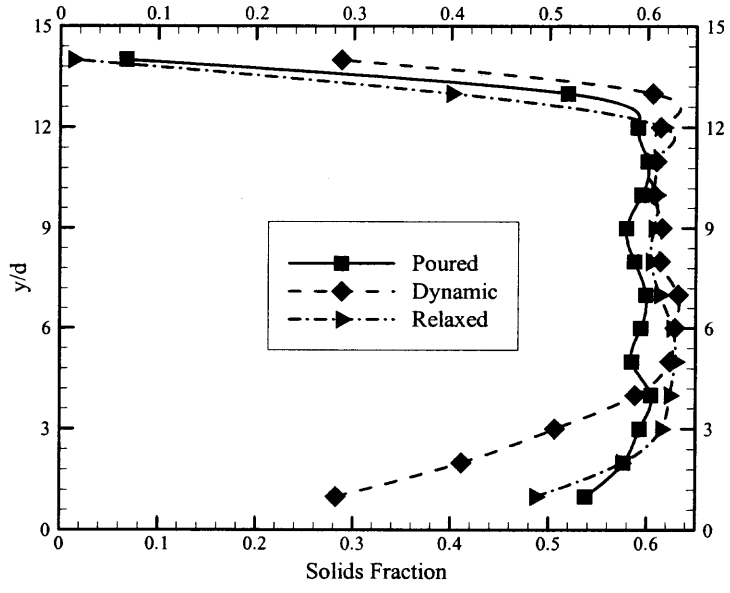

Figure 7.13 Depth profiles of solids fraction, $N = 1305$, $a/d = 0.48, f = 60\text{Hz}$.

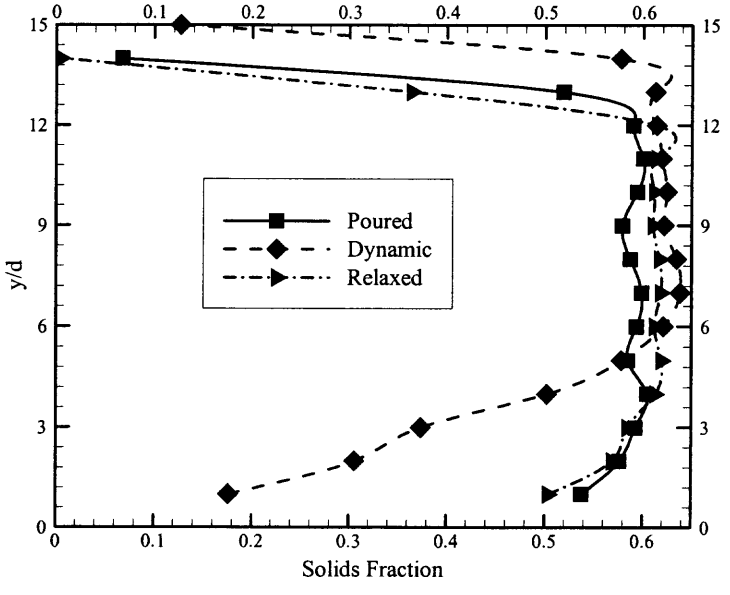

Figure 7.14 Depth profiles of solids fraction, $N = 1305$, $a/d = 0.48, f = 90\text{Hz}$.

Figures 7.13 and 7.14 shows the poured, dynamic and relaxed states for the deeper assembly (N = 1305) at 60 and 90 Hz, respectively when a/d = 0.48. As the curves indicate, relaxation of these dynamic assemblies favors a redistribution of the particles that results in an improvement of the overall solids fraction.

7.4 Effect of Friction Coefficient on Densification

The results in Chapter 6 demonstrated that the inter-particle friction coefficient μ_p plays an important role on the dynamic state. In this section, the effect of friction on densification upon relaxation is examined.

Figure 7.15 shows solids fraction improvement versus frequency curves at a/d = 0.02 for μ_p = 0, 0.1 and 0.8. All assemblies become more dense after relaxation, although the system consisting of smooth particles (μ_p = 0) exhibits the smallest values and its curve contains a maximum at $f \cong 75\,\text{Hz}$. At a higher vibration amplitude (Figure 7.16) a/d = 0.08, all three systems become more dense after relaxation with each curve showing a peak. Again, the smooth particle system has the smallest values. For both amplitudes, the rough sphere systems (μ_p = 0.8) attain the greatest solids fraction improvement. The high friction system reaches a peak in the improvement curve at a higher frequency, the reason being that the assembly requires more input energy from the floor vibrations to reach a thermal phase due to large energy dissipation during the collisions among particles. When a/d = 0.24, the smooth particle assembly is unable to achieve any substantial increase in solids fraction (suggesting that it is over-thermalized), in contrast to the frictional particle systems. Also, the 0.8 frictional particle system experiences a bulk density increase throughout the range of tested frequencies shown on Figure 7.17,

while beyond 75 Hz, no improvement in solids fraction occurs in the slightly frictional particle assembly (μ_p =0.1). Upon doubling the amplitude to a/d = 0.48 (Figure 7.18), systems with both smooth and slightly frictional particles (μ_p =0, 0.1) show no improvement in solids fraction at any frequency. The system with the greatest inter-particle friction exhibits a decaying improvement curve until, at $f \cong 60$ Hz, a reduction in bulk density takes place. In fact, the 75 Hz vibrations place the system in a dynamic state such that upon relaxation, the solids fraction becomes approximately 4% smaller than it was after pouring. A principal finding from this series of simulations is that smooth particle assemblies do not attain a substantial increase in bulk density (i.e., approximately 5%) after vibrations are applied.

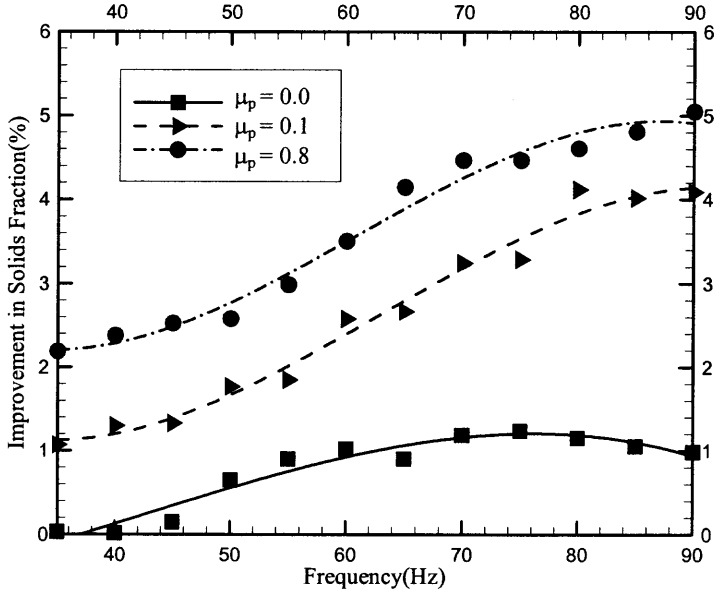

Figure 7.15 Solids fraction versus frequency, $N = 605$, $a/d = 0.02$ ($0.32 \leq \Gamma \leq 2.07$).

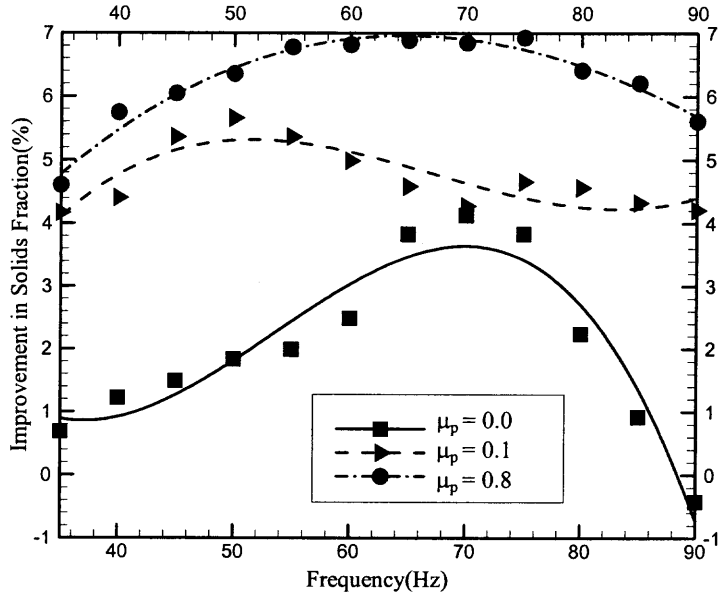

Figure 7.16 Solids fraction versus frequency, $N = 605$, $a/d = 0.08$ $(1.25 \leq \Gamma \leq 8.28)$.

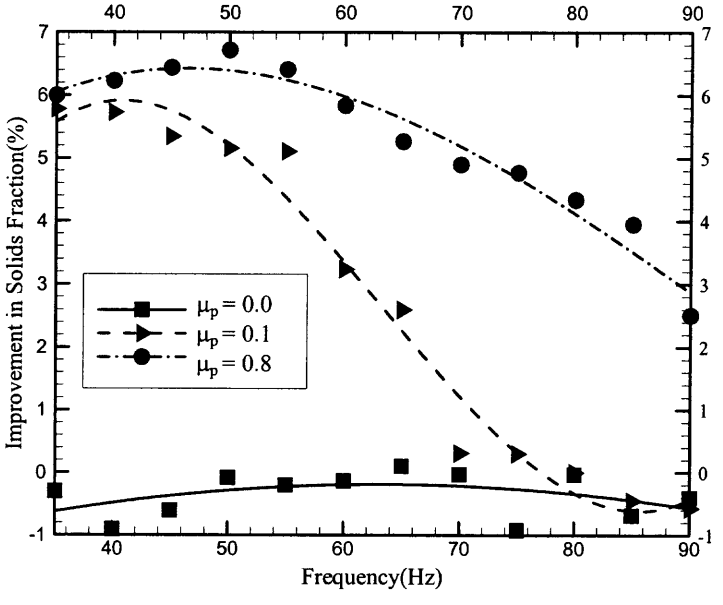

Figure 7.17 Solids fraction versus frequency, $N = 605$, $a/d = 0.2$ $(3.75 \leq \Gamma \leq 24.8)$.

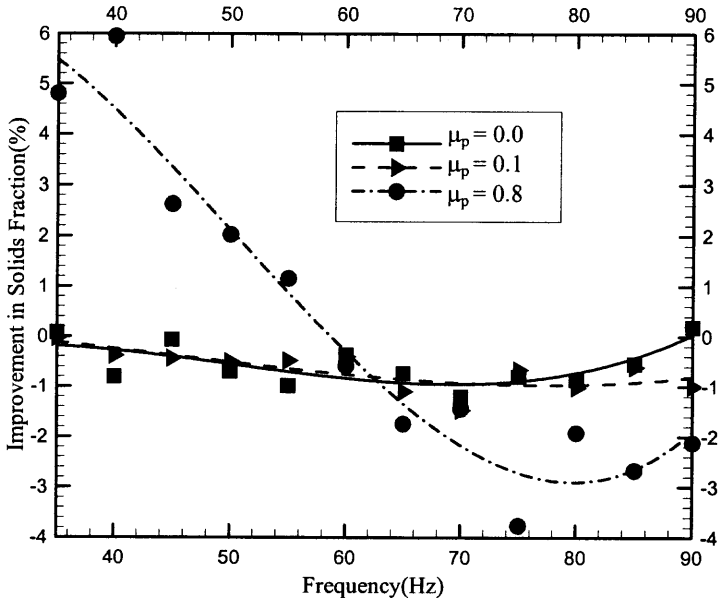

Figure 7.18 Solids fraction versus frequency, $N = 605$, $a/d = 0.4$ ($7.5 \leq \Gamma \leq 49.7$).

In order to understand the physical rationale for the behaviors discussed above, reference is made to the dynamic analysis presented in Section 6.3 (Figures 6.12 – 6.15). In Figure 7.15, the general trends of three systems are similar, but the improvement in solids fraction is different. When vibrated, the high friction assembly ($\mu_p = 0.8$) maintains the largest granular temperature (Figure 6.12), and the translational energy ratio profiles (Figure 6.13) indicate that the particles undergo more sizeable lateral motions (albeit small) compared with the smooth ($\mu_p = 0$) and lower frictional particles ($\mu_p = 0.1$). At the vibration levels applied ($a/d = 0.02, 35\,\text{Hz} < f < 90\,\text{Hz}, \; 0.32 \leq \Gamma \leq 2.07$), this relatively low density assembly experiences a global rearrangement process that depends, in part, on the lateral mobility of the particles. If this conjecture is accepted, then the improvement curves for the smooth and low friction systems (whose particles undergo significantly smaller lateral displacements as can be seen from their large translational

energy ratio profiles in Figure 6.13) would necessary lie below that of the high friction particle system. Equally important to the trends with friction illustrated in Figure 7.15 is "proximity" of the poured solids fraction (see Figure 5.3) to that of a loose random packing. If this value is taken as 0.61, then high friction particle system (μ = 0.8) is at 91.1% ($\nu_{pour}/0.61\times100=91.1$), while the smooth and lower friction particle assemblies are at 97.3% and 94.8%, respectively. Thus, after pouring, the high friction particle system has the greatest capacity to undergo an increase in bulk density.

In Figure 7.18, the lack of any densification for the smooth and μ = 0.1 assemblies is a consequence of them being in over-thermalized states (Figure 6.14 and 6.15). However the highly friction system (μ = 0.8) does experience a substantial improvement in solids fraction because at f = 35Hz it is in a mixed solid-thermal and thermal phase.

7.5 Effect of Aspect Ratio on Densification

In Chapter 6, it was shown that at low relative accelerations, the dynamic states of an assembly are, in a sense, controlled principally by initial poured structure, which in turn depends on the aspect ratio of the containment geometry. However, with an increase in relative acceleration, the influence of aspect ratio is minimized. In this section, the influence of aspect ratio on relaxed systems is considered.

Figure 7.19 presents the percentage improvement in solids fraction versus frequency at aspect ratios L/d = 10, 15 and 25 when the relative acceleration is small (a/d = $0.02, \Gamma \leq 2.07$). The system with the largest aspect ratio attains the smallest improvement under these small accelerations because the larger poured solids fraction

(see Figure 5.8 and Table 5.2) makes the system less sensitive to the vibrations. However, when the vibration intensity reaches some level, the effect of initial poured states becomes minimal.

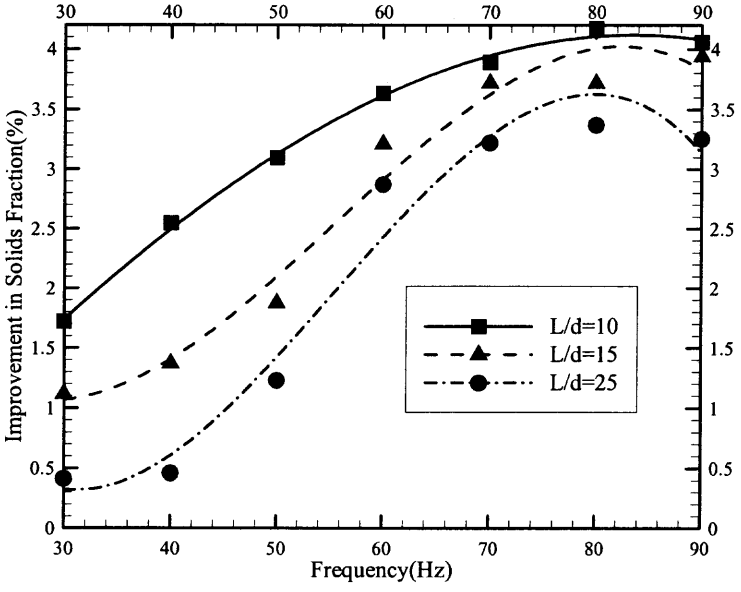

Figure 7.19 Solids fraction versus frequency, $a/d = 0.02$.

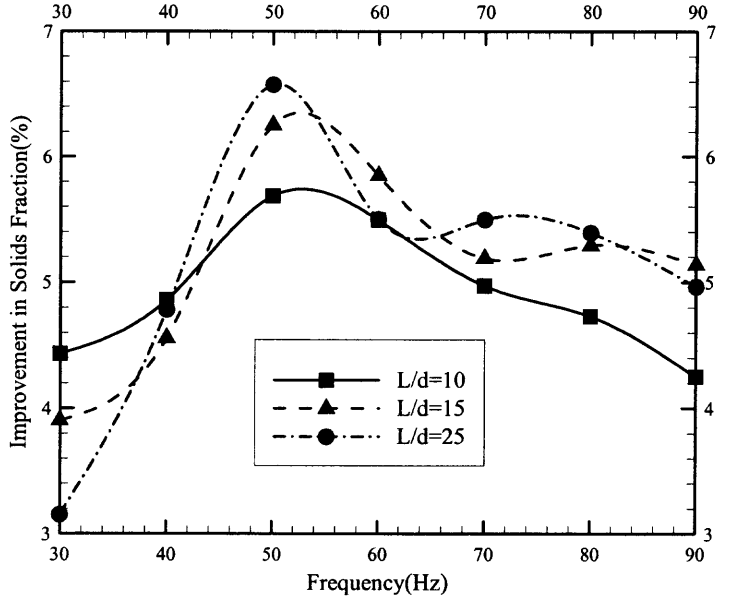

Figure 7.20 Solids fraction versus frequency, $a/d = 0.08$.

This can be seen in Figure 7.20 at a higher vibration amplitude (a/d = 0.08). When $f \leq 40$ Hz, the system with the largest aspect ratio (L/d = 25) shows the least improvement in solids fraction. However, the trend reverses when $f \geq 40$ Hz so that the largest system now attains the largest improvement.

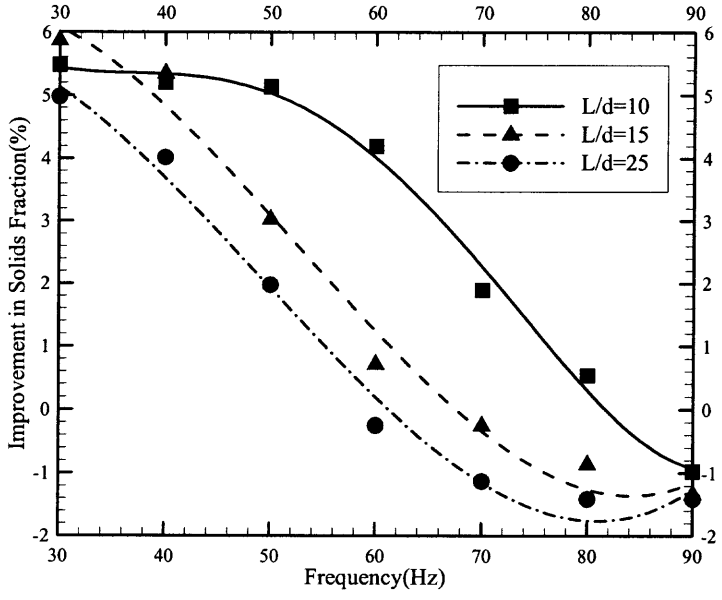

Figure 7.21 Solids fraction versus frequency, a/d = 0.24.

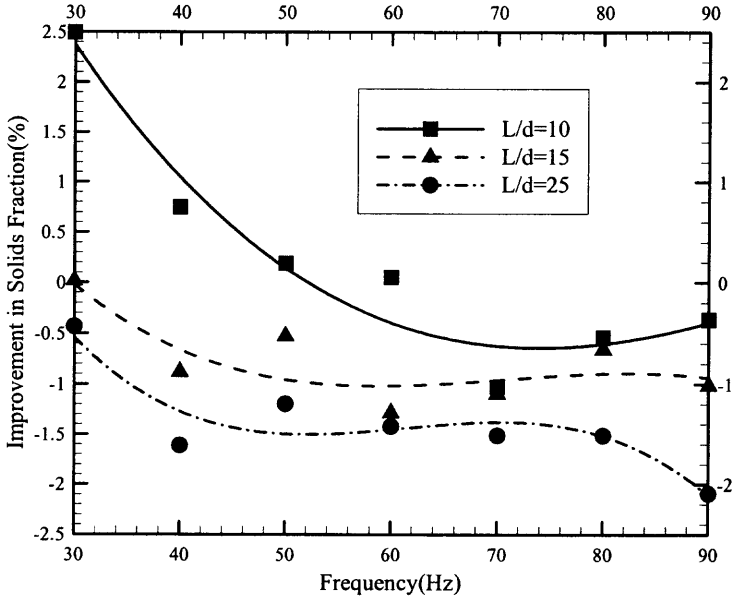

Figure 7.22 Solids fraction versus frequency, a/d = 0.48.

Figures 7.21 and 7.22 indicate that the trends of the improvement curves for the different aspect ratios are quite similar, although their magnitudes are not the same. That is, for example, the improvement becomes worse as frequency increases in these figures.

In summary, for each fixed *a/d* values, the results reveal that the overall trends of the improvements curves are similar.

7.6 Effect of Restitution Coefficient on Densification

When the relative acceleration is small so that particle fluctuations are minimal, the coefficient of restitution does not play an important role on the dynamic state of an assembly (See Chapter 6). However, as the assembly becomes more energetic at higher vibrations, there is more collisional dissipation through the restitution coefficient *e*. Hence, the value of *e* has an effect on the dynamic state of the assembly. In this section, the role of normal restitution on the relaxed state is considered.

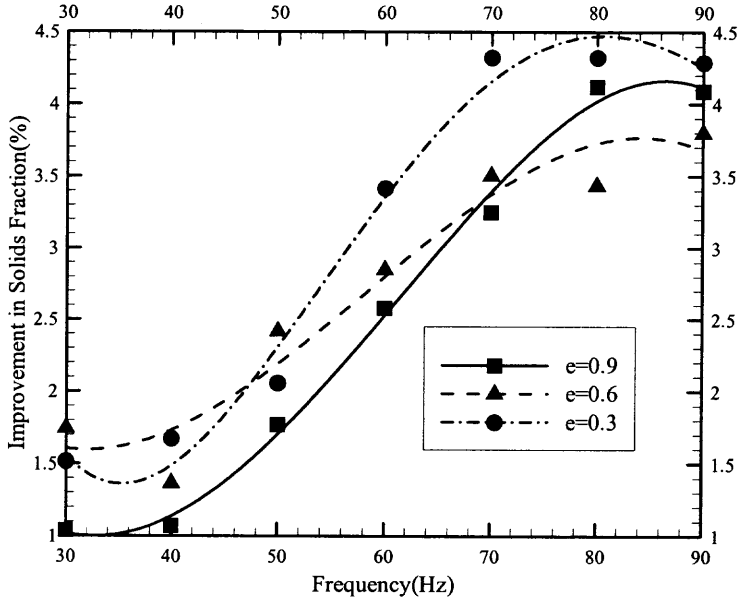

Figure 7.23 Solids fraction versus frequency, $N = 605$, $a/d = 0.02$.

Figure 7.23 shows the percentage improvement in solids fraction (after relaxation of the dynamic state) against floor vibration frequency for e = 0.3, 0.6 and 0.90 under small relative accelerations (a/d = 0.02). While the curves do exhibit some differences in the degree of improvement, they all have very similar trends. Consequently, it appears that the system is not extremely sensitive to the exact value of the restitution coefficient. A similar level of insensitivity of the dynamic state on the restitution coefficient was seen in Chapter 6 (Section 6.5).

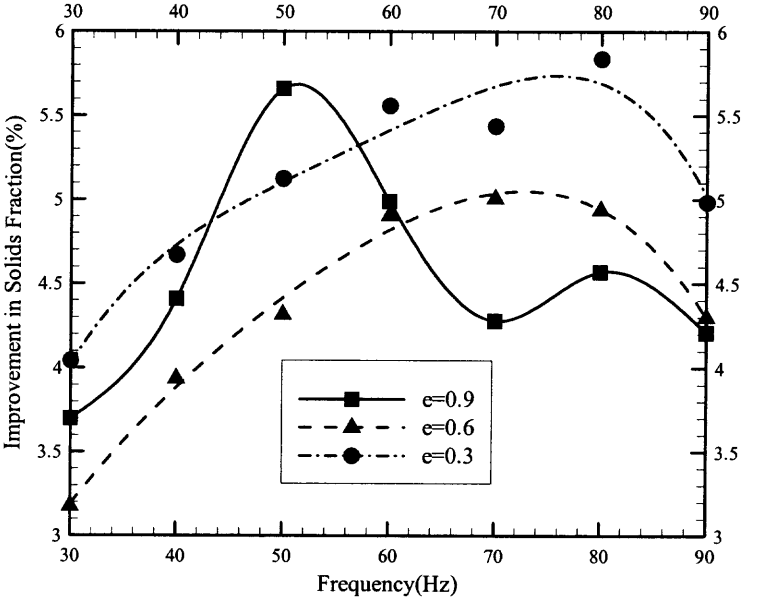

Figure 7.24 Solids fraction versus frequency, $N = 605$, $a/d = 0.08$.

As the vibration amplitude is increased (a/d = 0.08), Figure 7.24 shows that restitution coefficient begins to play a role. For the case where e = 0.9, the solids fraction reaches its maximum value when f = 50Hz, it then decreases up to 70 Hz, after which is oscillates. When e = 0.6 and 0.9, the assemblies attain the greatest improvement in solids fraction at approximately 70Hz and 80Hz, respectively. The assembly having the largest

restitution coefficient particles experiences the smallest dissipation and thus it becomes thermalized at a lower frequency that the other systems.

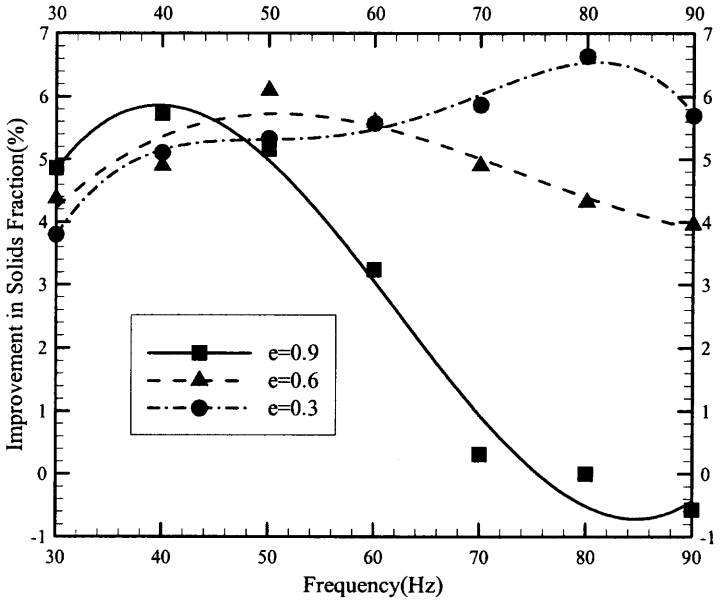

Figure 7.25 Solids fraction versus frequency, $N = 605$, $a/d = 0.24$.

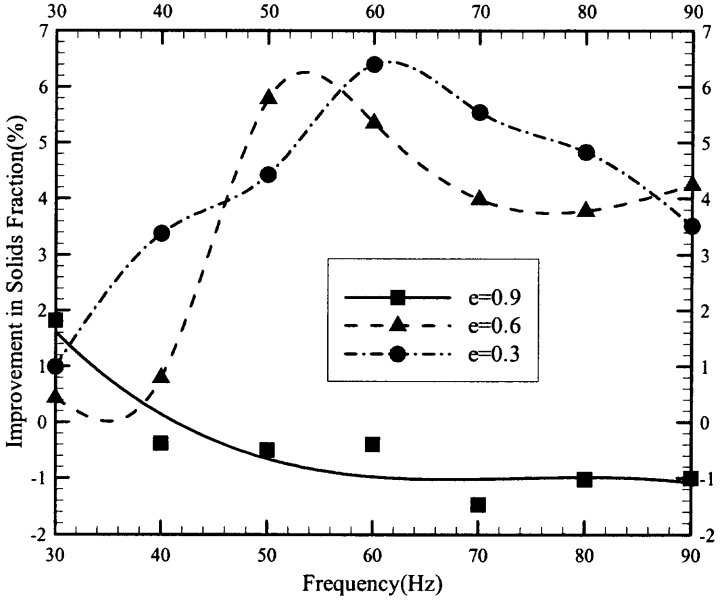

Figure 7.26 Solids fraction versus frequency, $N = 605$, $a/d = 0.48$.

When a/d = 0.24 (Figure 7.25), the assembly with 0.9 restitution coefficient particles reaches its maximum solids fraction at the lowest frequency ($f \cong 40\,\text{Hz}$), followed by e = 0.6 at $f \cong 50\,\text{Hz}$, and e = 0.3 at $f \cong 80\,\text{Hz}$. These differences in frequency are again attributed how easily the system attains the proper thermal dynamic state, which depends on the restitution coefficient of the particles comprising the assembly. Note that at 70 Hz, the e = 0.9 curve indicates that the system is over thermalized since the there is no improvement in solids fraction upon relaxation. Figure 7.26 (a/d = 0.48) continues to show that the e = 0.9 assembly has been over-thermalized at f = 40Hz, but the other two systems exhibit some solids fraction improvement.

7.7 Effect of Normal Stiffness on Densification

In Chapter 6, it was demonstrated the normal loading stiffness K_1 only affected the dynamic state in the low relative acceleration regime.

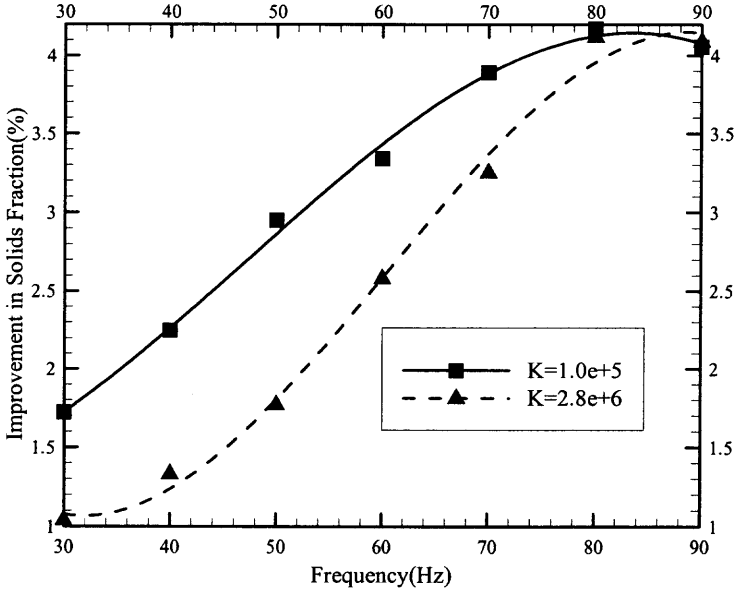

Figure 7.27 Solids fraction versus vibration frequency, N = 605, a/d = 0.02.

Figure 7.27 shows the percentage improvement in solids fraction versus frequency when a/d = 0.02 for two values of the loading stiffness. The improvement increases monotonically with frequency as the difference between the curves is reduced.

The qualitative features in the curves (Figures 7.28 – 7.30) at each amplitude level are quite similar, and only the magnitude of the improvement differs with the loading stiffness. Most important is that the frequency at which the peak occurs at each fixed vibration amplitude is not highly sensitive to the value of K_1. This result indicates that normal stiffness does not have a great effect on the trend of improvement versus frequency at higher relative accelerations.

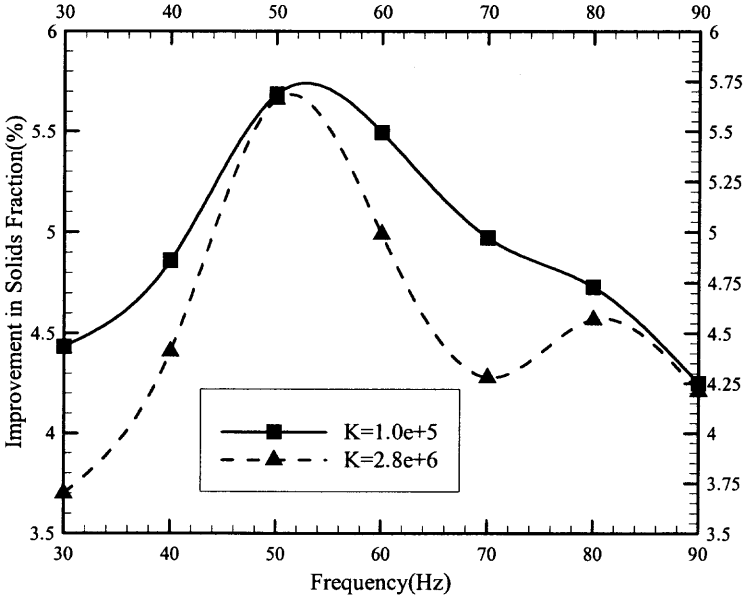

Figure 7.28 Solids fraction versus vibration frequency, $N = 605$, $a/d = 0.08$.

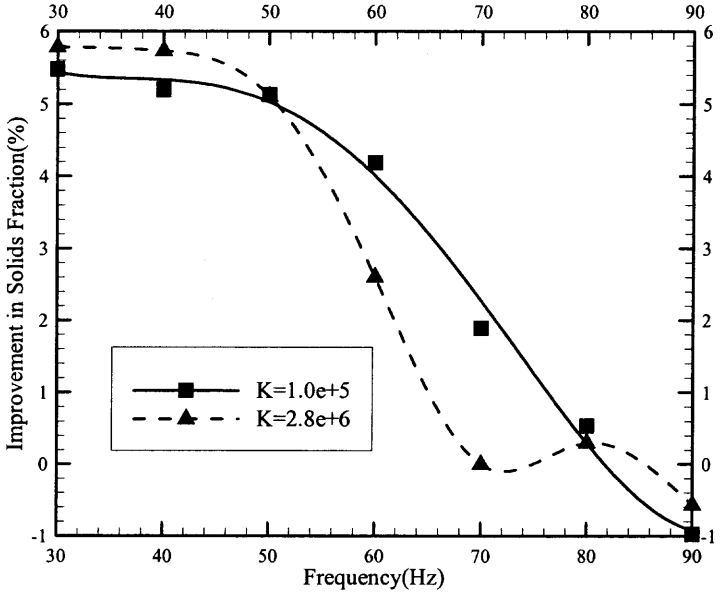

Figure 7.29 Solids fraction versus vibration frequency, $N = 605$, $a/d = 0.24$.

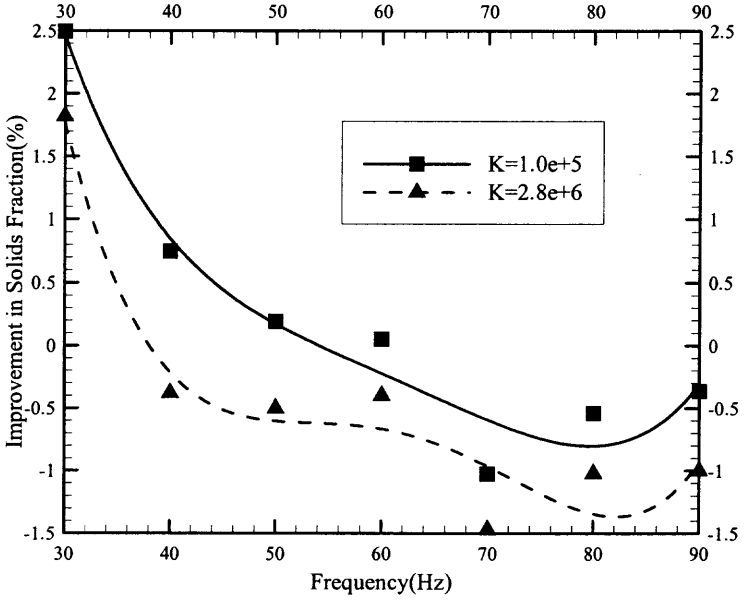

Figure 7.30 Solids fraction versus vibration frequency, $N = 605$, $a/d = 0.48$.

7.8 Phase Chart of Densification

In this section, a contour plot is presented that portrays the overall relationship between improvement in solids fraction against frequency and amplitude. This is done by simulating a system having $N = 8000$ particles, $L/d = 25$, and $0.02 \leq a/d \leq 0.48$ and 10Hz $\leq f \leq$ 90Hz, with $e = 0.9$, $\mu_p = 0.1$ and $\mu_w = 0.3$. It is conjectured that similar plots may exist for other materials, although this has not been done in the current investigation.

Figure 7.31 shows the densification contour plot as a function of amplitude and frequency, where the color indicates the extent of the improvement as given in the included scale. Four rather distinct improvement zones appear, corresponding to various levels of the improvement in solids fraction. "Zone1" is characterized by improvements of less than 1%, while assemblies in "Zone 2" show an improvement of the order of 3%. "Zone3" systems are distinguished by a significant improvement of the order of 5% or better. Finally, "Zone4" systems attain little or no solids fraction improvement, which is characteristic of an over-thermalized dynamic state before relaxation.

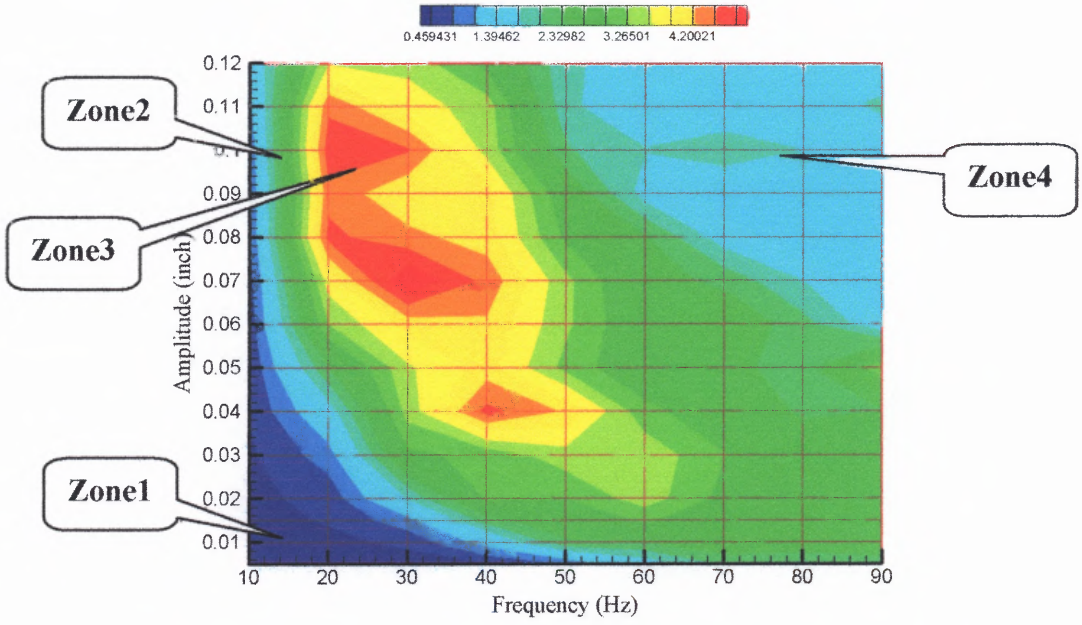

Figure 7.31 Phase chart of densification, $N = 8000$, $L/d = 25$.

7.9 Generation of Random "Closest" Packing

In Chapter 6, the simulation results for the solids fraction of random "loose" packing were shown to be in good agreement with the results of physical experiments and other simulations in the literature. In this section, a random "closest" packing is produced by vibrating the assembly of $N = 8000$ spheres in a cell having an aspect ratio $L/d = 25$. In addition, the arrangement of the particles directly adjacent to the wall is obtained when the system is in the closed packing state.

7.9.1 Random "Closest" Packing

In order to obtain a dense random packing, it is necessary to find suitable conditions at which to vibrate the assembly. This is accomplished by shaking the system at different vibratory conditions for 3 seconds and by plotting the bulk solids fractions (relaxed) to select the optimum settings.

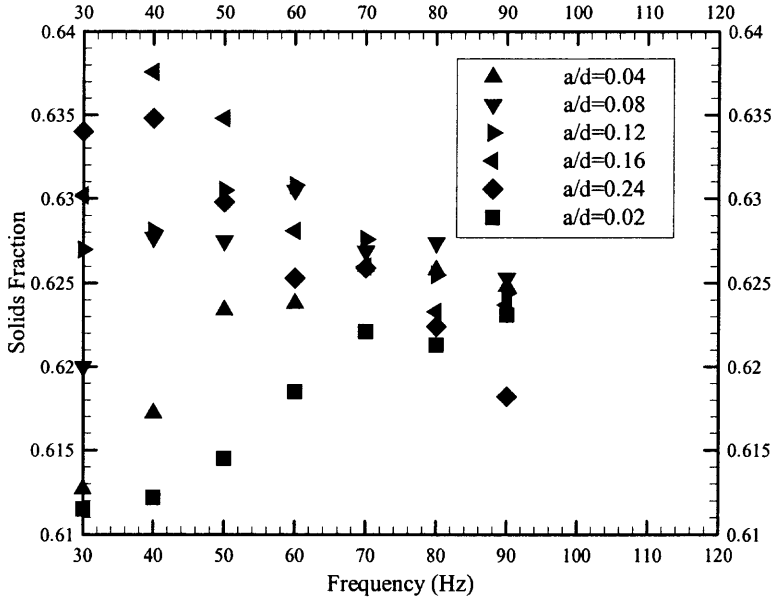

Figure 7.32 Solids fraction versus vibration intensity ($N = 8000$, $L/d = 25$).

From Figure 7.32, it can be seen that this occurs when f = 40Hz and a = 0.04″. Using these parameters, the system is vibrated for T_v seconds until the solids fraction curve flattens out, as shown in Figure 7.33a. An extrapolation is performed as $T_v^{-1} \rightarrow 0$ to obtain the solids fraction for random close packing (Figure 7.33b). A value of 0.6582 is found, which is very close to the experimental results of Nowak et al. [11].

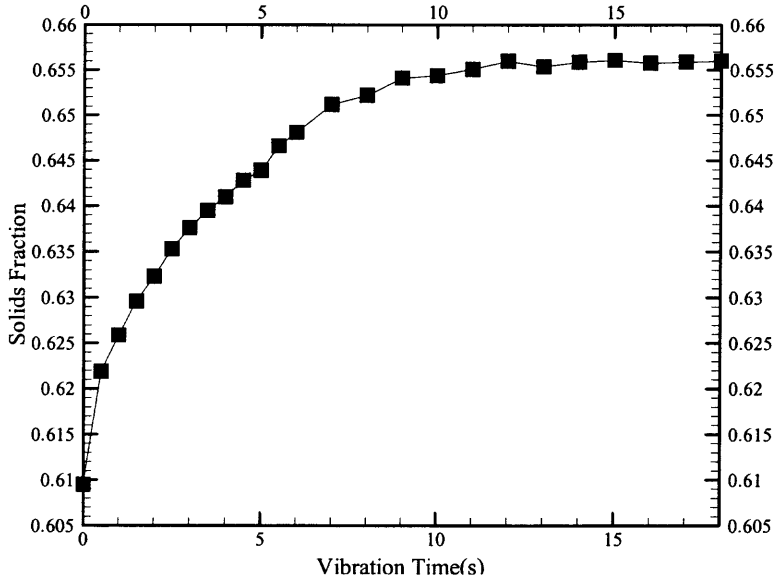

Figure 7.33a Evolution of solids fraction, N = 8000, f = 40Hz, a = 0.04″.

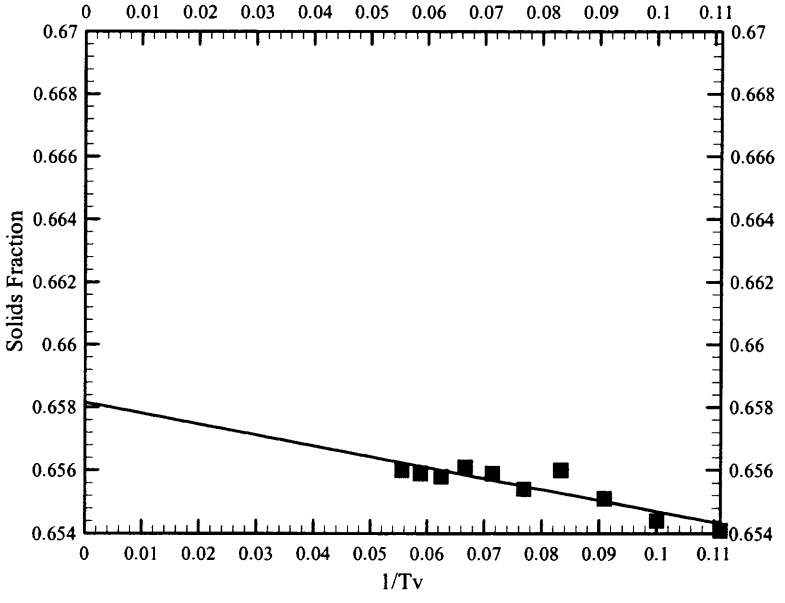

Figure 7.33b Extrapolation of the solids fraction to obtain the random close packing value, here, T_v is vibration time.

7.9.2 Particle Structure Near the Wall

Experimental observations presented in Chapter 2 revealed (Figure 2.11) an interesting ordered arrangement of the particles against the wall. A similar feature is produced in the simulations after 13 seconds of vibration, as can be seen in Figures 7.34a, b.

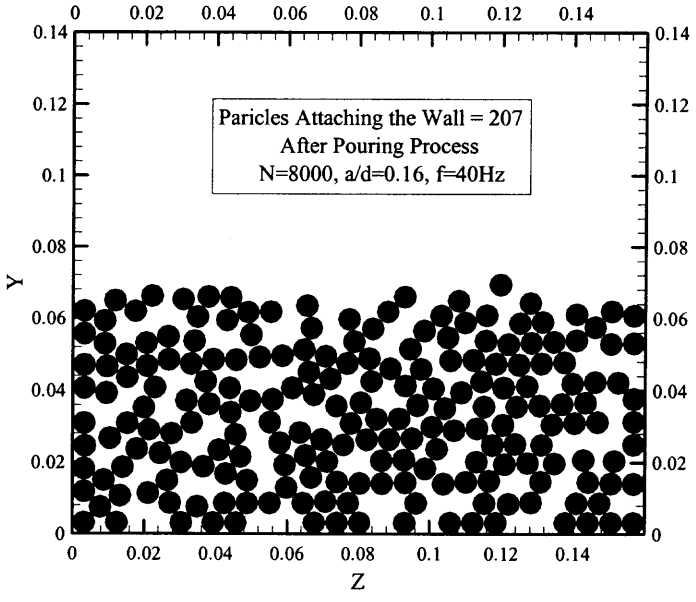

Figure 7.34a Wall particle arrangement after the pouring process.

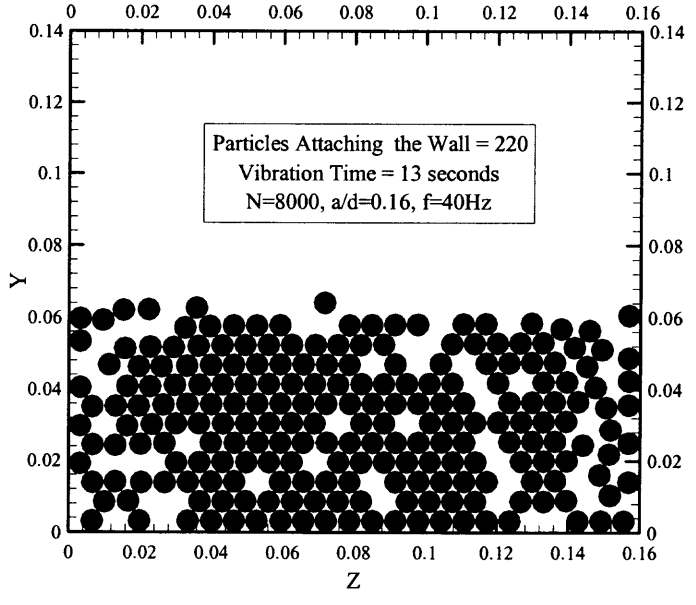

Figure 7.34b Wall particle arrangement after 13 seconds of vibration.

7.10 Conclusions

From the simulation studies discussed in the Chapter, the following conclusions are made:

1) The simulation was able to duplicate all phenomenon that occurred in physical experiments. At low relative accelerations, the densification mechanism is simply a shifting of particles towards the bottom of the cell, which causes a small improvement in solids fraction. A substantial increase in solids fraction takes place only when the assembly has been fully thermalized to the proper degree.

2) The depth of a system has a pronounced effect on solids fraction improvement, i.e., deeper assemblies require stronger floor vibrations to attain the same bulk density (and level of agitation) as shallower assemblies after relaxation.

3) A level of vibration that causes a decrease in the average solids fraction upon relaxation of a shallow bed can induce densification in deeper assemblies.

4) Smooth sphere systems do not easily attain a large degree of densification. However, assemblies consisting of highly frictional particles are more responsive to the vibrations and more easily attain a large increase in average solids fraction.

5) The container aspect ratio and normal stiffness of the particles have almost no effect on the trends of solids fraction against the frequency of vibration.

6) At large relative accelerations, normal restitution coefficient e greatly affects solids fraction. As e increases, the assembly attains their maximum improvement in solids fraction at lower floor vibration frequencies than do more dissipative particle systems, which have smaller maximums.

7) The simulation is capable of producing a random close packing that is in very good agreement with physical experiments.

8) The particle structure near the wall is very similar with observations made in physical experiments.

CHAPTER 8

CONCLUSIONS

Physical experiments as well as discrete element simulations have been successfully carried out to deepen the understanding of pouring process, vibration-induced fluidization and densification. In physical experiment, before vibration is imposed, the particle bed is prepared by pouring mono-disperse acrylic particles with different diameters into a cylinder. It is found that with the increase of aspect ratio (D/d), the solids fraction becomes bigger and its fluctuation is smaller, then the different amplitudes (a) and frequencies (f) are applied to facilitate the observation of four densification trends. The results show that attaining the "maximum density" is closely related to the combination of frequency and amplitude, and vibration amplitude (a) affects the densification trends. Additionally, convection can accelerate or hinder the densification process. At the vibration conditions, which can induce a big improvement in solids fraction, a crystal-like structure is obtained against the container wall, which may be the reason for the particle bed to easily reach a solid fraction of 0.6366. For multi-disperse polyethylene pellets, there is a substantial increase in solids fraction due to the effects of particle shape and surface friction, and the slope angle of top surface and fluidization behavior of particle beds with different pellets also show some effects of particle surfaces and shapes.

Computer simulations applying the discrete element method are then used to carefully investigate the influences of material properties, pouring methods and container geometry on the pouring process. Normal force models with constant restitution coefficient and variable restitution coefficient have been used. It is found that aspect ratio

and particle friction coefficient have a pronounced influence on the solids fraction, other parameters, such as restitution coefficient, normal stiffness and material density have little effect on the poured solids fraction. The solids fraction of random "loose" packing is derived by interpolation and matches the experimental results of Macrae [30] and Scott [7]. The collision simulation between two particles is also in good agreement with those of Goldsmith [55].

Vibration process is then simulated. The instantaneous dynamic states have also been analyzed by using the depth profiles of granular temperature, solids fraction and translational energy ratio, and the effects of height of particle bed, friction coefficient, normal stiffness, restitution coefficient, aspect ratio of container and initial poured states are deeply studied. At the same time, the dynamic state is divided in three phases depending on the translational energy ratio. The results from different vibration conditions are in agreement with the observation of Eversque et al. and consistent with theoretical predictions of Richman et al. at the high relative accelerations. Depths of particle beds have a big effect on the dynamic behaviors under the same vibration conditions. With the increase of depths, the beds are more difficult to be thermalized. The results are in good agreement with the experiment of Thomas et al. Friction coefficient shows strong influence on the dynamic behaviors. Its effect is different at low and high relative accelerations. At low relative acceleration, the particle bed with higher friction coefficient shows a stronger trend to be thermalized, but at a high relative acceleration, the particle bed with smaller friction coefficient shows a stronger trend to be thermalized. For aspect ratio and normal stiffness, only at low relative acceleration, their influences appear, and only at low relative accelerations, the initial structure of the poured particle

bed strongly affects the dynamic behavior during vibration. For the effect of restitution coefficient, it becomes apparent with the increase of relative accelerations.

The main contributions of the research are duplication of four densification trends and the establishment of relationship between the instantaneous dynamic states and final relaxed states. At low relative accelerations, the densification mechanism is that the particles just shift to the bottom, which makes the solids fraction increase, but this improvement is limited. Big improvement only happens when the bed is totally thermalized. Depth of a particle bed has big effect on the improvement in solids fraction. With the increase of depth, the bed is postponed to attain a big improvement in solids fraction. Some strong vibration can make shallow beds un-densify and deep beds attain small improvement in solids fraction, the reason is strong vibration can make the solids fraction near the bottom smaller than their initials. Smooth spheres make the beds difficult to obtain big increase in solids fraction. Spheres with big friction coefficient make the particle bed more sensitive to vibration and attain high increase in solids fraction. Aspect ratio and normal stiffness have almost no effect on the evolution trends of solids fraction, and restitution coefficient has big effect on the evolution trends of solids fraction at big relative acceleration. With the increase of restitution coefficient, the beds will be quicker to be thermalized and attain big improvement in solids fraction. Similar to the derivation of solids fraction of 'loose' packing, the solids fraction of random 'close' packing has been derived, which is very close to the experiment value, and the particle structure against the wall is very similar with the observation in the real experiment.

The work, which has been done, supplies some directions for the future study.

(1) Calculate the energy distribution of rotational and translational in different zones.

(2) Use a normal force model with variable restitution coefficient to investigate vibration –induced fluidization and densification.

(3) Modify boundary condition to a cylinder.

(4) Apply multi-disperse particle system to investigate vibration-induced segregation.

(5) Develop algorithms to simulate non-sphere particles.

APPENDIX

VIBRATION PARAMETERS FOR EXPERIMENT

1. Densification under Vibration with Mono-disperse Acrylic Spheres

Table A.1 Experiment 1 for $a/d = 0.04$

Frequency, f, Hz	Amplitude, a, inch	a/d	Acceleration, Γ, g
55	0.005	0.04	1.55
60	0.005	0.04	1.84
65	0.005	0.04	2.16
70	0.005	0.04	2.51
75	0.005	0.04	2.88
80	0.005	0.04	3.28
85	0.005	0.04	3.70
90	0.005	0.04	4.15
95	0.005	0.04	4.62
100	0.005	0.04	5.12

Table A.2 Experiment 2 for $a/d = 0.06$

Frequency, f, Hz	Amplitude, a, inch	a/d	Acceleration, Γ, g
55	0.075	0.06	2.32
60	0.075	0.06	2.76
65	0.075	0.06	3.24
70	0.075	0.06	3.76
75	0.075	0.06	4.32
80	0.075	0.06	4.92
85	0.075	0.06	5.54
90	0.075	0.06	6.22
95	0.075	0.06	6.93
100	0.075	0.06	7.67

Table A.3 Experiment 3 for $a/d = 0.08$

Frequency, f, Hz	Amplitude, a, inch	a/d	Acceleration, Γ, g
40	0.01	0.08	1.61
45	0.01	0.08	2.04
50	0.01	0.08	2.52
55	0.01	0.08	3.05
60	0.01	0.08	3.63
65	0.01	0.08	4.26
70	0.01	0.08	4.93
75	0.01	0.08	5.66
80	0.01	0.08	6.45
85	0.01	0.08	7.28

Table A.4 Experiment 4 for $a/d = 0.1$

Frequency, f, Hz	Amplitude, a, inch	a/d	Acceleration, Γ, g
40	0.0125	0.1	2.01
45	0.0125	0.1	2.55
50	0.0125	0.1	3.15
55	0.0125	0.1	3.81
60	0.0125	0.1	4.54
65	0.0125	0.1	5.33
70	0.0125	0.1	6.16
75	0.0125	0.1	7.08
80	0.0125	0.1	8.06
85	0.0125	0.1	9.10
90	0.0125	0.1	10.20
95	0.0125	0.1	11.54

Table A.5 Experiment 5 for $a/d = 0.12$

Frequency, f, Hz	Amplitude, a, inch	a/d	Acceleration, Γ, g
35	0.015	0.12	1.88
40	0.015	0.12	2.45
45	0.015	0.12	3.11
50	0.015	0.12	3.84
55	0.015	0.12	4.64
60	0.015	0.12	5.52
65	0.015	0.12	6.48
70	0.015	0.12	7.52
75	0.015	0.12	8.63

Table A.6 Experiment 6 for $a/d = 0.2$

Frequency, f, Hz	Amplitude, a, inch	a/d	Acceleration, Γ, g
25	0.025	0.2	1.60
30	0.025	0.2	2.31
35	0.025	0.2	3.14
40	0.025	0.2	4.02
45	0.025	0.2	5.10
50	0.025	0.2	6.30
60	0.025	0.2	7.62

Table A.7 Experiment 7 for $a/d = 0.24$

Frequency, f, Hz	Amplitude, a, inch	a/d	Acceleration, Γ, g
25	0.03	0.24	1.92
30	0.03	0.24	2.76
35	0.03	0.24	3.76
40	0.03	0.24	4.91
45	0.03	0.24	6.22

2. Densification under Vibration with Multi-disperse Polyethylene Pellets

Table A.8 Experiment 8 for $a = 0.005''$

Frequency, f, Hz	Amplitude, a, inch	Acceleration, Γ, g
45	0.005	1.04
50	0.005	1.28
55	0.005	1.55
60	0.005	1.84
65	0.005	2.16
70	0.005	2.52
75	0.005	2.88
80	0.005	3.28
85	0.005	3.7

Table A.9 Experiment 9 for $a = 0.01''$

Frequency, f, Hz	Amplitude, a, inch	Acceleration, Γ, g
30	0.01	0.92
35	0.01	1.25
40	0.01	1.64
45	0.01	2.07
50	0.01	2.56
55	0.01	3.1
60	0.01	3.68

Table A.10 Experiment 10 for $a = 0.015''$

Frequency, f, Hz	Amplitude, a, inch	Acceleration, Γ, g
25	0.015	0.96
30	0.015	1.38
35	0.015	1.88
40	0.015	2.46
45	0.015	3.11
50	0.015	3.84

Table A.11 Experiment 11 for $a = 0.02''$

Frequency, f, Hz	Amplitude, a, inch	Acceleration, Γ, g
20	0.015	0.82
25	0.015	1.28
30	0.015	1.84
35	0.015	2.51
40	0.015	3.27
45	0.015	4.14

REFERENCES

1. D. A. Stewart, *High Quality Concrete*, Spon Publishers, London (1951).

2. P. E. Evans, and R. S. Millman, "The Vibratory Packing of Powders". *Power Met*, 7:50 (1964).

3. J. C. Macrae, W. A. Gray, and P. C. Finlayson, "Vibration Packing of Dry Granular Solids", *Nature*, 179:1365 (1957).

4. J. E. Ayer and F. E. Soppet, "Vibratory Compaction: I, Compaction of Spherical Shapes", *J. Am. Ceram. Soc.*, 48(4): 180 (1965).

5. D. J. D'Appolonia, and E. D'Apolonia, "Determination of the Maximum Density of Cohesionless Soils", *Proc.3rd Asian Regional Conference on Soil Mechanics and Foundation Engineering*, 1266~1268, Jerusalem Academic Press (1967).

6. R. Dobry and R. V. Whitman, "Compaction of Sand on a Vertically Vibrated Table: Evaluation of Relative Density and its Role in Geo-technical Projects Involving Cohesionless Soils", *ASTM STP* 523, 156~170, American Society of Testing Materials, Philadelphia (1973).

7. G. D. Scott and D. M. Kilgour, "The Density of Random Close Packing of Sphere", *British Journal of Applied Physics (Journal of Physics D)*, 2(series 2): 863 (1969).

8. O. R. Walton and R. L. Braun, "Viscosity, Granular-temperature, and Stress Calculations for Shearing Assemblies of Inelastic, Frictional Disks," J. Rheology, 30(5), 949-984 (1986).

9. J. B. Knight, C. G. Frandrich C. N. Lau, H. M. Jaeger and S. R. Negel, "Density Relaxation in Vibrated Granular Materials", *Phys. Rev. E* 51, 3957-3963 (1995).

10. E. R. Nowak, M. Povinelli, H. M. Jaeger, and S. R. Nagel, "Studies of Granular Compaction", *Powders & Grains 97*, Editors: R. Behringer and J. Jenkins, Balkema, 377-380 (1997).

11. E. R. Nowak, J. B. Knight, E. B. Naim, H. M. Jaeger, and S. R. Nagel, " Density Fluctuation in Vibrated Granular Materials," *Phys. Rev. E* 57, 1971 (1998).

12. M. Nicodemi, A. Coniglio, H. J. Herrmann, "Frustration and Slow Dynamics of Granular Packing," *Phys. Rev.E*54, 3962 (1997).

13. C. R. Wassgren, M. L. Hunt & C. E. Brennen, "Vertical Vibration of a Deep Bed of Granular Materials Subjected to Vertical Vibration", *Proceedings of the Fifth World Congress of Chemical Engineering*, San Diego, CA, USA, 355-358 (1996).

14. P. Evesque & J. Rajchenbach, "Instability in a Sand Heap". *Physical Review Letters*, 69, 44-46 (1989).

15. E. Clemen, J. Duran & J. Rajchenbach, "Experimental Study of Heaping in a Two-dimensional Sand pile". *Physical Review Letters*, 69, 1189-1192 (1992).

16. S. Douady & C. Laroche, "Sub-harmonic Instabilities and Defect in a Granular Layer under Vertical Vibrations". *Euro-physics Letters*, 8, 621-627 (1989).

17. S. B. Savage, "Streaming Motions in A Bed of Vibrational Fluidized Dry Granular Material", *Journal Fluid Mechanics*, 194, 457-478 (1988).

18. Y. H. Taguchi, "New Origin of Convective Motion: Elastically Induced Convection in Granular Materials". *Physical Review Letters*, 69, 1367-1370 (1992).

19. R. Jullien, P. Meakin & A. Pavlovitch, "Three-dimensional Model for Particle-size Segregation by Shaking". *Physical Review Letters*, 69, 640-643 (1992).

20. A. D. Rosato, K. Strandbury, F. Prinz, R. Swendsen, "Why the Brazil Nuts Are on Top: Size Segregation of Particulate Matter by Shaking". *Phys. Rev, Lett.* 58, 1038-1040 (1987).

21. J. B. Knight, H. M. Jaeger & S. R. Nagel, "Vibration-induced Size Separation in Granular Media: the Convection Connection". *Physical Review Letters*, 70, 3728-3731 (1993).

22. S. S. Hsiau & H. Y. Yu, "Segregation Phenomena in a Shaker". *Powder Technology*, 93, 83-88 (1997).

23. S. Warr, J. M. Huntley, and G. T. H. Jacques, "Fluidization of a Two-dimensional Granular System: Experimental Study and Scaling Behavior," *Phys. Rev. E* 52, 5583 (1995).

24. F. Mel, P. Umbanhowar & H. Swinney, "Transition to Parametric Wave Patterns in A Vertically Oscillated Granular Layer". *Physical Review Letters*, 72, 172-175 (1994).

25. J. Miles & D. Henderson, "Parametrically Forced Surface Waves". *Annual Review of Fluid Mechanics*, 22, 143-165 (1990).

26. S. S. Hsiau & M. S. Wu, "Arching Phenomena in a Vibrated Granular Bed". *Advanced Powder Technology*, 99, 185-193 (1998).

27. C. R. Wassgren, C. E. Brennen & M. L. Hunt, "Vertical Vibration of a Deep Bed of Granular Material in A Container". *Journal of Applied Mechanics*, 63, 712-719 (1996).

28. A. O. Oman & K. M. Watson, "Pressure drops in granular beds," *Natl. Patrol. News* 36, 795-802 (1944).

29. G. D. Scott, "Packing of spheres," *Nature* 188, 908-909 (1960).

30. J. C. Marcrae, W. A. Gray, "Significance of the Properties of Materials in the Packing of Real Spherical Particles", *British Journal of Applied Physics*, 164-172 (1960).

31. E. M. Tory, N. A. Cochrane, S.R. Waddell, *Nature* 220, 1023 (1968).

32. K. Gotoh & J. L. Finney, "Statistical Geometrical Approach to Random Packing Density of Equal Spheres," *Nature* 252, 202-205 (1974).

33. C. H. Bennett, *J. Appl. Phys.* 432, 727 (1972).

34. G. Mason, *Discuss. Faraday Soc.* 43, 1709 (1967).

35. W. S. Jodrey & E. M. Tory, *Phys. Rev.* A 32, 2347 (1985).

36. J. L. Finney, *Mater. Sci. Eng.* 23, 199 (1976).

37. P. A. Cundall, "A Computer Model for Simulating Progressive, Large Scale Movements in Blocky Rock System", *Proceeding of the Symposium of International Society of Rock Mechanics*, Nancy, Article 8 (1971).

38. K. Z. Y. Yen, T. K. Chaki, *J. Appl. Phys.* 71, 3164 (1992).

39. Z. P. Zhang, L. F. Liu, Y. D. Yuan, A. B. Yu, " A Simulation Study of the Effect of Dynamic Variables on the Packing of Spheres", *Powder Tech.*, 116, 23-32 (2001).

40. M. W. Richman & R. E. Martin, "Undefined Granular Materials Thermalized by Fluctuating horizontal Surfaces." *Proc. 9th Conf. Engr. Mech.* (ed. L.D. Lutes, J. N., Niezwecki), ASCE, NY 900-903 (1992).

41. B. Thomas, M. O. Mason, Y. A. Liu, and A. M. Squres, "Identifying States in Shallow Vibrated Beds," *Powder Technology* 57, 267 (1989).

42. Y. D. Lan, and A. D. Rosato, "Macroscopic Behavior of Vibrating Beds of Smooth Inelastic Spheres," *Phys. Fluids*, 7(8): 1818 (1995).

43. M. L. Hunt, S. Hsiau & K. T. Hong, "Particle Mixing and Volumetric Expansion in a Vibrated Granular Bed." *Proc. National Heat Transfer Conference* (1993).

44. Y. D. Lan and A. D. Rosato, "Convection Related Phenomena in Granular Dynamics Simulations of Vibrated Beds," *Phys. Fluids*, 9(12): 3615 (1997).

45. L. Vanel, A. D. Rosato, and R. N. Dave, "Rise-time Regimes of a Large Sphere in Vibrated Bulk Solids," *Phys. Rev. Lett.*, 78, 1255 (1997).

46. S. S. Hsiau, S. J. Pan, "Motion State Transitions in a Vibrated Granular Bed", *Powder Tech.*, 96, 219-226 (1998).

47. S. C. Yang, S. S. Hsiau, "Simulation Study of the Convection Cells in a Vibrated Granular Bed." *Chemical Engineering Science* 55, 3627-3637 (2000).

48. S. Ogawa, "Multi-temperature Theory of Granular Materials." *Proc. US-Japan Seminar on Continuum-Mechanical and Statistical Approaches in the Mechanics of Granular Materials*, Tokyo, 208-217 (1978).

49. S. B. Savage & D. J. Jeffrey. "The Stress Tensor in a Granular Flow at High Shear Rates." *J. Fluid Mech.* 110, 255-272 (1981).

50. C. K. K. Lun, S. B. Savage, D. J. Jeffrey & N. Chepurnity, "Kinetic Theories for Granular Flow: Inelastic Particles in Couette Flow and Slightly Inelastic Particles in a General Flow Field", *J. Fluid Mech.* 140, 223-256 (1984).

51. J. T. Jenkins & M. W. Richman, "Boundary Conditions for Plane Flows of Smooth, Nearly Elastic, Circular Disks," *J. Fluid Mech.* 171, 53-69 (1986).

52. G. C. Barker, and A. Mehta, "Vibrated Powder: Structure, Correlations, and Dynamics," *Phys. Rev. A* 45, 3435 (1992); G. C. Barker, and A. Mehta, *Phys. Rev. E* 47, 184 (1993).

53. A. D. Rosato, and D. Yacoub, "Microstructure Evolution in Compacted Granular Beds", *Powder Technology*, 109, 255 (2000).

54. M. Takabshi & S. Suzuki, "Numerical Analysis of Tapping Behavior of Ceramic Powders", *Ceramic Bulletin* 65, 1587 (1986).

55. W. Goldsmith, *Impact*, Edward Arnold (Publishers) Ltd, London, 1960.

56. K. K. Yin, "Numerical Modeling of Agglomerate Degrading," *PhD Thesis*, Aston University, 1992.

57. G. Lian, C. Thornton and M. J. Adams, "Discrete Particle Simulation of Agglomerate Impact Coalescence," *Chemical Eng. Sci.*, 53, No. 19, 3381-3391 (1998).

58. O. R. Walton, "Numerical Simulation of Inclined Chute Flows of Monodisperse, Inelastic Frictional Spheres", *Advances in Micro-mechanics of Granular Materials* (Eds. H. H. Shen, M. Satake, M. Mehrabadi, C. S. Campbell), Elsevier, 453-461 (1992).

59. R. Mei, H. Shang, O. R. Walton and J. F. Klausner, "Concentration Non-uniformity in Simple Shear Flow of Cohesive Powders", *Powder Tech.*, 112, 102-110 (2000).

60. O. R. Walton, *Energy and Technology Review*, Lawrence Livermore Lab., 24 (1984).

61. M. A. Hopkins and H. Shen, "Constitutive Relations for A Planar, Simple Shear Flow of Rough Disks", *Int. J. Eng. Sci.*, 24, 1717-1730 (1986).

62. J. Ghaboussi and R. Barbosa, *Int. J. Num. Anal. Meth. Geomech.*, 14, 451 (1990).

63. O. R. Walton and R. L. Braun, "Stress Calculations for Assemblies of Inelastic Spheres in Uniform Shear", *Acta Mech.*, 63, 73 (1986).

64. O. R. Walton, "Numerical Simulation of Inelastic, Frictional Particle-Particle Interactions", *in Particulate Two-Phrase Flow* (ed. M.C. Roco), 884-911 (1992).

65. L. Verlet, "Computer 'Experimental' on Classic Fluids. I Thermodynamical Properties of Leonard-Jones Molecules," *Phys. Rev.,* 159, 98-103 (1967).

66. Y. D. Lan, "Particle Dynamics Modeling of Vibrating Granular Beds", *PhD thesis*, NJIT, 1994.

67. K. Shinohara, *Handbook of Powder Science and Technology*, edited by M.E. Fayed and L. Otten (Van Nostrand Reinhold Co., New York, 1984).

68. T. Baumeister, L. S. Marks, *Standard Handbook for Mechanical Engineers*, McGraw-Hill Book Company, New York, 1967.

69. J. Litwinyszn, *Bull. Acad. Polon. Sci. Ser. Sci. Tech.* 11, 593 (1962).

70. W. W. Mullins, *J. Appl. Phys.* 43, 867 (1974).

71. R. Neddermann, T. Davier, and D. Horton, *Powder Tech.*, vol. 25, 215 (1980).

72. R. Neddermann, U. Tuzun, and G. T. Houlsby, *Chem. Eng. Sci.* 37, 1597 (1982).

73. M. W. Richman, "Boundary Conditions for Granular Flows at Randomly Fluctuating Bumpy Boundaries," *Advances in Micro-mechanics of Granular Materials*, edited by H. H. Shen, M. Satake, M. Mehrabadi, C. S. Chang, and C. S. Campbell, 111-122 (1992).

74. A. D. Rosato, Y. Lan, D. T. Wang, "Vibratory Particle Size Sorting in Multi-component System," *Powder Tech.,* 66, 149-160 (1991).

75. G. L. Liu, K. E. Thompson, "Influence of computational Domain Boundaries on Internal Structure in Low-porosity Sphere Packings", *Powder Tech.*, 113, 185-196 (2000).

76. A. D. Rosato, D. L. Blackmore, N. H. Zhang, Y. D. Lan, "A Perspective on Vibration-induced Size Segregation of Granular Materials", *Chemical Engineering Science* 57, 265-275 (2002).

77. W. L. Chen, "Numerical Simulation of Mechanofusion System for Dry Particle Coating Process", *Ph.D thesis*, NJIT, 2002.

78. S. F. Foerster, M. Y. Louge, H. Chang and K. Allia, "Measurements of the Collision Properties of Small Spheres", *Phys. Fluids* 6(3), 1-8 (1994).

79. K. L. Johnson, *Contact Mechanics*, Cambridge University Press, Cambridge, 1985.

80. S. Timoshenko, J. N. Goodier, *Theory of Elasticity*, McGraw-Hill, New York, 1951.

81. S. Tulluri, "Analysis of the Random Packing of Uniform Spheres using the Monte-Carlo Simulation Method", *MS thesis*, NJIT, 2003.

82. D. J. Adams and A. J. Matheson, "Computation of Dense Random Packing of Hard Spheres", *J. Chem. Phys.* 56, 1989-1994 (1972).

83. A. J. Matheson, "Computation of Random Packing of Hard Spheres", *J. Phys.* 7, 2569-2676 (1974).

84. W. M. Visscher and M. Bolsterli, "Random Packing of Equal and Unequal Spheres in Two and Three Dimensions", *Nature* 239, 504-507 (1972).

85. M. J. Powell, "Computer-Simulated Random Packing of Spheres," *Powder Technology* 25, 45-52 (1980).

86. J. Rodriguez, C. H. Allibert, and J. M. Chaix, "A Computer Method for Random Packing of Spheres of Unequal Size", *Powder technology* 47, 25-37 (1986).